EXTRACTION OF SPIN POLARIZATION OF BULK AND MEASUREMENT OF TRANSPORT PROPERTIES OF THIN Gd_XSi_{1-X} NEAR THE METAL-INSULATOR TRANSITION

A Dissertation

by

RAJ VIBHUTI ANAND SRIVASTAVA

Submitted to the Office of Graduate Studies of
Texas A&M University
in partial fulfillment of the requirements for the degree of

DOCTOR OF PHILOSOPHY

May 2009

Major Subject: Physics

EXTRACTION OF SPIN POLARIZATION OF BULK AND MEASUREMENT OF TRANSPORT PROPERTIES OF THIN Gd_XSi_{1-X} NEAR THE METAL-INSULATOR TRANSITION

A Dissertation

by

RAJ VIBHUTI ANAND SRIVASTAVA

Submitted to the Office of Graduate Studies of
Texas A&M University
in partial fulfillment of the requirements for the degree of

DOCTOR OF PHILOSOPHY

Approved by:

Chair of Committee,	Winfried Teizer
Committee Members,	Glenn Agnolet
	Mosong Cheng
	Donald Naugle
Head of Department,	Edward Fry

May 2009

Major Subject: Physics

ABSTRACT

Extraction of Spin Polarization of Bulk and Measurement of Transport Properties of Thin Gd_xSi_{1-x} Near the Metal-Insulator Transition. (May 2009)

Raj Vibhuti Anand Srivastava, B.Sc.; M. Sc., Indian Institute of Technology, India;

M.S., Texas A&M University

Chair of Advisory Committee: Dr. Winfried Teizer

Since the early 1960s, Abrikosov-Gorkov theory has been used to describe superconductors with paramagnetic impurities. Interestingly, the density of states resulting from the theoretical framework has to date only been known approximately, as a numeric solution of a complex polynomial. An analytical solution to the theory was discovered and applied to extract the spin polarization from the tunneling conductance of superconducting aluminium with 3-dimensional (3-D) amorphous (a-) $gadolinium_xsilicon_{1-x}$ (Gd_xSi_{1-x}) as a counter electrode ($Al/Al_2O_3/a\text{-}Gd_xSi_{1-x}$ planar tunnel junction measured at T = 25 mK and $H \leq 3.0$ T) in the quantum critical regime (QCR). The analytical solution is valid in the whole regime of Abrikosov–Gorkov theory independent of the presence of an energy gap.

Applying the spin polarized Abrikosov-Gorkov theory to describe aluminium gives a larger spin polarization in Gd_xSi_{1-x} than the spin polarized Bardeen-Cooper-Schrieffer (BCS) theory. The purpose of this study is to extract polarization at various applied magnetic fields, but no specific relationship between the two could be

determined. Results obtained shows a transition from a superconductor with a gap to a gapless superconductor in varying external magnetic fields was observed.

To improve understanding of Gd_xSi_{1-x} near the metal-insulator transition (MIT) and compare it with prior work, the initial experimental attempts to investigate the transport property of Gd_xSi_{1-x} near the MIT in the 2-dimensional limit are presented. A low temperature ultra high vacuum quench condensation system was used to make thin films of Gd_xSi_{1-x} and in-situ measurements were performed. The transport properties for different values of x and thicknesses were measured for T = 4.2 K to ~10 K. In addition to other possible causes, the uncertainty in the electron impact emission spectroscopy (EIES) appeared to be a major reason behind the observed error in x when gadolinium and silicon are co-evaporated. The problems faced during the co-evaporation are also discussed.

DEDICATION

I would like to dedicate this work to my parents, my brother Vijay and my sisters, Rajshree and Jayashree. It is only because of their love and support that I have reached this far in my life.

ACKNOWLEDGEMENTS

My graduate studies at Texas A&M have been rich in experience, both intellectually and professionally. I have had an excellent opportunity to work with some of the best and brightest minds in the world. The debt of gratitude I owe is too large to express in words, and any attempt to repay this debt remains meaningless.

First of all, I would like to express gratitude and sincere thanks to my advisor, Dr. Winfried Teizer, for his tremendous support and encouragement. A visionary and a teacher, he guided me through good and bad times and helped me find strength and inspiration by sharing his experiences and knowledge. An extra thanks goes for piloting the memorable flying ride over Brazos county.

I am grateful to Dr. Glenn Agnolet, Dr. Don Naugle and Dr. Mosong Cheng for being on my dissertation committee and generously offering their time and expertise along the way.

I appreciate Dr. Chia-Ren Hu, Dr. Frances Hellman and Dr. Bob Dynes for sharing their experience and knowledge related to Spin Polarized tunneling phenomenon, and Dr. A. Finkelstein and his student, Karen Michaeli, for insightful discussions related to two dimensional limits and the effect of magnetic impurities near Metal-Insulator Transition (MIT). Their constructive insights into the subject were much needed.

I would like to thank Dr. D. Rathanayaka for his guidance in operating and understanding the workings of an ultra high vacuum, low temperature e-gun evaporator;

Dr. Ray Guillemette (Electron Microprobe Laboratory, Department of Geology and Geophysics) for performing the characterization of thin film samples using WDS and EDS; and, Steve, Jason, James and Tom of the electronic shop for their support in maintaining electronics of the e-gun system.

I would like to thank all my nanolab mates, Dr. K. Kim, Dr. Dongmin Seo, Dr. Huachun Xu, Dr. Louhan Peng, Dr. Joel Means, John Noel, Arlene Ford and Tracey, for tirelessly answering all my questions (no matter how inane they were) and infallibly motivating me. They made my experience here to be as enjoyable and beneficial as it possibly could have been.

I would also like to acknowledge The Robert A. Welch Foundation and The Department of Physics for providing financial support; Sandi Smith, Yasa Rathanayaka and Minnotte Biblo for their prompt support; and, fellow Teaching Assistants; Sam, Matt, Dave, Karrie, Mike, Venkat, Milan and Lucas for all the good times and the support that they provided.

Many thanks are also extended to my Aggie buddies, Priyanka, Aparna, Uma, Kapil, Salil, Rana, Naresh, Arnab, Anshu and Tarun, and also my school friends, Rohit, Nishant, Ashish and Nidhi, whose constant encouragement and much needed distractions made graduate life an unforgettable experience for me.

Finally, thanks to my parents and siblings for their encouragement and unfailing love.

TABLE OF CONTENTS

CHAPTER Page

LIST OF FIGURES

FIGURE Page

FIGURE Page

FIGURE Page

FIGURE Page

LIST OF TABLES

CHAPTER I

INTRODUCTION

The existence of solids as either metals or insulators has been a fundamental physical observation. In a metal electrons are free to move around, whereas in an insulator electrons are bound to their atoms. To provide one specific theory to explain metal-insulator transition (MIT) phenomena has been a challenge for many decades. The age-old question, "What mechanism at the atomic scale changes the physical properties of the bulk material?" becomes even more interesting and tricky in the context of the MIT.

A. OVERVIEW

The MIT is one of the most interesting phenomena in condensed matter physics.[1] Different MITs can be classified depending on structural, electronic or correlation effects (electron-exciton interactions), magnetic (either orbital or spin) interactions, variable valence effects, order-disorder transitions and others.[2] Some MITs are the result of more than one of the above effects.

This dissertation follows the style of Physical Review B.

No single comprehensive theory exists that can explain all the different types of MITs, however, depending on the system and the internal conditions, a specific explanation prevails for each observed MIT.

Recently, the field of MIT has resurfaced and received considerable attention, mainly due to the discovery of high T_c-superconductivity and colossal magneto resistance (CMR) in perovskite-like metal-oxide cuprates and manganites.[3-11] The MIT has been revisited in recent years to improve the understanding of the Mott transition,[3-9,12] which is controlled by the electron density at zero temperature. The Mott transition occurs at a critical density n_c, which is a result of the Mott criterion. The Mott transition theory fails to explain some other observed phenomena in the MIT such as magnetic effects, electron-phonon coupling (polarons), disorder (Anderson Localization) and other interactions.[12]

The MIT in doped semiconductors has been a well known subject of investigation for many years,[3-6] and is studied in detail in a large number of experiments related to the MIT field, for example Ref.[13-21] and references within. Random doping can cause a system to become extremely disordered; that increasing disorder leads to an Anderson transition where the carriers become localized. Contrary to localization due to disorder, the correlation of electrons becomes important and the system is close to a Mott transition. Some systems show both Mott and Anderson effects, and as the doping concentration is increased, semiconductors reach the percolation limit (Anderson-Mott transition) and become insulator.

B. METAL-INSULATOR TRANSITIONS

Generally, MITs are divided into two categories depending on the method of physical effects -- structural effects and electronic effects. While the former lead to a change in the band gap that changes the conduction electrons and hence causes a MIT, the latter can further be divided into two classes: a transition affected by electronic correlation and a transition affected by disorder. The first is known as a Mott transition and the second as an Anderson transition.

B.1. THE MOTT TRANSITION

In the late 1920s, Bloch, Peierls and Wilson gave a successful quantum mechanical explanation for physical properties of metals and non metals. In 1937, Boer and Verwey pointed out that nickel oxide does not show metallic behavior, although according to the Bloch, Peierls and Wilson theory, it should have shown metallic behavior due to the partially filled d-band of the Ni^{2+} ion. The lack of consistency in theory and experiment stimulated further investigation of descriptions for transitions of metals and non metals.

Mott explained the MIT for a crystalline system by considering a system made of hydrogen-like atoms with a lattice parameter *a*, which can be varied. Mott calculated that a MIT will occur when

$$n^{1/3} a_H \cong 0.2 \qquad \text{(I-1)}$$

where n is the number of lattice points per unit volume and a_H is the hydrogen radius. When $a \sim (n)^{-1/3}$ is small, the system is a normal metal; however, when a is large, the system is an insulator. Somewhere between these two ranges, there is a sharp transition from a normal metal to an insulator. At zero temperature, there will be a sudden, sharp change in conductivity from infinity to zero. The formula in Eq. (I-1) gives successful results in heavily doped semiconductors. In the Mott transition at T=0, the number of carriers vanishes.[22]

B.2. THE ANDERSON TRANSITION

For disordered systems, a different form of MIT occurs. It is known as the Anderson transition. In these systems, electrons can stay localized at a range of energies. At zero temperature, the system will not conduct, even though the density of states is non zero near the Fermi level.

In 1958, Anderson showed that in certain random fields, when the random potential difference, V_0, is larger than the band width, B, the electron wave function can be localized, which leads to zero conductivity. Figure I-1 shows a random potential energy model as introduced by Anderson.

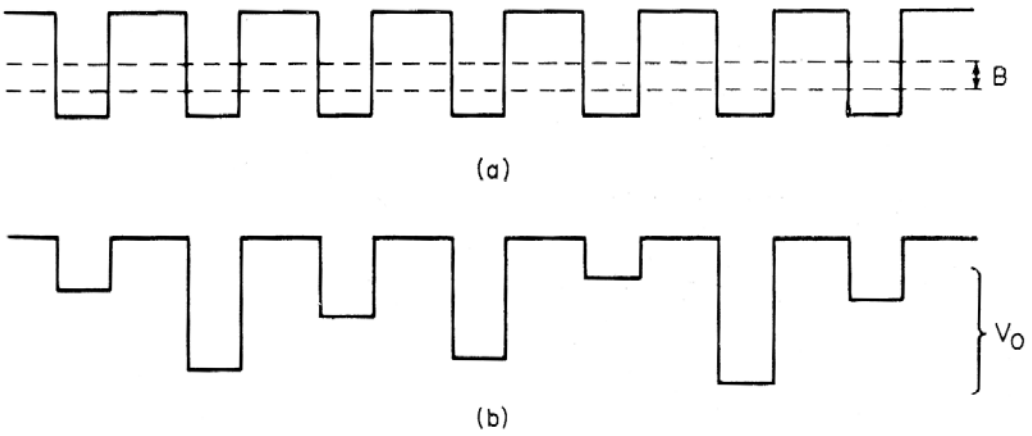

FIG. I-1. Random potential energy introduced by Anderson (a) V_0=0. (b) V_0/B large.[3]

If the random potential model has fluctuations within the limits of ±1/2 V_o then, for a critical value of $(V_o/B)_{\text{critical}}$ at zero temperature, the diffusion of electrons is not possible. Figure I-2(b) shows localized wave functions that lead to zero conductivity.

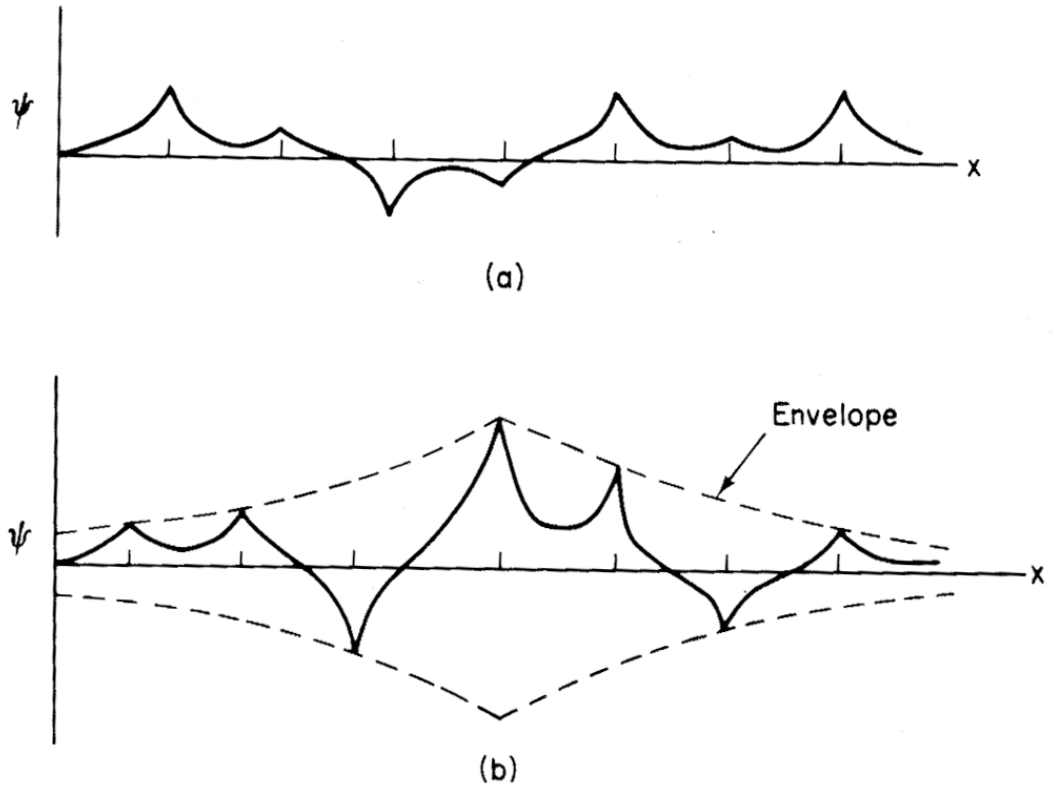

FIG. I-2. Wave function of an electron when $L \sim a$ (a) Extended states, (b) weakly localized states (L is mean free path).[3]

C. MAGNETICALLY DOPED SEMICONDUCTORS

In the late 1970s and early 1980s many materials were tested if a MIT was observed as the doping concentration was varied. For each material, a sample was prepared to check whether it was a metal or an insulator. The doping parameter was then altered to make another sample to measure the same physical property. The process of making different samples features one external parameter, which gives a discrete data set

that is available to tune the material through the MIT. In some studies, the densities of states for each sample were also measured by tunneling with a discretely varying doping parameter.[23]

In 1983, Hertel et al. measured the density of states and conductivity near the MIT as well as other physical properties of NbSi.[24] The group then sought out a method through which a sample could be tuned by an external parameter. Later, Dynes and coworkers substituted Nb with Gd to see a similar MIT, but gained an extra external control to drive the system through the MIT by magnetic field. By doping silicon, a prepared sample can be tuned and measured through the MIT. Gd_xSi_{1-x} has been rigorously studied and measurements of different physical properties like structure,[25] conductivity,[26,27] density of states,[28] magnetization,[29] specific heat,[30] the Hall effect,[31,32] optical/IR conductivity[33] and spin polarization[34] have been measured in the 3-D case. Other groups found it was possible to tune or drive the sample through the MIT using an external parameter like pressure (stress),[35] light (illumination of electro-magnetic radiation)[36] or magnetic field.[37]

As mentioned before, some materials can be driven through the MIT using external parameters, allowing for the measurement of the conductivity as a function of the external parameter such as magnetic field, illumination or pressure. In each case of an externally controlled MIT, one critical sample can be made that can be driven from an insulating phase to a metallic phase by varying an external parameter. It is also useful and important to measure the density of states during the MIT as it will give more

physical understanding of the mechanism that the system undergoes and how the external parameter alters the density of states (DOS).

One of the methods to measure the DOS in a system is to measure a tunnel conductance across a barrier. Of the external parameters mentioned above, only the magnetic field can be used successfully. In the case of an external parameter such as pressure (stress), the tunnel barrier may be destroyed. In the case of using light as an external parameter, the material is covered under the tunneling leads, always leaving doubt whether the material under the tunnel barrier is affected by the illumination or not. The best candidate for the external parameter is magnetic field, which can be used to measure the DOS without any experimental difficulties.

D. DILUTE MAGNETIC SEMICONDUCTORS

If a semiconductor crystal is doped with magnetic impurities, then the system shows both semiconducting and magnetic properties. In early 1970s there were numerous attempts to make samples with magnetic impurities to study the electron spin resonance in magnetic ions. Semiconductors doped with transition ions such as Mn^{2+} or Fe^{2+} were classified as dilute magnetic semiconductors.[38,39,40] In these systems the magnetic ion is randomly substituted in the crystal site with charge conservation. These crystals were also known as semi magnetic semiconductors or dilute magnetic semiconductors (DMS).[41] The magnetic ion changes the electric and magnetic properties of the parent crystal. Examples of change in properties are the spin Zeeman splitting, and

Faraday rotation. These significant changes in the physical property can be used in various optical and electrical devices for example magneto-optical drive.

The sample under study for this project is far from the regime of a DMS as the doping concentration of the magnetic material is larger than the transition ions used in the DMS mentioned above. In addition, most of the DMS doping elements only have unfilled d-shell electron(s), while for higher doping concentrations elements with f-shell electrons are preferred.

Gd[42] and Tb[43] are metallic, but their magnetic behaviors are very well described by the localized spins of the incomplete ionic f- shell, which interacts with a semiconductor like silicon. In summary, Gd_xSi_{1-x} demonstrates very rare physical properties that are interesting to investigate further in the dimensionality and the disorder limit near the QCR.

E. BRIEF SUMMARY

This dissertation is composed of eight chapters, starting with this introduction. Chapter II gives a brief introduction to the material under study, Gd_xSi_{1-x}, and provides the motivation for the experimental setup. Chapter III introduces an analytical solution of the Abrikosov-Gorkov theory and explains its usefulness for calculating the density of states for a superconductor in an external magnetic field. The solution will then be used in Chapter IV to extract spin polarization in a tunneling experiment. Chapter V describes the experimental setup and different components of the experiment and Chapter VI will

cover the calibration and measurement part of making the thin films. The results and analysis are covered in Chapter VII. Finally the last chapter will conclude with a summary of the issues and other problems faced during this work, which can be used as a reference for further research.

CHAPTER II

MOTIVATION

The introductory chapter explained the development of magnetically doped semiconductors and elaborated on how the resulting samples possess many interesting physical properties along with the roles they play in the theory of the metal-insulator transition (MIT). Chapter II introduces gadolinium$_x$silicon$_{1-x}$ (Gd_xSi_{1-x}), a magnetically doped semiconductor and shows different physical properties of it. This alloy shows a MIT phenomenon. Chapter II also gives a brief introduction to different theories explaining the phenomenon and motivates for the use of Gd_xSi_{1-x} for this study.

A. PHYSICAL PROPERTIES OF Gd_xSi_{1-x}

The variation of the concentration of gadolinium atoms in amorphous silicon, Gd_xSi_{1-x}, leads to a MIT as in Fig. II-1. The conductivity is very sensitive to the value of x (x is the fraction of gadolinium atoms in Gd_xSi_{1-x}). Figure II-1 shows that the fit for x = 14% has weak localization and Altshuler and Aranov type interactions.[44]

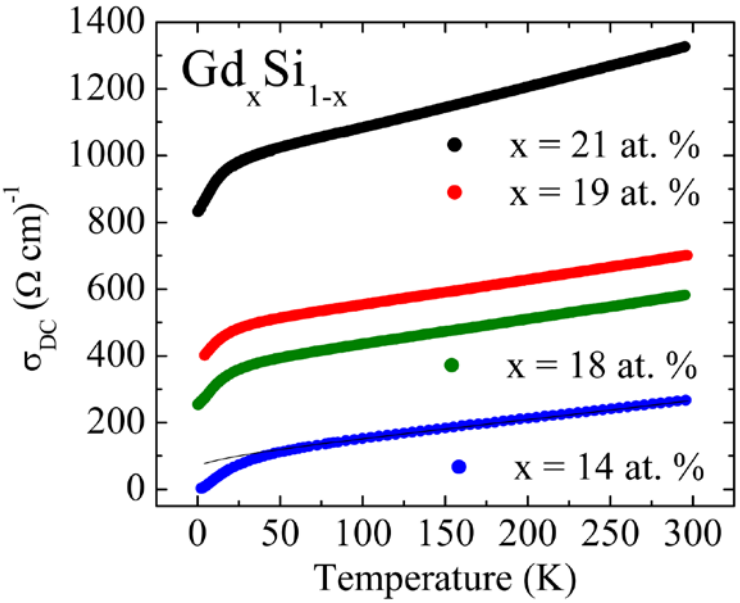

FIG. II-1. Conductivity of Gd_xSi_{1-x} for different values of x (from Ref.[45]).

A comparison conductivity of gadolinium doped silicon with the counter element yttrium doped silicon, which has almost the same atomic size but no magnetic property, clearly shows that affects of magnetic moment of gadolinium are at much higher temperature (Fig. II-2).

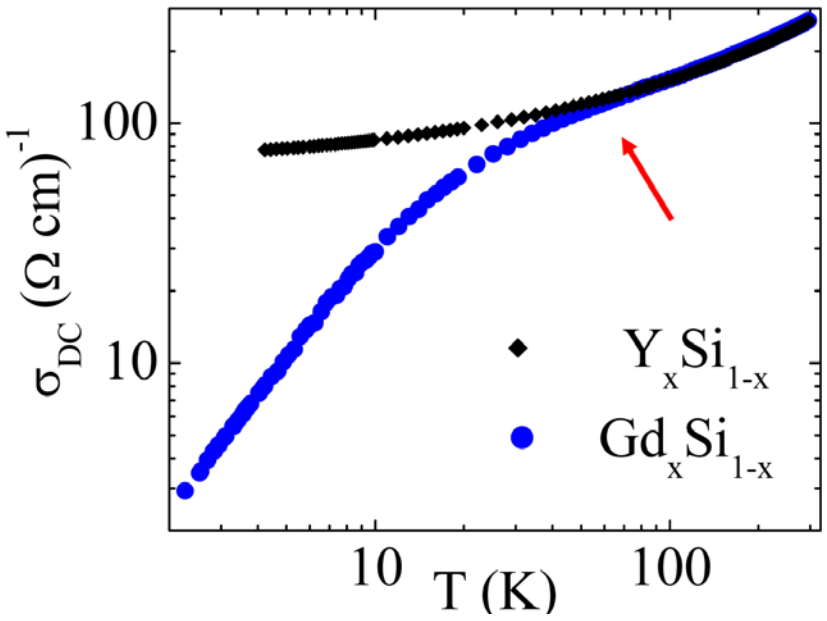

FIG. II-2. Conductivity of Gd_xSi_{1-x} and Y_xSi_{1-x} for same value of x.[45]

Bokacheva et al[27] prepared several Gd_xSi_{1-x} samples with different values of x, shown in Fig. II-3. Their samples show negative magneto resistance (NMR). In fact, sample (#3) which can be tuned from an insulator to a metal using a magnetic field and hence highlights the fact that Gd_xSi_{1-x} experiences a magnetically tuned MIT.

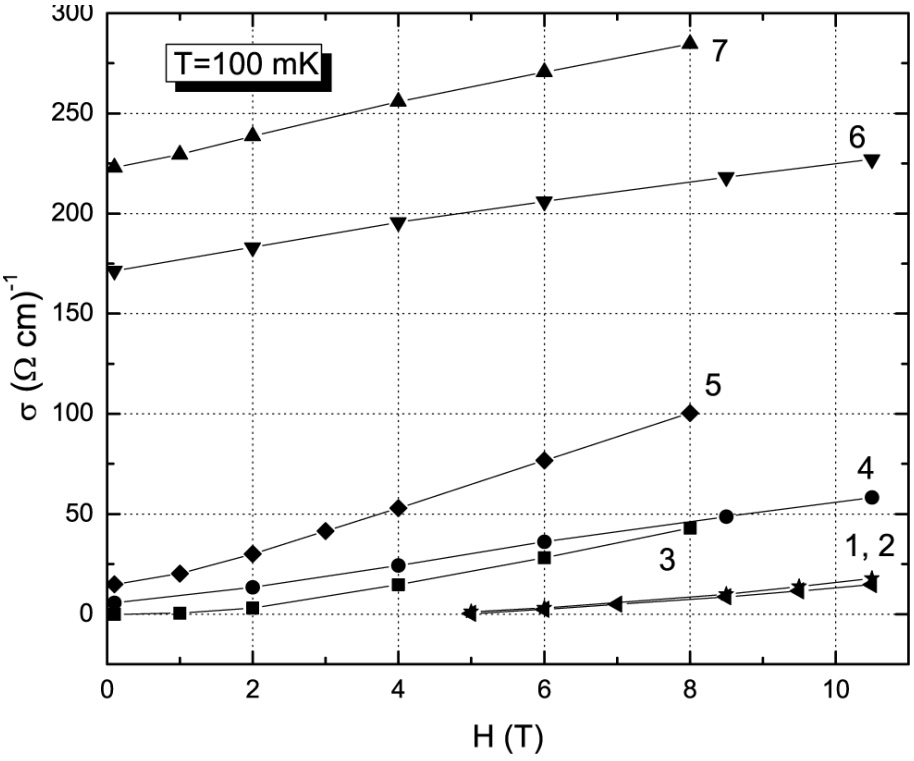

FIG. II-3. Low temperature conductivity $\sigma(H)$ of seven different samples versus the applied magnetic field. At H= 0.1 T samples #1 and #2 are insulating, sample #3 is at the transition, sample #4 and #5 are slightly metallic, samples #6 and #7 are in the metallic regime (from Ref.[27]).

To summarize, Gd_xSi_{1-x} is a special alloy that experiences a MIT if the value of x varies. For $x \approx 14\%$, it undergoes the MIT in an external magnetic field. Measured conductivities (Fig. II-3.) are below the Mott minimum conductivity [$\sim 500\ (\Omega\ \text{cm})^{-1}$] for all samples (more than two orders lower for some of them), and demonstrate strongly

correlated electron effects deep in the quantum critical regime. The material has disorder and strongly correlated electrons, which implies an Anderson-Mott transition.

Under these specific physical limits, Sample #3 was used for a tunneling experiment to understand the density of states of the system near the MIT, which will be described in Chapter III.

The unique set of properties mentioned above was also the motivation to understand and probe further into the MIT in 2-dimension (2-D); this study is aimed at better understand the basic theory of the electron-electron interactions. The experiment also helps to further understand the role of magnetic impurities and (or) external magnetic fields in a 2-D magnetically doped semiconductor.

In addition to properties mentioned above, normalized conductance measurements of thin Al/Al_2O_3/amorphous Gd_xSi_{1-x} planar tunnel junctions at T= 25 mK in an applied magnetic field, $H \leq 3.0$ T, display spin polarization. In contrast to previous attempts[34] using the Bardeen-Cooper-Schrieffer theory,[46] the Abrikosov-Gorkov theory[47] was applied to extract the spin polarization, which will be discussed in detail in Chapter III.

The Anderson-Mott transition shows a large change in the resistance in an applied magnetic field that is similar to colossal magneto resistance (CMR) but opposite in sign. The reason behind the CMR effect is not the same as in the Anderson-Mott transition. Gd_xSi_{1-x} shows negative magneto-resistance as compared to non-magnetic Y_xSi_{1-x}. Gd_xSi_{1-x} shows a unique convolution of the two theories in one sample.[48]

B. SCALING THEORY

MIT can also be understood by the most powerful theory of localization which is the scaling theory of Abrahams et al.[49] The basic concept of scaling theory is very simple. Assume there is a bag full of resistors. If two resistors with the same values of resistance are hooked together, then they are indistinguishable; that is, it does not matter which one is connected first. The underlying mechanism in the physical reasons for resistance is considered to be the same as for the density of states or disorder. Further, a larger scale resistor can be made using these resistors. If l identical resistors of resistance r are connected then the total resistance will be a function of r and l only.

To simplify it further, the resistors can be reduced to a basic quantum of resistance $R_H = h/e^2 \sim 25\text{K ohm}$.

Let the length of the material needed to have resistance R_H be l_0; then the resistance of any other length L of the same material can be related as

$$R_1(l)=R_1(l/l_0) \quad . \tag{II-1}$$

The main hypothesis of the scaling theory is that there is only one function $R_1(l)$, and the resistance of every quantum resistor changes with length.

To appreciate the power of the scaling theory, suppose the function of $R_1(l)$ is known, then whatever material is used, if the resistance for a given length is known, the resistance for any desired length can be derived. The one functional dependence hypothesis can be extended to two and three dimensions, as well, though the way these resistors will be hooked together is slightly different. The resistance of a square with side length L can be written as $R_2(L)=R_2(L_0/L)$ and the same way for 3-D. More generally, for a dimension d, dependence can be written as $R_d \sim L^{(d-2)}$.

In d=1 and d=2, there is no problem supporting that R rises monotonically with L, but in d=3, R shrinks as a function of L when it is small and is very large when L is large. To guess the function, Abrahams proposed a function that is not related to resistance but to the conductance $g \sim 1/R$ of the material.

$$\beta(g(L) = \frac{\partial \ln g(L)}{\partial \ln L} \tag{II-2}$$

Figure II-4 shows the prediction of Eq. (II-2) for different dimensions.

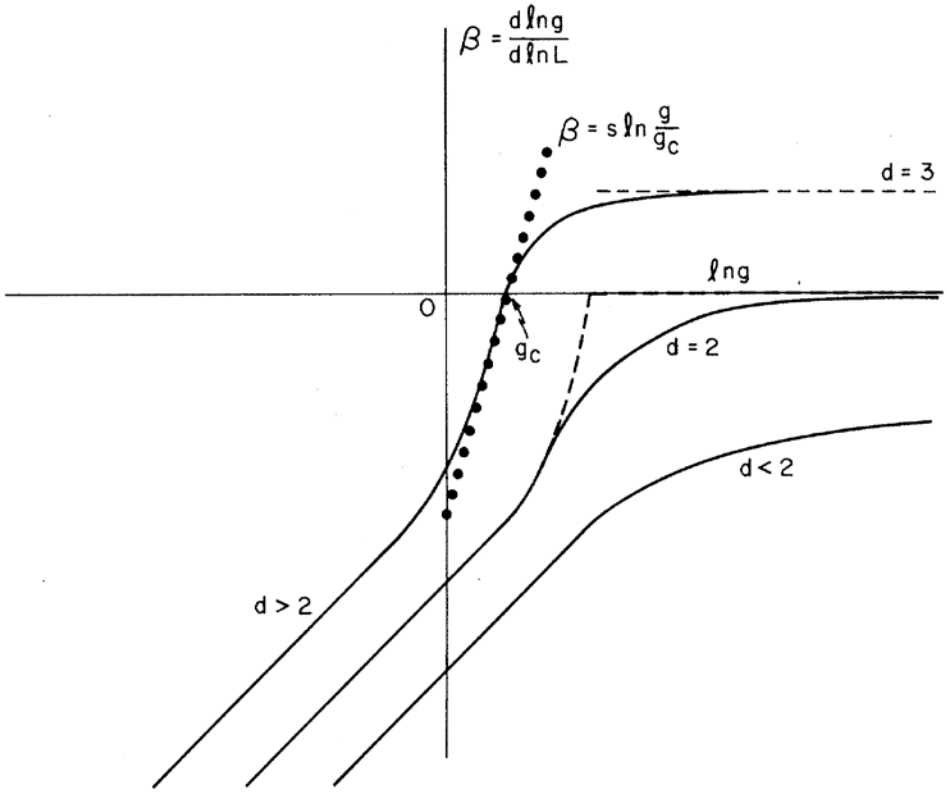

FIG. II-4. Plot of $\beta(g)$ vs. $\ln(g)$ for $d > 2$, $d = 2$, $d = 3$. g(L) is normalized 'local conductance." The approximation $\beta = s\ln(\frac{g}{g_c})$ is shown for $d > 2$ as the solid-circled line; the unphysical behavior necessary for a conductance jump in d=2 is shown dashed.

Fig II-4. shows that there is only one critical point with the cross-over on the y=0 axis. According to the scaling hypothesis, the MIT is possible only when d=3. The observation of a MIT at B=0 and in 2 dimensions[50] gave an indication that Abrahams[49] theory does not include all mechanisms and considers only non interacting electron system. Punnoose and Finkelstein[51] included electron-electron interaction at low

temperature with the disorder. They showed that in the presence of impurities, the charge perturbation and the spin densities relax diffusively over a large distance. In highly correlated systems, either electron-hole interactions (defined as cooperon), or electron-electron interaction (defined as diffuson) can occur between two electrons with each quasi particle having its own channel to interact and conduct.

In Gd_xSi_{1-x}, when a magnetic field is applied to the sample, disorder from the magnetic impurity (Gd) is reduced. The applied magnetic field orients the magnetic impurity and results in a reduction in randomness. In turn, the reduction in randomness leads to a reduction of the localization of the electrons, and eventually the conductivity is increased. The magnetic field indirectly controls the degree of disorder in the system, which is rarely observed in other systems.

As the system is reduced to 2-D, the effects of both quasi particles start showing up in different ways. Each channel (interaction mode) is affected by the magnetic impurities and the external magnetic field. It is crucial to know the spin relaxation and scattering amplitudes to understand the system. Dimensionality defines the relation between the conductivity of the sample and the temperature. The conductivity is a logarithmic function of temperature in 2-D and a square root function in 3-D. We attempted to probe the 2-D MIT Gd_xSi_{1-x}.

In recent years, the MIT of semiconductors and amorphous metal-semiconductor mixtures has been considered an example of a continuous quantum phase transition with certain scaling properties. The scaling theory of the MIT describes the critical behavior

of a system by an analogy with second order phase transitions, on the basis of power functions of the coherence length.

$$\xi = \left| 1 - n/n_c \right|^{\nu} \tag{II-3}$$

The scaling theory deals with the spatial scale (size) of the correlation length in a critical region where it increases infinitely. In the critical region, the system's local properties do not play an important role, and the correlation length (diverging at $T \rightarrow T_t$) is the only parameter that defines the phase transition (where T_t is the transition temperature). The same behavior of ξ in a doped semiconductor is observed for $n \rightarrow n_c$, and the value of ξ is equal to the localization radius R on the insulator side of the transition. On the metallic side, σ, the conductivity goes to zero as $n \rightarrow n_c$ as given by Eq. (II-4).

$$\sigma \approx (1 - n/n_c)^{\mu} \tag{II-4}$$

The exponent μ in Eq. (II-4) is related to the correlation length exponent, ν, and the dimensionality[6], *d.* given by Eq. (II-5)

$$\mu = \nu(d - 2) \tag{II-5}$$

The relation predicts that the MIT (Anderson) is a continuous phase transition and the conductivity of the doped semiconductor has the form of Eq. (II-4). Thus, scaling theory is an important tool to extract physical information about the system at MIT, which is dependent on the dimensionality of the sample and the type of element (magnetic or non magnetic) introduced in the semiconductor.

C. QUANTUM PHASE TRANSITION

Quantum phase transitions (QPT), from insulator to superconductor or from insulator to metal, depend only on disorder or external magnetic field and are independent of temperature, as opposed to processes like the melting of ice. In the QPT scenario, the tuning parameter transforms one quantum mechanical system to another, e.g., from a localized to an extended electronic state. All quantum phase transitions are observed at absolute zero temperature and are thus governed by the quantum critical point at $T = 0$.

D. DIMENSIONALITY EFFECT ON PHYSICAL PROPERTY

D.1. ONE DIMENSIONAL EFFECTS

According to Peierls theorem, a true one-dimensional metal does not exist as its fermi surface is destroyed by periodic lattice distortions that change the crystal periodicity.[52] But it is not obvious that a periodic lattice distortion is energetically favorable, as it will be opposed by the elastic energy resulting from the short-range forces caused by the periodicity in the lattice. Thus an appropriate Peierls distortion can destroy the metallic behavior in a 1-D lattice. In addition, according to Peierls theorem, in a 1-D system, electronic perturbation always destroys the conductivity. However, it is

possible to have a 1-D superconductor, which allows a temperature induced superconductor-insulator transition in one-dimensional systems.

D.2. TWO AND THREE DIMENSIONAL EFFECTS

To understand the interaction of the electrons in strongly doped semiconductors, it is important to include all possible interactions between the electrons, such as lattice disorder, band structure, polarons, binding to defect sites, and Coulomb forces.

Initially it was predicted that a MIT would not occur in a 2-D system with disorder, [49] or in other words, no quantum diffusion of electrons would take place in 2-D in a disordered system at zero temperature. Even a small disorder will trap electrons and no net current will be produced. The scaling theory does not include any interaction between electrons, but highly correlated electrons have been shown to lead to a MIT in 2-D systems.

Another way to look at a MIT is through topological defects. In 1-D any one defect will lead to a bound state and prohibit conductivity through the system. Using the same reasoning in 2-D, no topological path is likely to avoid defects and make the system conductive. The defects will have exponentially decaying bound states throughout the system hence no conductivity. Whereas in 3-D, some topological path around the impurities or defects should be able to lead to a conductive path but still have local bound states.

CHAPTER III

ANALYTICAL SOLUTION OF ABRIKOSOV-GORKOV THEORY*

A. INTRODUCTION

The basic microscopic theory of superconductivity by Bardeen, Cooper, and Schrieffer[46] (BCS) is based on the pairing of electrons with opposite physical properties such as momentum and spin, and leads to various spin-dependent properties. The original BCS theory was formulated in such a way that it covers only homogeneous superconductors and excludes superconductors with either intrinsic or extrinsic inhomogeneous states. Yosida[53] showed that the spin susceptibility of superconductors goes to zero as the temperature reaches zero. Subsequently, Chandrasekhar[54] and Clogston[55] identified an upper limit of the critical magnetic field for a thin film of a superconductor whose thickness approaches zero. Fulde[56] noted that the density of states (DOS) for the quasiparticles splits into separate densities of states for each spin population.

The DOS of a clean conventional superconductor is customarily described by BCS theory through a model of paired electrons. Bogoliubov et al.[57] and Valatin[58]

---

*Part of this chapter is reprinted with permission from "Analytical density of states in the Abrikosov-Gorkov theory" by R. V. A. Srivastava and W. Teizer, 2008. Solid State Comm, 145, 512-513, Copyright © 2007 Elsevier Ltd.

independently found a canonical transformation of the Hamiltonian, thus simplifying the mathematics of the BCS theory. Using the canonical transformation, Abrikosov et al.[59] decoupled the Green's functions equations of motion to extend BCS theory for external potentials and gauge invariance.

Reif[60] had shown a shift in the nuclear magnetic resonance frequency (Knight shift) in mercury before the publication of the BCS theory. Thereafter the same effect was shown for tin,[61] vanadium,[62,63] and aluminum.[64] Ferrell[65] and Anderson[66] suggested that the spin-orbit interaction is of a general kind, which affects the spin states and the pairing between the time-reversed states. Finally, Abrikosov and Gorkov[67] (AG) further improved BCS theory to develop a general theory for superconductors.

The AG theory has been used to describe superconductors with paramagnetic impurities. This chapter introduces an exact analytical solution to the above framework and shows the solution is valid in the whole regime of the AG theory independent of the presence of an energy gap. The solution has computational benefits in the evaluation of integrals for tunneling conductances and allows for an analytic description of materials with densities of states that are modeled from the basic AG density of states.

Abrikosov and Gorkov[67,68] used the BCS model interaction and described the impurities as point scattering sources with short-ranged effects. These impurities can change the electromagnetic properties of superconductors by removing the anisotropy, changing the electronic density of states and even altering the effective interaction.[69] The exchange interaction between the impurity spins and conduction electrons give an indirect exchange coupling between the impurity spins that can lead to magnetic

ordering at low temperature.[70,71] AG theory assumes that the interactions between impurity spins are negligible, and the impurity potential is assumed to be short-ranged; the correlations between the impurities are negligible.

The AG DOS typically is derived by numerically evaluating the solutions to a complex, fourth-order polynomial:

$$u^4 - 2u^3\xi + u^2\left(\xi^2 + \alpha^2 - 1\right) + 2u\xi - \xi^2 = 0\,, \qquad \text{(III-1)}$$

where ξ represents the energy difference to the Fermi energy and α is a free parameter. One of the roots u (selected according to the boundary conditions) is then used to numerically construct the DOS, ρ, according to

$$\rho = N(u) = \mathrm{Re}\left[\frac{u}{(u^2-1)^{1/2}}\right]. \qquad \text{(III-2)}$$

The approach is quite inconvenient and requires significant computational power in projects where finite temperature requires numerical evaluation of folding integrals with Fermi functions, such as in the case of evaluating tunneling conductances. No analytic expression of the AG DOS has been described to date.

B. RESULTS

Despite the recent efforts[72] to achieve a specific microscopic understanding of superconductors with paramagnetic impurities, there was an absence of an exact DOS expression in AG theory, which is important for ongoing work in several systems.[70,73,74]

Srivastava and Teizer constructed[75] an analytical solution for the AG DOS from an analytic form for *u*, which was found as an explicit solution of Eq. (III-1):

$$u = \frac{1}{6}\left(3\xi + \sqrt{3}\sqrt{\left(A + \frac{B}{E} + E \right)} - \sqrt{3}\sqrt{\left(2A - \frac{B}{E} - E - \frac{6\sqrt{3}\left(1+\alpha^2\right)\xi}{\sqrt{\left(A + \frac{B}{E} + E \right)}} \right)} \right), \qquad \text{(III-3)}$$

where the values of A, B, C, D and E are given as:

$$\begin{aligned} A &= 2 - 2\alpha^2 + \xi^2, \\ B &= \left(-1 + \alpha^2 + \xi^2\right)^2, \\ C &= -1 + \alpha^6 + 3\xi^2 - 3\xi^4 + \xi^6 + 3\alpha^4\left(-1+\xi^2\right) + 3\alpha^2\left(1 + 16\xi^2 + \xi^4\right), \\ D &= 6\sqrt{3}\sqrt{\alpha^2\xi^2\left(\alpha^6 + 3\alpha^4\left(-1+\xi^2\right) + \left(-1+\xi^2\right)^3 + 3\alpha^2\left(1 + 7\xi^2 + \xi^4\right)\right)}, \\ E &= \left(C + D\right)^{1/3}. \end{aligned} \qquad \text{(III-4)}$$

Eq. (III-1) has four solutions which exist in pairs of complex conjugates. Out of these two sets of complex conjugate solutions one set is discontinuous and is therefore abandoned as unphysical. The other conjugate pair of complex solutions leads to the same AG DOS in Eq. (III-2). Eq. (III-3) is that choice of the complex conjugate pair which results in a positive DOS. The expression can readily be introduced into Eq. (III-1), leading to an identical cancellation and thus constituting a solution to the equation. In Eq. (III-4), the order parameter is α, and varying the value of α produces different AG DOSs. Depending on the value of α, the system can be in a gapless regime ($\alpha > 1$) or a regime with gap ($\alpha < 1$). For α equal to zero, the system reverts to the standard BCS model. Figure III-1 shows plots of $\rho = N(u)$ (using *u* from Eq. (III-3)) versus ξ which are reminiscent of numerical solutions used for decades;[76] however, the curves shown are

representations of the exact analytic solutions Eq. III-3. The analytical solution to the AG theory facilitates the construction of more complex theoretical DOSs, including combinations of several AG DOS and other superconducting systems.

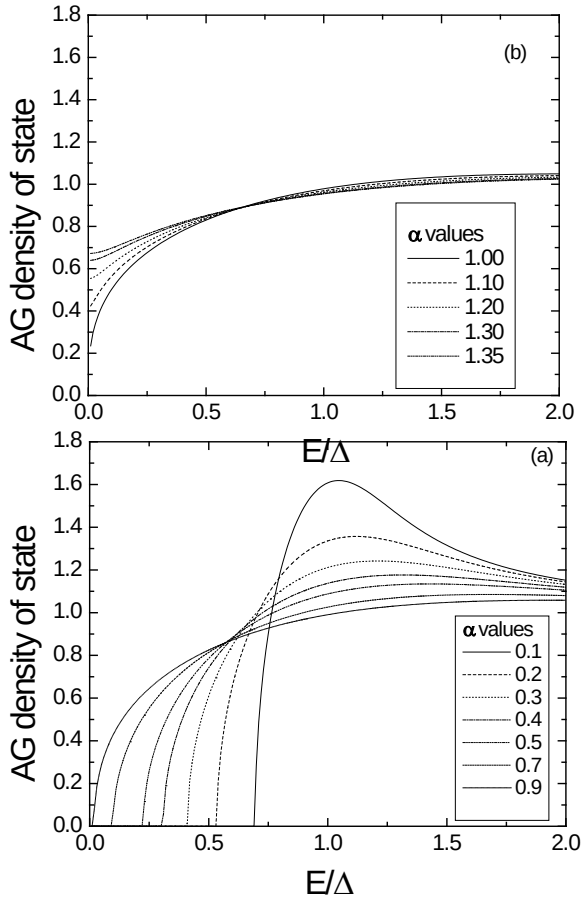

FIG. III-1. AG density of states vs. normalized energy for different values of α, (a) $\alpha < 1$, and (b) $\alpha \geq 1$.

In addition, Eq. (III-3) does not require a verification of the solution's independence of the numeric process. The general analytic form with free parameters ξ

and α is a significant step forward from the numeric evaluation. (Appendix A shows the analytical form and computed AG density of states.)

CHAPTER IV

EXTRACTION OF SPIN POLARIZATION NEAR THE METAL-INSULATOR TRANSITION USING ABRIKOSOV-GORKOV DENSITY OF STATES*

A. INTRODUCTION

The metal-insulator transition (MIT) is a very interesting phenomenon used to observe a quantum phase transition (at T=0 K). To explore the MIT in the quantum critical regime (QCR), a reversible tunable sample in an external magnetic field H was used. From previous work, conductivity, density of states, magnetization, specific heat and the Hall Effect were obtained. The Abrikosov-Gorkov (AG) theory was used to extract the spin polarization for a 3-D $Al/Al_2O_3/a\text{-}Gd_xSi_{1-x}$ at T = 25 mK and in different external magnetic fields.

B. SAMPLE PREPARATION

A (5 nm) thin aluminum (Al) film was thermally evaporated, and then a thin native oxide layer was grown by exposing the film to atmosphere for approximately 30 min. On top of the oxide layer, 100 nm of gadolinium (Gd) and silicon (Si) were

---

*Part of this chapter is reprinted with permission from "Using AG theory to model a S/I/N tunnel junction"by R. V. A. Srivastava,W. Teizer, F. Hellman and R. C. Dynes, 2008. Solid State Comm, 403, 1321-1322, Copyright © 2007 Elsevier Ltd.

co-evaporated using dual e-beam evaporation in high vacuum. As a result, a planar tunnel junction with Al_2O_3 as a tunnel barrier was produced. Bulk $Al/Al_2O_3/a\text{-}Gd_xSi_{1-x,}$ with proper values of x (≈14%) and application of an external magnetic field can be changed from an insulating to a metallic material.[77]

C. TUNNELING THEORY

To measure the density of states of a system, a tunneling experiment was employed, as the tunneling conductance is proportional to the DOS. There are different types of tunnel junctions that can be used for tunneling experiments: superconductor-superconductor tunnel junctions (SS), superconductor-normal metal tunnel junctions (SN), as shown in Fig. IV-1, and normal metal-normal metal tunnel junctions (NN).[78] The sample was designed with one superconducting counter electrode made of thin Al and another made of Gd_xSi_{1-x}, which is an SN tunnel junctions.

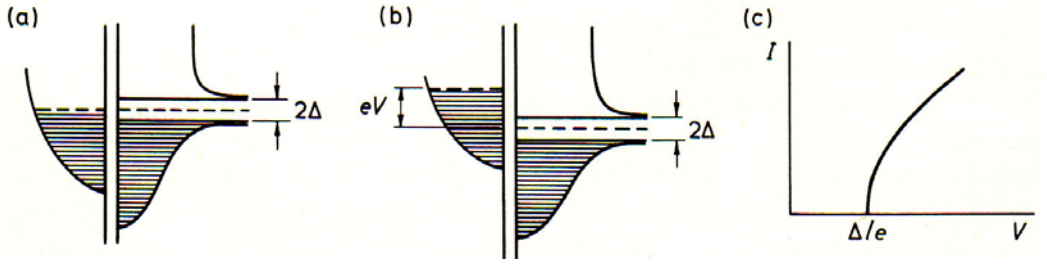

FIG. IV-1. The energy diagram of an SN junction in the semiconductor representation; (a) V=0, (b) $V>\Delta/e$, (c) the I-V characteristic at T = 0.[79]

Tunneling between a superconductor and a normal metal is given by Giaver and Megerle.[80]

In this case the tunneling current I_{SN} is given by

$$I_{SN} = C_N \int_{-\infty}^{\infty} \rho_S(E)\left[f(E) - f(E+ev)\right]dE\,, \qquad \text{(IV-1)}$$

Where C_N, the conductance between the metals when the superconductor is in the normal metal state, is given by,

$$C_N = (2\pi e/\hbar)\left|M\right|^2 N_N(0)N_S(0)\,. \qquad \text{(IV-2)}$$

M is the tunneling matrix element, $N_N(E)$ is the density of states of the normal metal and $N_S(E)$ is the density of states of the superconductor in the normal state.

The normalized conductance of the junction $G(V)$ is given by

$$G(V) = \frac{dI_{SN}}{dV} \Big/ \frac{dI_{NN}}{dV} = \int_{-\infty}^{\infty} \rho_S(E)\left(\frac{\beta e^{\beta(E+eV)}}{\left(1+\beta e^{\beta(E+eV)}\right)^2}\right)dE\,, \qquad \text{(IV-3)}$$

At T=0 the function degenerates into a δ function and $G(V)_{T=0} = \rho_S(eV)$, thus at T=0 the measured conductance is exactly proportional to the superconducting density of states. In a finite temperature range but still in a superconducting regime, the kernel of the integral is still sharply peaked and the conductance measured is the density of states with some broadening due to temperature.[81]

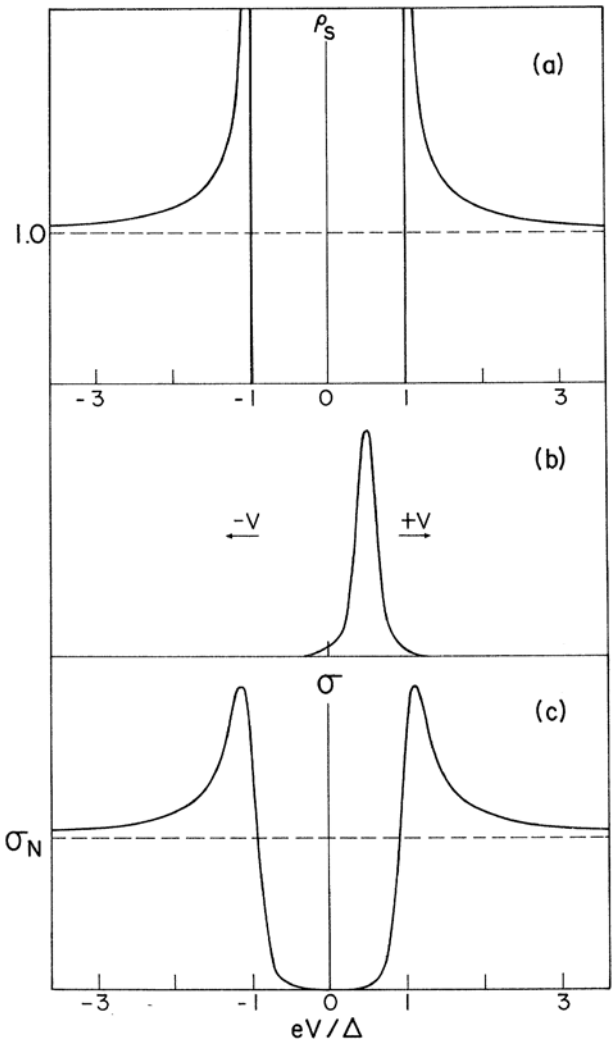

FIG. IV-2. Superconductor-normal-metal tunneling. (a) BCS density of states as function of voltage. (b) Temperature-dependent kernel in the integral expression for the conductance. (c) Theoretically normalized conductance σ.[81]

Figure IV-2 shows the effect of temperature on the density of states which is symmetric near Fermi energy. Spin polarized tunneling will be discussed in detail in spin polarization section.

D. EXPERIMENTAL SETUP

The tunnel plane of the sample was aligned in-situ with the external magnetic field to < 1°. The tunnel junction was subjected to an external magnetic field from two specific directions. One direction is parallel to the planar junction and another direction is at an angle of 45° to the plane of the tunnel junction. In the parallel case, an appropriate magnetic field was used such that the thin Al remained superconducting, whereas in the 45° case superconductivity is quenched as shown in Fig. IV-3. With a parallel magnetic field, the junction is an SN tunnel junction, and with a magnetic field at 45°, the junction is an NN tunnel junction. The ratio of a tunnel conductance of an SN junction (parallel magnetic field) with a tunnel conductance of an NN junction (magnetic field at 45°) gives the density of states of the superconducting thin Al with the affect of the spin polarization of Gd_xSi_{1-x} as will be discussed in more detail in section spin polarization.

For $H \leq 1.5$ T, the a-Gd_xSi_{1-x} is insulating and the conductance is too small to be measured accurately. $H > 3.0$ T quenches the superconducting behavior of Al. Thus, in a small range of external magnetic field the spin polarized tunneling conductance can be observed and the polarization extracted. The data collected for different magnetic fields displayed an asymmetric tunneling conductance.

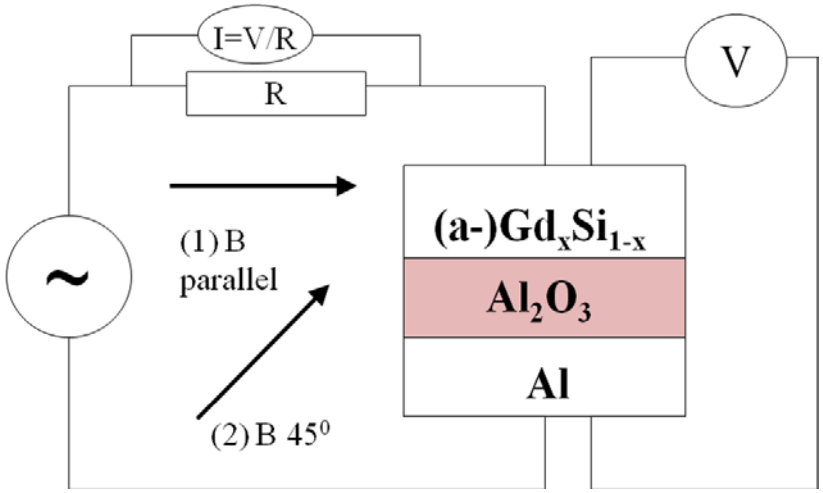

FIG. IV-3. Schematic diagram for the experimental measurement set up and magnetic fields direction.

E. INITIAL ATTEMPTS TO EXTRACT POLARIZATION

E.1. USE OF BCS DENSITY OF STATES

The main observation by Cooper[82] was that if two electrons were excited slightly above the fermi sea, they could form a bound state which leads to the BCS theory. The electron phonon interaction provides a weak attractive potential. The bound state has lowest energy if its net momentum is zero, i.e., if the wave function is composed of two electrons with equal and opposite momentum. The BCS density of states is given by the following equation:

$$\frac{N_s(E)}{N(0)} = \begin{cases} \mathrm{Re}\left(\dfrac{E}{(E^2 - \Delta^2)^{1/2}} \right) & (E > \Delta) \\ 0 & (E < \Delta) \end{cases} \qquad \text{(IV-4)}$$

where Δ is the gap parameter or 2Δ is the energy gap. Figure IV-4 shows the BCS DOS. Numerical graphs are truncated at the boundary (as explained in Appendix B).

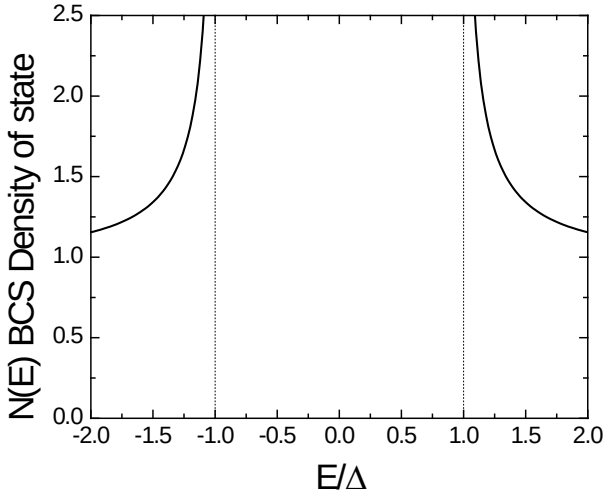

FIG. IV-4. BCS density of state vs. normalized energy.

Fig. IV-4. clearly shows that no states exist within the gap ($|E|<\Delta$) and singularities occur at the gap edges ($|E|=\Delta$). Far from the gap edge ($|E|>>\Delta$), the density of states asymptotically approaches 1.

E.2. SPIN POLARIZATION (SP)

If the population of spin up electrons and spin down electrons are different, then the net polarization in the system is defined as:

$$P = \frac{n_{\uparrow} - n_{\downarrow}}{n_{\uparrow} + n_{\downarrow}} \qquad \text{(IV-5)}$$

where, $n_{\uparrow}$ = number of electrons with spin up, $n_{\downarrow}$ = number of electrons with spin down and $n_{\uparrow} + n_{\downarrow}$ = total number of electrons.

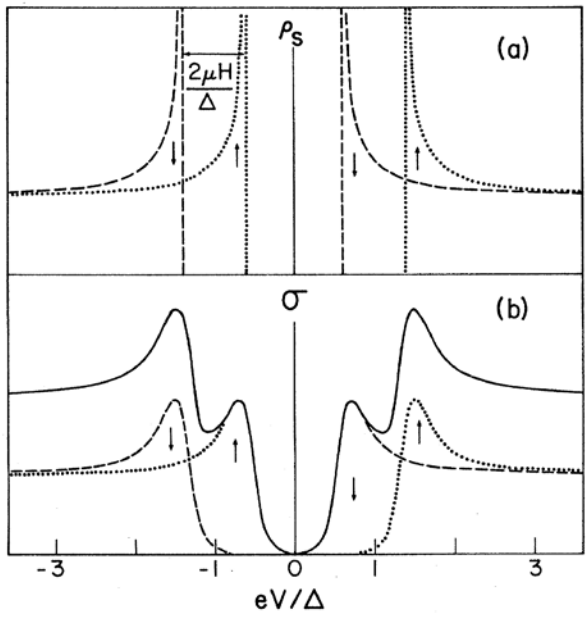

FIG IV-5 . (a) Magnetic field splitting of the density of quasiparticle states into spin-up (dotted) and spin-down (dashed) densities. (b) Spin-up conductance (dotted), spin-down conductance (dashed), and total conductance (solid line).[81]

Figure IV-5 shows that in a magnetic field there is no asymmetry in the net normalized total conductance. To fit the asymmetry in the experimental data we included a polarization in the system.

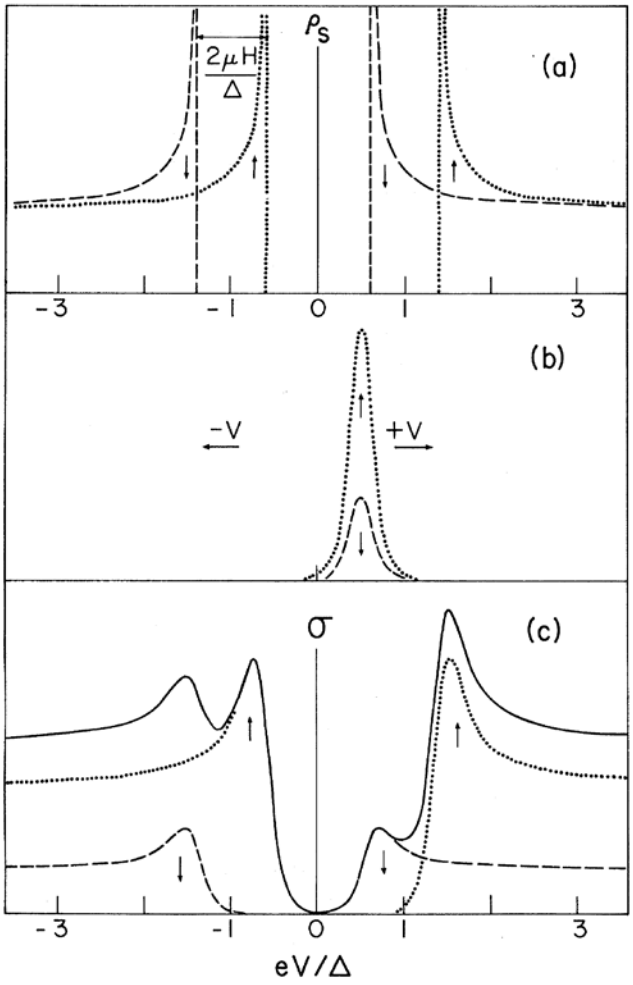

FIG. IV-6 (a) BCS density of states of a superconductor as a function of voltage in a magnetic field. (b) Temperature-dependent kernels for each spin direction in the integral expressions for conductance. (c) Theoretical normalized conductance for each spin direction (dotted and dashed curves) and the total conductance (solid line).[81]

The asymmetry in Fig. IV- 6(c) is due to the polarization in the normal side of the tunnel junction, i.e. in the normalized tunnel conductance measured in $Al/Al_2O_3/a\text{-}Gd_xSi_{1-x}$ it is due to Gd_xSi_{1-x}. In the next section we will show steps to extract the spin polarization from the normalized tunnel conductance.

E.3. USE OF SPIN POLARIZED BCS DENSITY OF STATES

After including polarization (P), thermal effects, Zeeman Effect, and lifetime effects of quasiparticles (Γ)[83], the BCS DOS (Eq. (IV-4)) becomes a spin polarized (SP) BCS DOS (Eq. (IV-6)), which is normalized with a tunneling conductance at T=0. Using Eq. (IV-6) a SP BCS DOS is plotted as shown in Fig. IV-7. Only the polarization factor can lead to an asymmetry in the DOS.

$$\frac{dI}{dV} = \frac{(1-P)}{2}\int \left| \mathrm{Re}\frac{(E - i\Gamma + \mu H)}{\sqrt{(E - i\Gamma + \mu H)^2 - \Delta^2}} \right| \left[-\frac{\partial f(E+eV)}{\partial (eV)} \right] dE + \frac{(1+P)}{2}\int \left| \mathrm{Re}\frac{(E - i\Gamma - \mu H)}{\sqrt{(E - i\Gamma - \mu H)^2 - \Delta^2}} \right| \left[-\frac{\partial f(E+eV)}{\partial (eV)} \right] dE \qquad \text{(IV-6)}$$

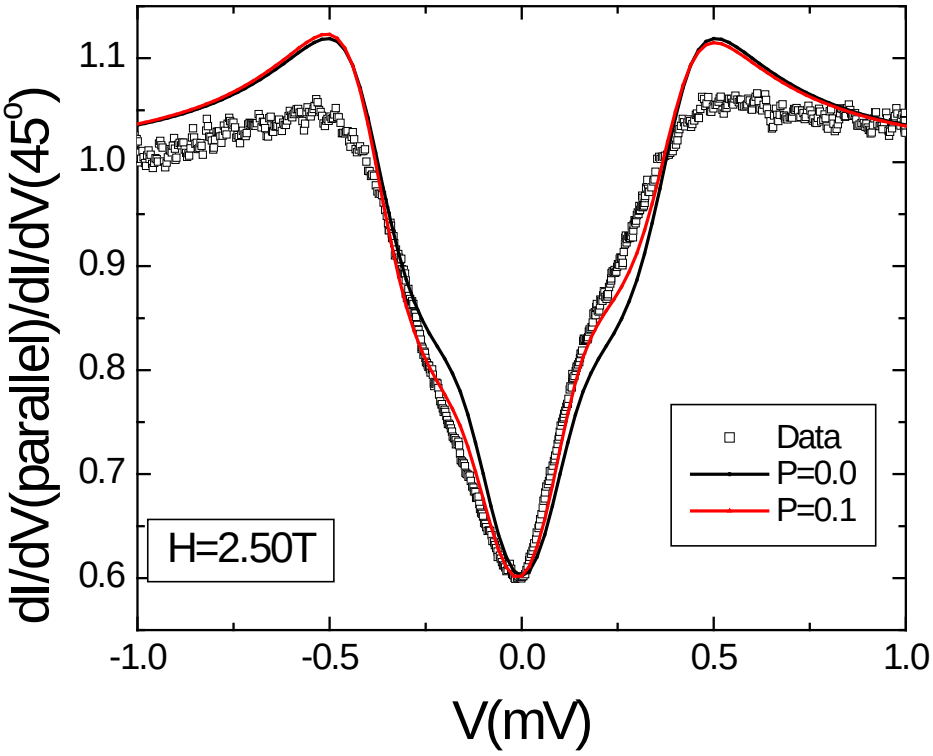

FIG. IV-7. Spin polarized tunneling data and fits at T = 25 mK and H = 2.5 T. The fits assume a spin polarized BCS density of states. The black curve fit is for no polarization, the red curve is for P = 0.10. The asymmetry of the data is better fit by $P \sim 0.10$.[34]

F. FURTHER ATTEMPTS TO EXTRACT THE POLARIZATION

Use of a SP BCS DOS does not properly fit the data at the gap edge, as shown in Fig. IV-7.

There are three well-known experimental methods of determining the polarization in a given system: (1) spin-polarized photoemission,[84] (2) Andreev reflection[85] and (3) spin-polarized tunneling.[86] Giaever[87] first introduced tunneling measurements in superconductors which allowed for the measurement of properties such as the density of states,[88] the de-pairing effect, and the phonon spectrum.[89] SP tunneling was subsequently established by Meservey and Tedrow.[90]

Maki[91] extended the effect of Pauli paramagnetism on superconductors to an arbitrary temperature using the results given by Clogston[55] and Chandrasekhar[54]. He found interesting outcomes for Abrikosov's mixed state using the generalized Ginzburg-Landau equation including Pauli terms in the general Gorkov equation, also known as the Maki equation,[92] and is particularly useful for extremely thin film (thickness d~10 Å). We used AG theory instead of Maki's equation due to the thickness of the amorphous Al sample.

In prior work, Teizer et al [34] implemented SP BCS DOS to find the polarization within a system but did not achieve a satisfactory result.

F.1. USE OF ABRIKOSOV- GORKOV DENSITY OF STATES

According to the AG theory, paramagnetic impurities do not affect the excitation spectrum of a superconductor in any magnetic field.[68] Maki[93] and Maki and Fulde[94] showed that an essentially identical DOS can describe a superconductor in a high magnetic field and a superconductor with nonmagnetic impurities. We have assumed that the samples have nonmagnetic impurities. Thus, in a magnetic field these impurities can be treated as paramagnetic impurities.

F.2. NUMERICAL METHOD

As the concept of numerical method implies, no exact expression is possible for some independent variables. The method generates discrete values of the expression for specific values of independent variables. In the AG theory, we get individual values of u for the specific value of α and ξ, as given in Eq. (III-1). These u values are then used to find the AG DOS as given in Eq. (III-2). Numerical methods allow the computation of discrete values of the DOS with discrete values of ξ and α. Including an effect of Fermi distribution over these DOSs requires numerical integration over discrete values; these integration results depend on the increment of the discrete density of states.

F.3. USE OF ANALYTICAL SOLUTION

To circumvent the process above, we have found an analytical solution for the AG density of states.[75] The analytical method has advantages over the numerical method as it does not depend on the iteration value of ξ. Appendix C describe further benefits of the analytical solution.

In Fig. IV-7, a fit can be obtained either at E=0 or at |E|=Δ, but not fit well in both regions simultaneously. Paramagnetic impurities affect the excitation spectrum of a superconductor as given by the AG theory. As can be seen in Fig. IV-4, the experimental density of states is less than the BCS DOS at the gap edge. Achieving a better fit of the experimental DOS requires a model that has a lower DOS at the gap edge. At zero temperature, the AG theory has a lower DOS at the gap edge, so we used the AG DOS with a Fermi distribution and including the Zeeman split to model the DOS. Figure IV-8 shows the effect of temperature on the AG DOS with the Zeeman shift.

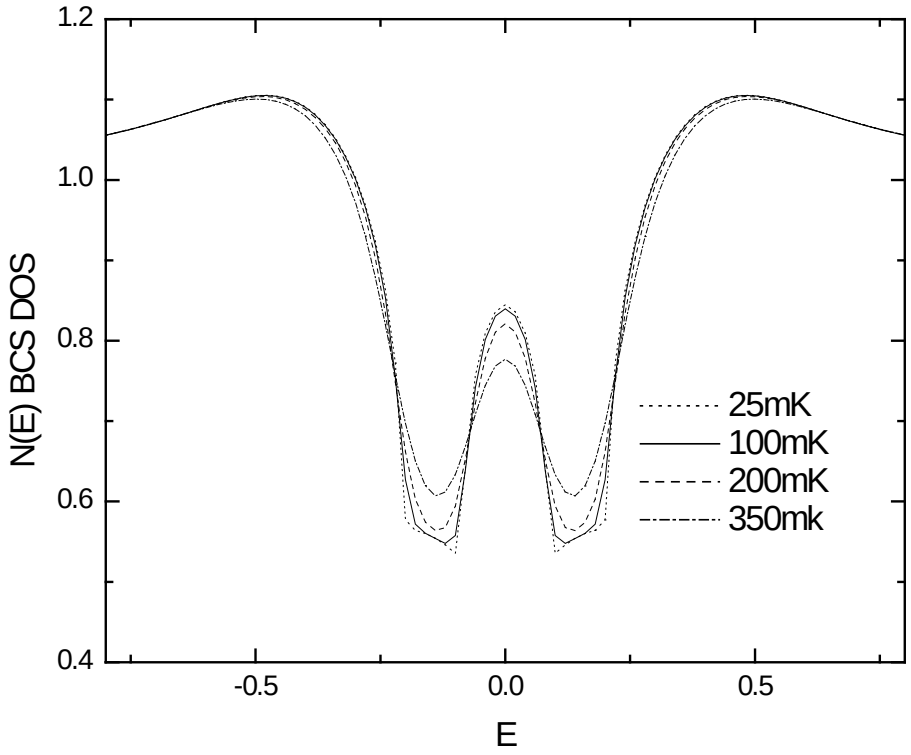

FIG. IV-8. AG DOS with the Zeeman shift at T=25 mK, 100 mK, 200 mK and 350 mK.

An increase in temperature smoothes the edges of the DOS plot. Γ cannot be included in the AG theory as the AG DOS depends on *u*, a complex root of Eq. (III-1). Including *Γ* as the imaginary term, as in the BCS approach, yields unreasonable results.

The only parameter that allows for control of the sharpness vs. smoothness of the data is temperature. Achieving smooth data, as observed in the experiment, requires a higher temperature than in the case of BCS.

F.4. PURE ZEEMAN SYSTEM (PZS)

The only way to include asymmetry in normalized tunneling conductance is to include polarization in the DOS. If the electron population splits into two independent carrier populations, then the net AG DOS is given by Eq. (IV-7):

$$N_1(u) = \frac{1-P}{2} N(u+\mu H) + \frac{1+P}{2} N(u-\mu H) \qquad \text{(IV-7)}$$

$N(u\pm\mu H)$ is the standard AG density of state as given by Eq. (III-5). Figure IV-9 shows the Zeeman shift in AG theory and the combined AG DOS. The net AG DOS is sum of two Zeeman shifted AG DOSs and has a bump at the gap (at T =900 mK).

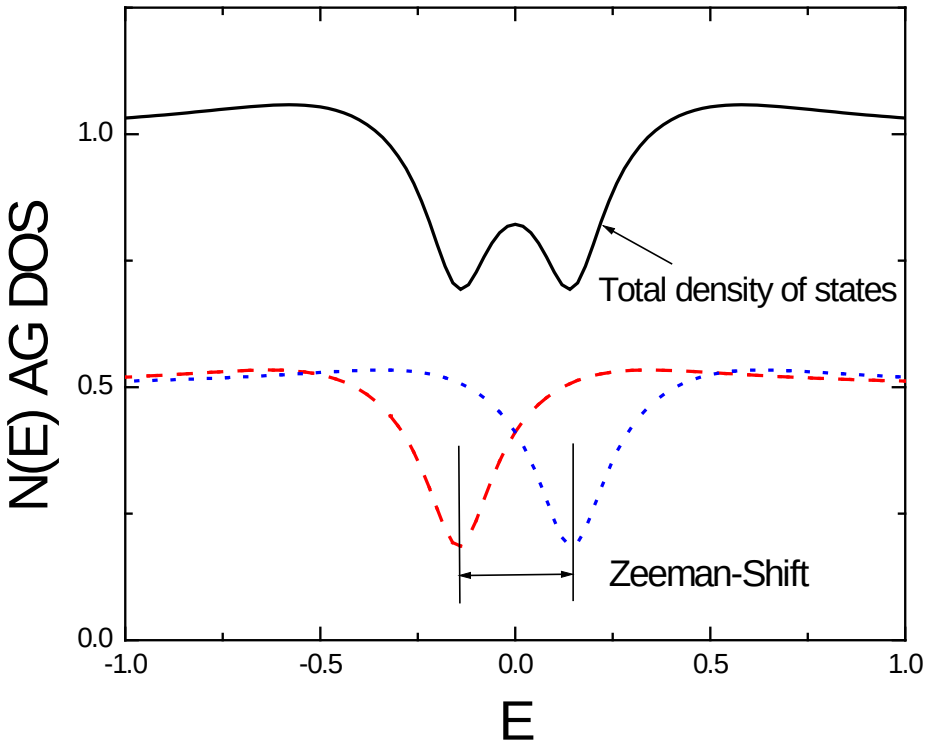

FIG. IV-9. Zeeman Shift and combined AG density of states versus energy.

If only the polarization is included, the fit at E=0 as shown in Fig. IV-10 is not good. Fitting the data using AG theory requires one more electron population to decrease the DOS at the gap.

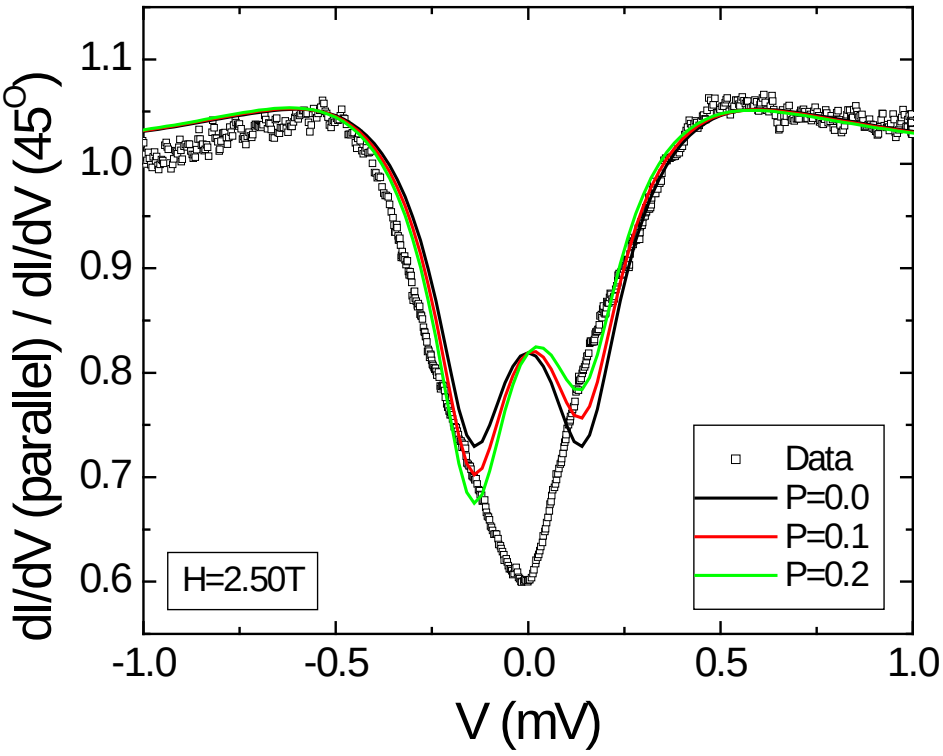

FIG. IV-10. Normalized conductance at external magnetic field (H = 2.5 T) with three different spin polarized AG densities of states versus biased voltage.

F.5. NON PURE ZEEMAN SYSTEM (NPZS)

If all the tunneling electrons are affected by the external magnetic fields and are divided into two populations, let us define the system as a pure Zeeman system (PZS). Since a fit with the PZS did not represent the data well, we hypothesized that the system

is a non pure Zeeman system (NPZS). An NPZS has an extra population of electrons that is not affected by the external magnetic field. Thus a NPZS includes three kinds of populations: electrons that are spin up, spin down and electrons that are not affected by the Zeeman Effect. The cause for the last population may be that over the whole scattering path in an NPZS, an external magnetic field prevents a net split. We heuristically added the AG DOS that was unaffected by the magnetic field to the Zeeman split AG DOS. The ad-hoc model allows for a better fit of experimental data simultaneously at the gap edge and the gap.

Assuming the NPZS and using the three AG DOS functions improves the fit for normalized tunneling conductance both at the gap edge (E=0) and at the gap ($|E|=\Delta$). To achieve a better fit, we introduced a new parameter x that is the fraction of electrons affected by the Zeeman shift in NPZS. Eq. (IV-9) gives the net AG DOS in NPZS with the three-population model. Where, $N_1(u)$ is from Eq. (IV-7) and $N(u)$ from Eq. (III-5).

$$N_2(u) = xN_1(u) + (1-x)N(u) \qquad \text{(IV-8)}$$

Eq. (IV-8) yields the density of states as shown in Fig. IV-11. Figure IV-11 shows three populations and the net AG DOS in NPZS. Half of the electrons undergo a Zeeman split in this example.

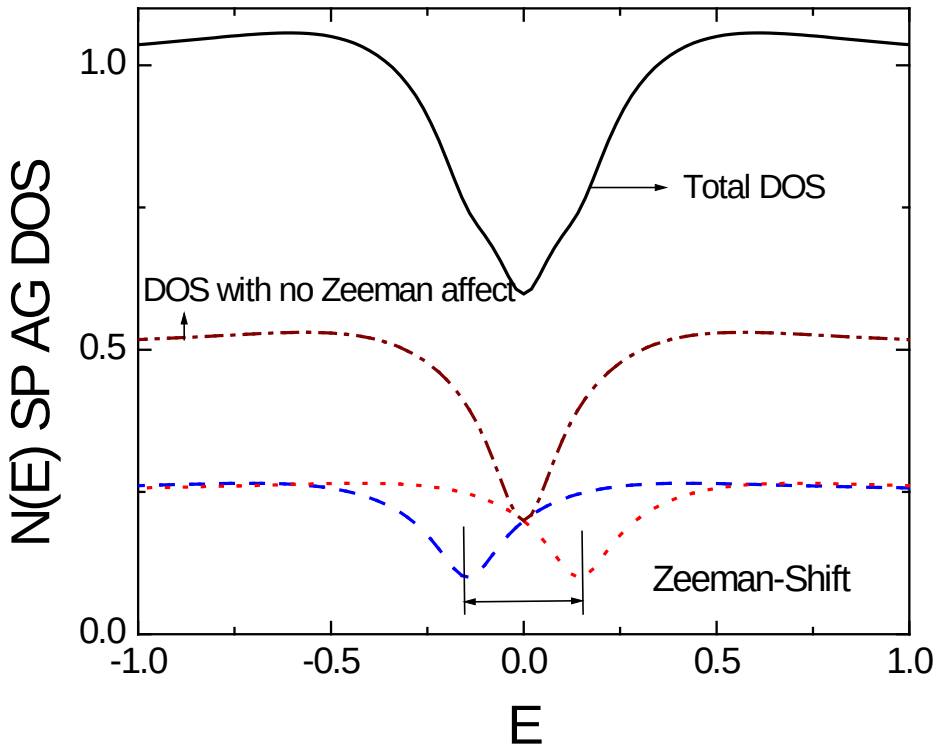

FIG. IV-11. Total AG DOS with three different types of populations (non pure Zeeman system) with $x = 0.5$ versus normalized energy.

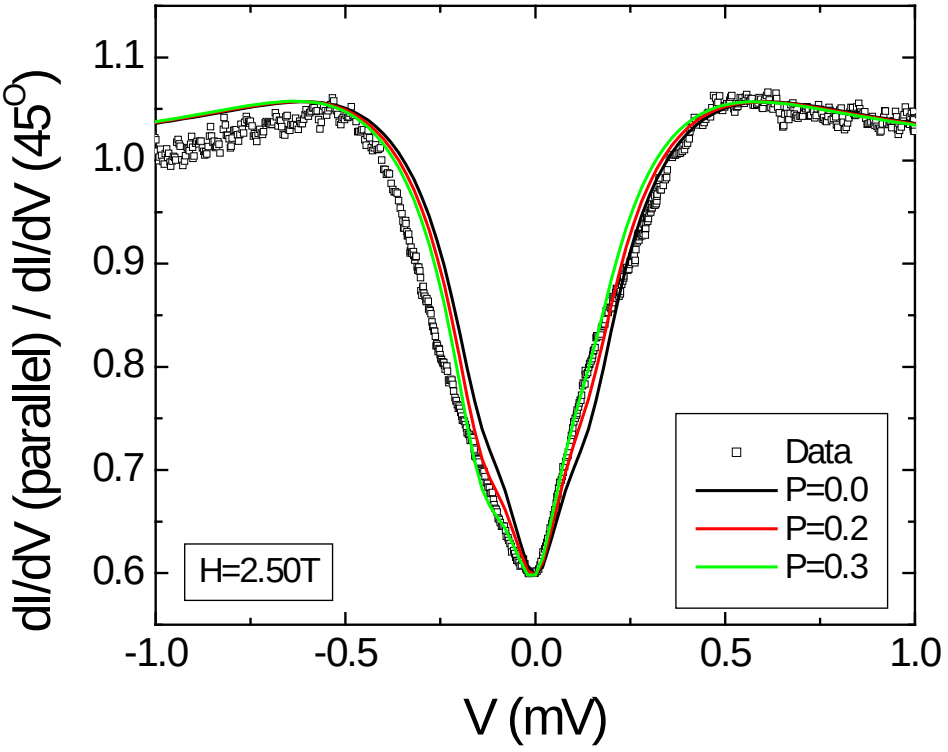

FIG. IV-12. Normalized conductance at external magnetic field (H = 2.5T) with three different spin polarized AG (non pure Zeeman system) densities of states versus biased voltage.

Fig. IV-12 shows three fits with different polarization. Clearly the NPZS AG DOS is a better approach than the PZS AG DOS, resulting in reasonable improvement in the fit using AG theory over BCS theory.

Further improvement was obtained by using different values of Δ as shown in Fig. IV-13. The increase in Δ increases the gap width. Vertical lines on the Fig. IV-13

show the highest point of the AG DOS (three-population). The values of Δ and α are selected to satisfy values at E=0 and $|E|=\Delta$ simultaneously.

.

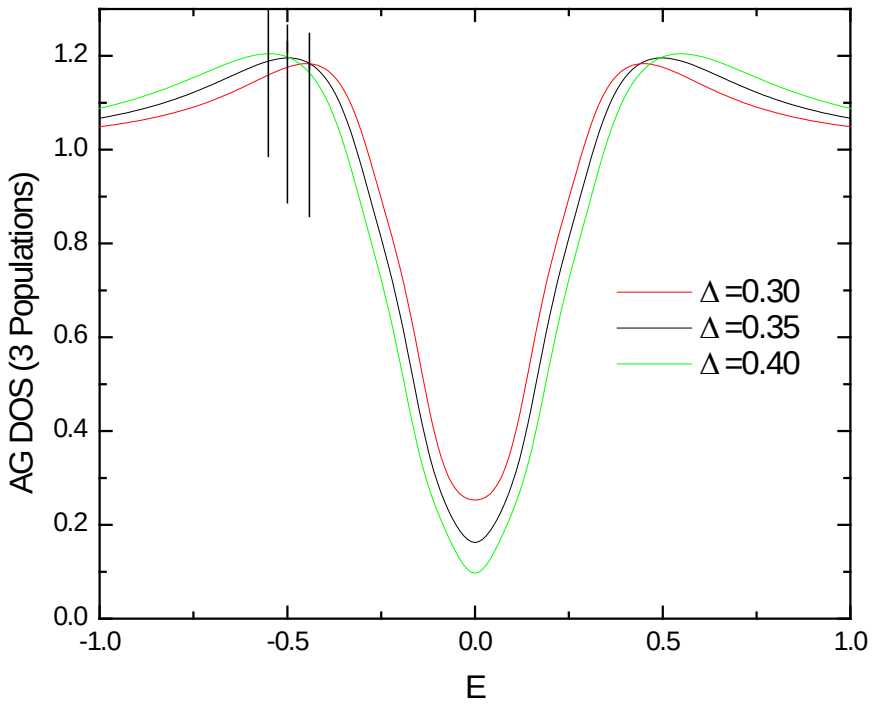

FIG. IV-13. AG density of states in non pure Zeeman system with constant α = 0.3, x = 0.5 and P = 0.0 and varying gap energy (Δ = 0.30, 0.35 and 0.40).

To compare the result with the BCS theory, we made two sets of graphs for each magnetic field, as shown in Fig. IV-14(*A*,*B*,*C*) and Fig. IV-15(*A*,*B*,*C*). The first set shows different values of Δ for both AG (NPZS) and BCS theories; the second set of graphs has the same Δ for both theories.

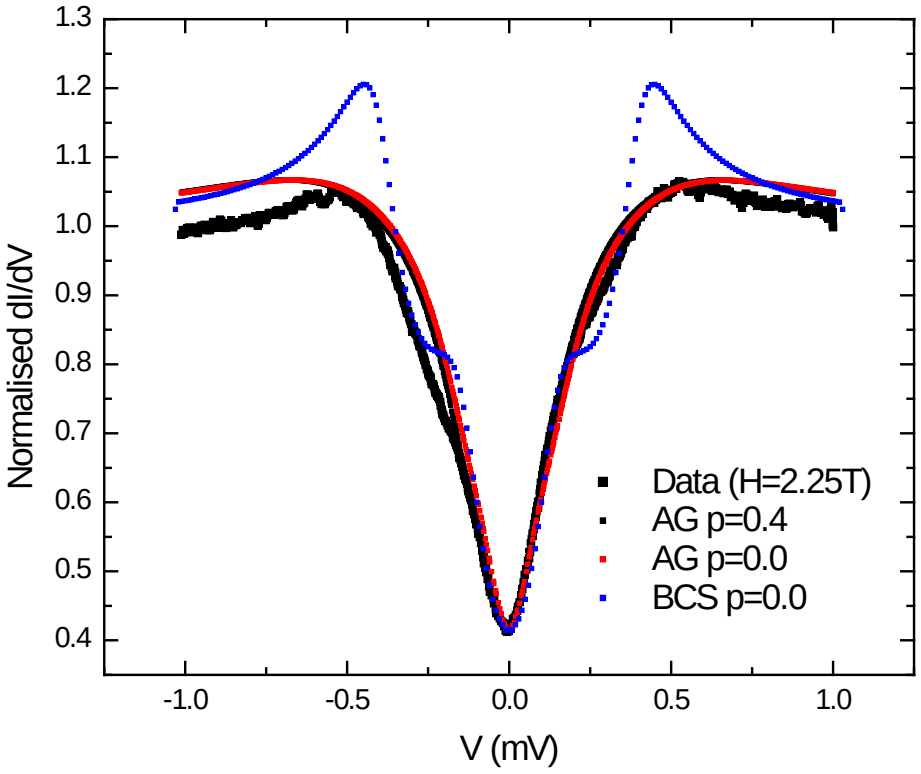

FIG. IV-14*A*. Normalized experimental conductance collected at external magnetic field (H = 2.25 T) plotted with SP BCS density of states with P = 0.0 and SP AG densities of states with P = 0.0, 0.4 (NPZS).

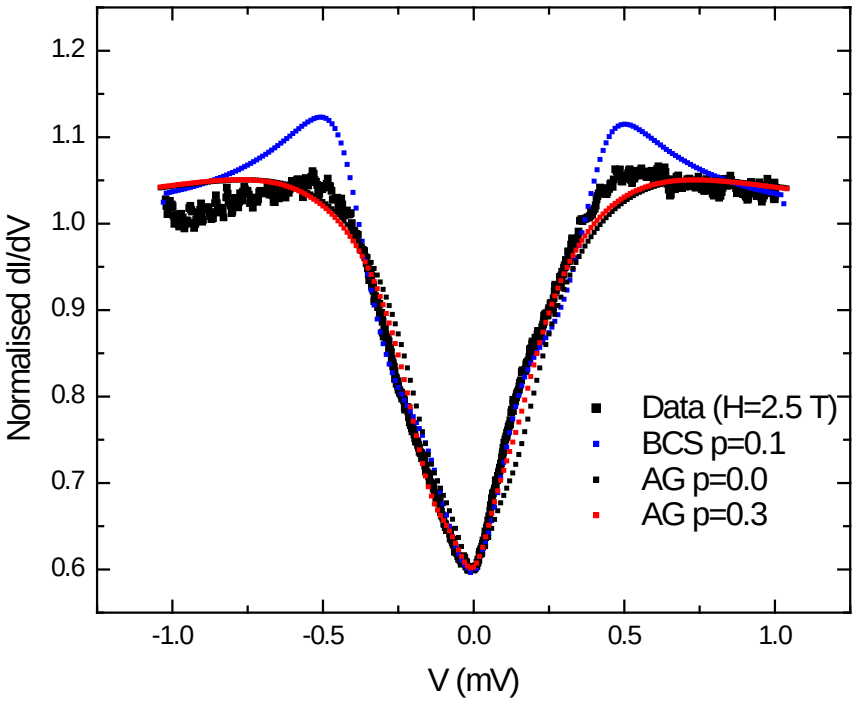

FIG. IV-14*B*. Normalized experimental conductance collected at external magnetic field (H = 2.5 T) plotted with SP BCS density of states with P = 0.1 and SP AG densities of states with P=0.0, 0.3 (NPZS).

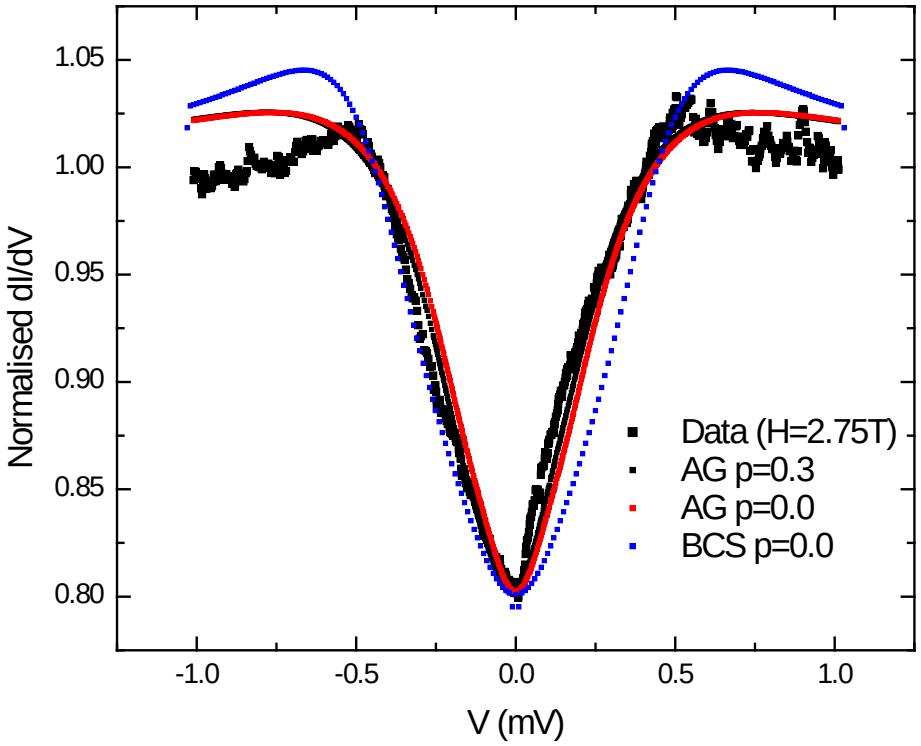

FIG. IV-14*C*. Normalized experimental conductance collected at external magnetic field (H = 2.75 T) plotted with SP BCS density of states with P = 0.0 and SP AG densities of states with P = 0.0, 0.3 (NPZS).

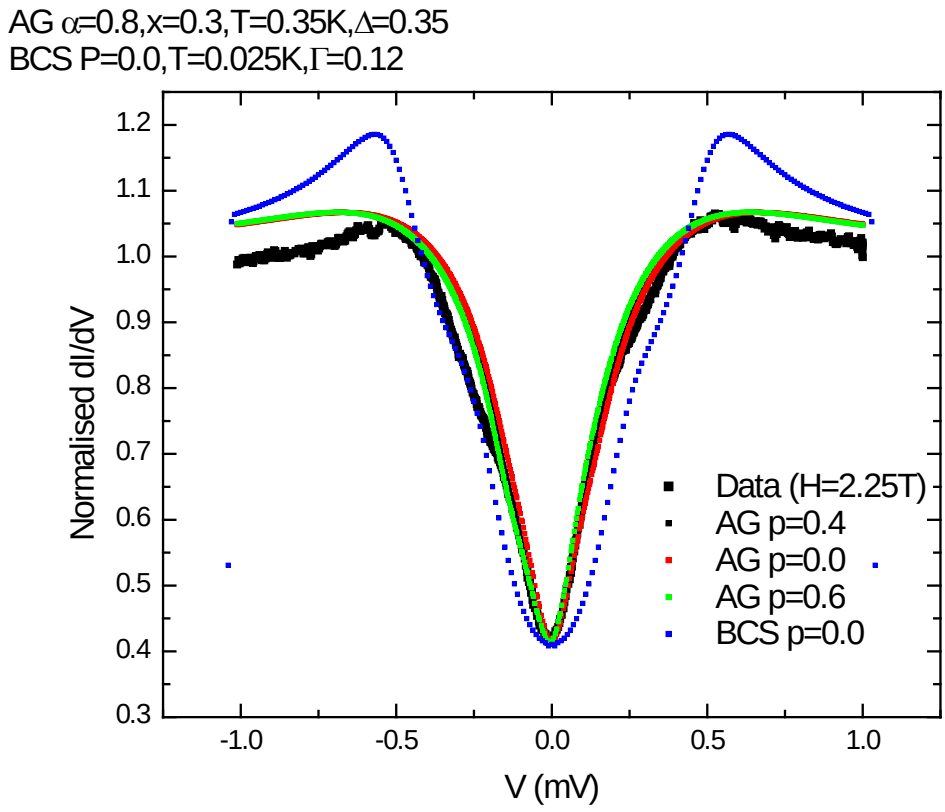

FIG. IV-15*A*. Normalized experimental conductance collected at external magnetic field (H = 2.25 T) plotted with SP BCS density of states with P = 0.0 and SP AG densities of states with P = 0.0, 0.4, and 0.6 (NPZS) with same Δ=0.35.

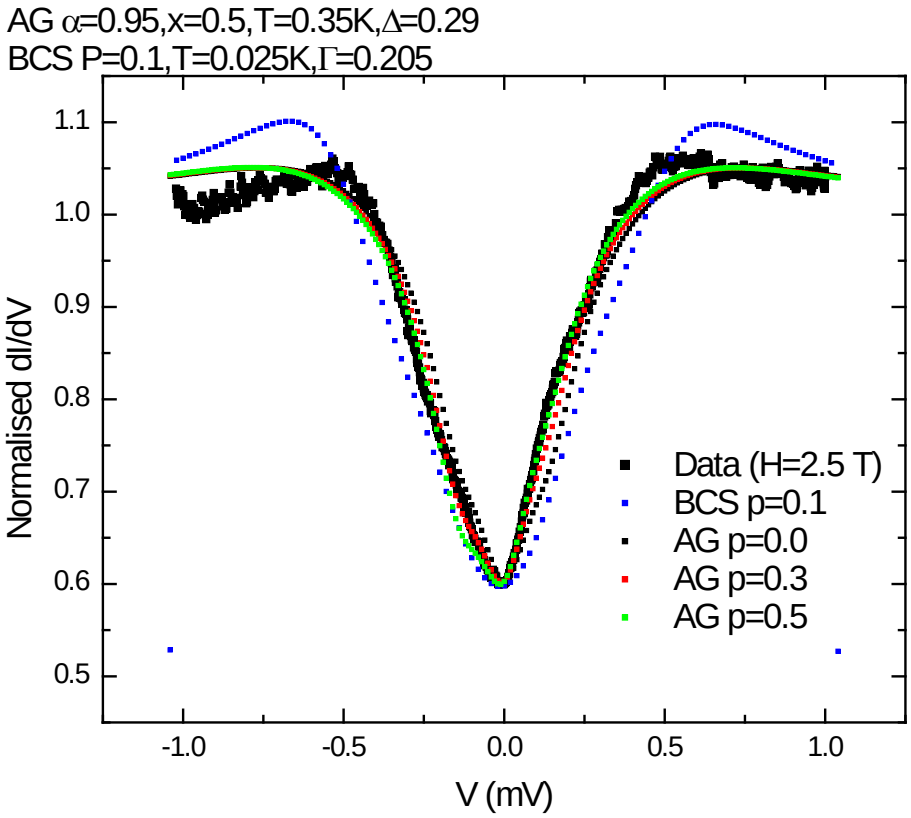

FIG. IV-15*B*. Normalized experimental conductance collected at external magnetic field (H = 2.5 T) plotted with SP BCS density of states with P = 0.1 and SP AG densities of states with P = 0.0, 0.3, and 0.5 (NPZS) with same Δ = 0.29.

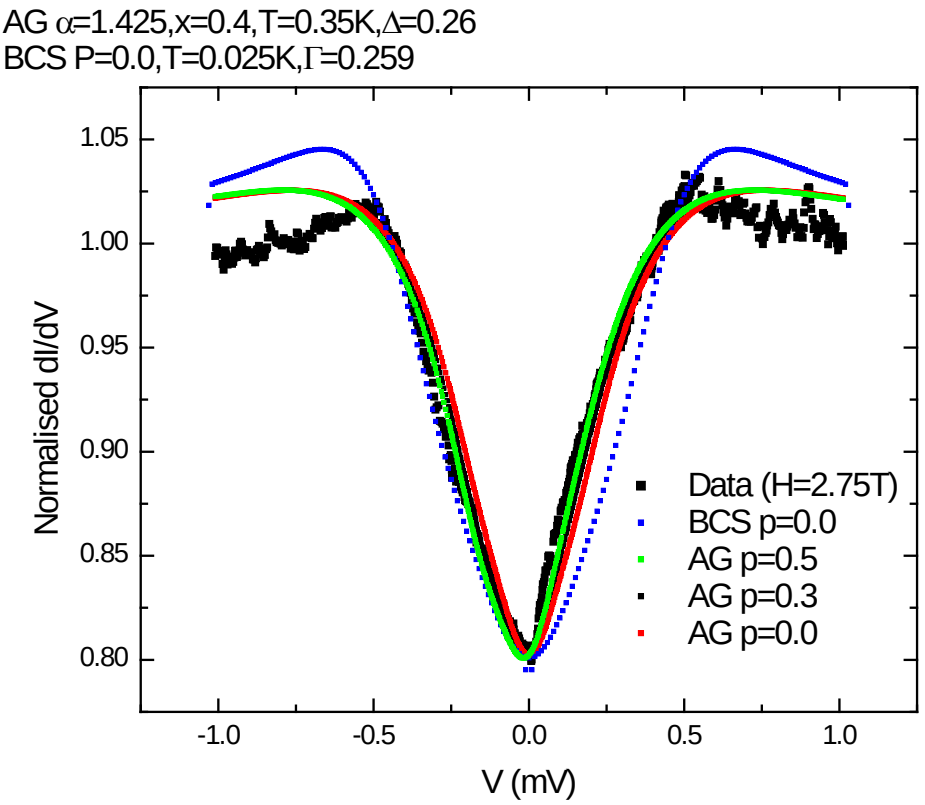

FIG. IV-15*C*. Normalized experimental conductance collected at external magnetic field (H = 2.75 T) plotted with SP BCS density of states with P = 0.0 and SP AG densities of states with P = 0.0, 0.3, and 0.5 (NPZS) with same Δ = 0.26

In both sets of graphs, the AG (NPZS) theory shows a better agreement with the experimental data than the BCS theory. Different Δ values for the same sample improve the fit. The external magnetic field could change the energy gap, although that is not clear theoretically; however the values used for the energy gap decrease with an increase in the magnetic field. The values of all the parameters for the best fit are given in the results and conclusions section.

G. RESULTS AND CONCLUSIONS

An analytical solution of the AG theory applied to the observed experimental data successfully extracted the values of polarization at different magnetic fields. The NPZS method showed an improved fit of the tunneling conductance vs voltage curve. Table IV-1 gives the extracted polarization of the experimental data at different magnetic fields. We also tried error analysis to improve the fit, as mentioned in Appendix D.

TABLE IV-1. Values of best fit parameters using BCS and AG (NPZS) theory fits with different values of Δ in AG with respect to BCS for different magnetic fields.

Parameters for AG theory

H	***α***	***x***	***P***	***T***	***Δ***
2.25	0.8	0.3	0.4	0.35	0.35
2.50	0.86	0.5	0.3	0.35	0.29
2.75	1.425	0.4	0.3	0.35	0.26

Parameters for BCS theory

H	***P***	***T***	***Δ***	***Γ***
2.25	0.2	0.025	0.26	0.074
2.50	0.1	0.025	0.26	0.130
2.75	0.0	0.025	0.26	0.259

TABLE IV-2. Values of best fit parameters using BCS and AG (NPZS) theory fits with same values of Δ in AG with respect to BCS for different magnetic fields.

Parameters for AG theory

H	***α***	***x***	***P***	***T***	***Δ***
2.25	0.8	0.3	0.4	0.35	0.35
2.50	0.86	0.5	0.3	0.35	0.29
2.75	1.425	0.4	0.3	0.35	0.26

Parameters for BCS theory

H	***P***	***T***	***Δ***	***Γ***
2.25	0.0	0.025	0.35	0.12
2.50	0.1	0.025	0.29	0.16
2.75	0.0	0.025	0.26	0.259

Using the values of Table IV-2, we plotted Fig. IV-16 and Fig. IV-17 As the external magnetic field is increased, the required α to fit the graph also increases. The system transforms from a superconductor with a gap to a gapless superconductor. The horizontal line in Fig. IV-16 shows the boundary between gapless superconductivity and superconductivity with a gap, also showing that the increase in the magnetic field reduces the Δ (gap energy) of the best fit. Thus, the gap energy is reduced by an external magnetic field, and the system ultimately becomes a gapless superconductor.[95] The gap energy from the best fit for an external magnetic field of 2.75 T matches with the bulk

gap energy (0.26 meV) of Al. The positive values of P indicate that more spins are aligned to the direction of the external magnetic field.

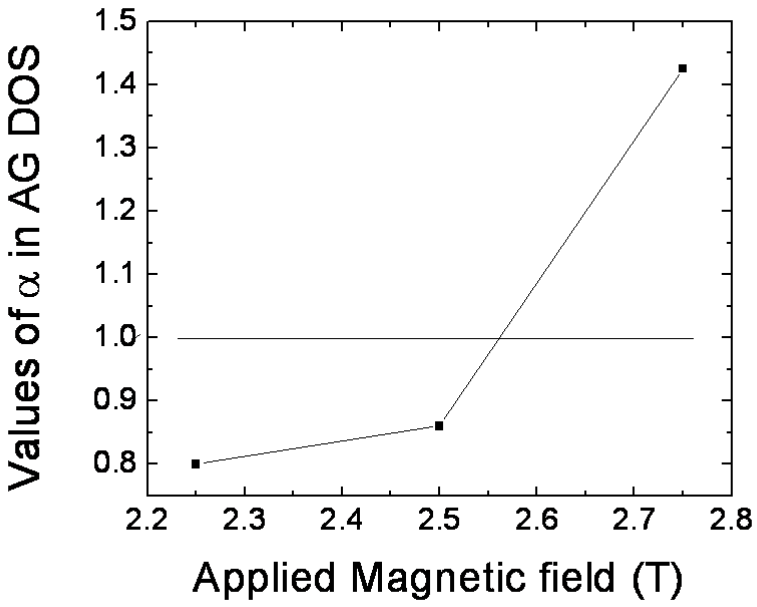

FIG. IV-16. The best fit α value plotted against different external magnetic field for AG density of states (NPZS).

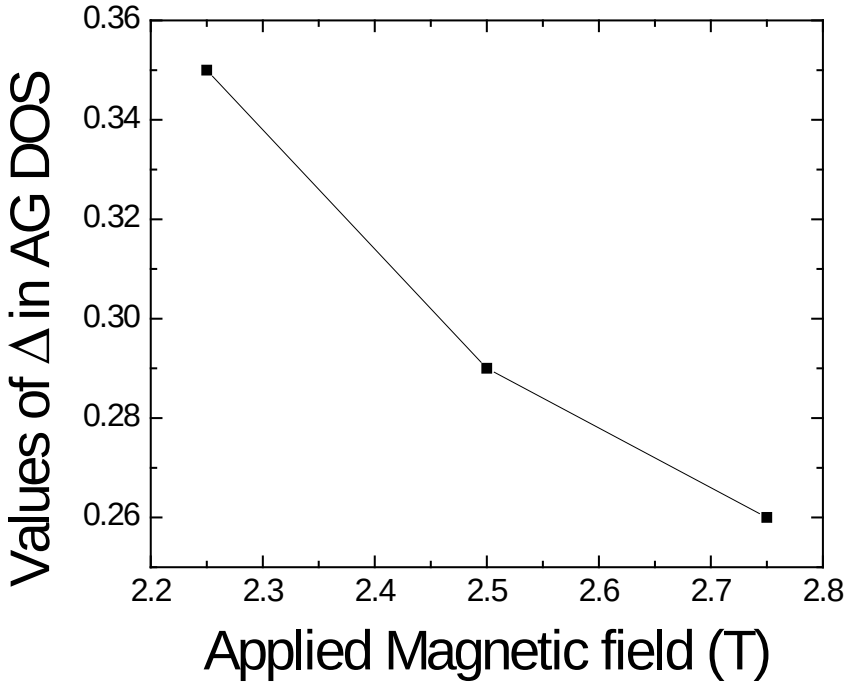

FIG. IV-17. The best fit Δ value plotted against different external magnetic field for AG density of states (NPZS).

Using the values given in Table IV-2, we plotted Fig. IV-18 containing data with all the magnetic fields and the best AG (NPZS) DOS with different Δ.

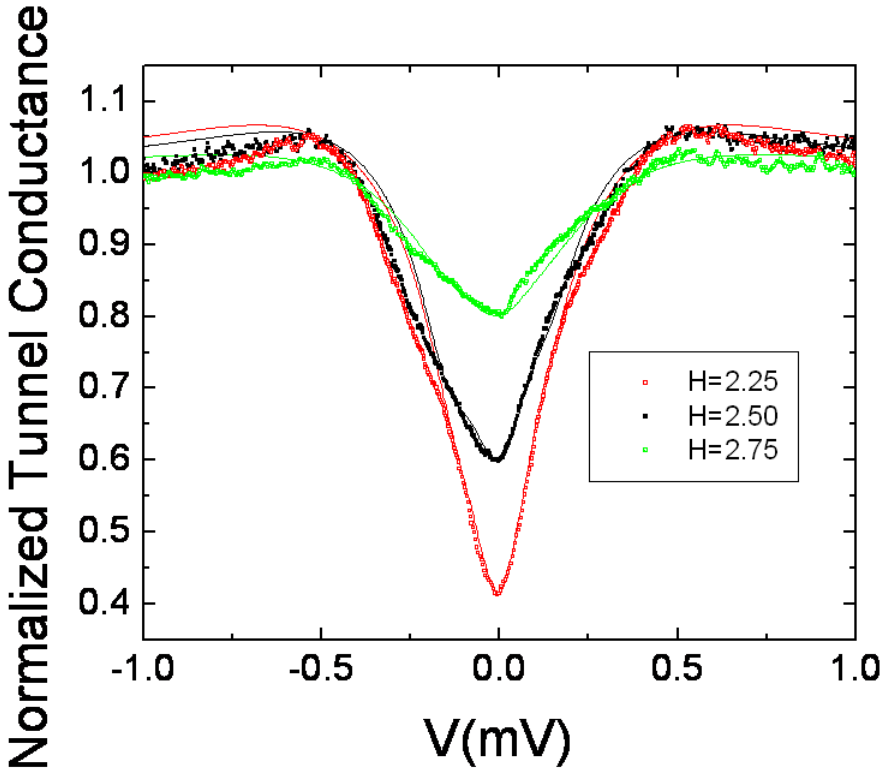

FIG. IV-18. Experimental normalized tunnel conductance with AG densities of states (NPZS) with polarization and in different magnetic fields.

Although the results are ambiguous about any dependence of polarization in the system to the applied external magnetic field, they unambiguously establish the existence of a surprisingly large polarization (~ 0.3). The AG theory shows a better fit than the BCS theory with experimental data especially at the gap edge. The results are better with NPZS (three types of carrier populations) than PZS (two types of carrier populations). The intrinsic[96] or the atomic scale[97] inhomogeneities can be responsible for smooth data points. The fits indicate the existence of spin polarization in the

tunneling experiments in magnetic field that are yet to be explored near the quantum critical regime (QCR).

The SP BCS DOS fits the experimental data at the gap but does not fit at the gap edge. If attempts were made to fit at the gap edge the gap does not fit. The SP AG DOS with PZS achieved the fit at the gap edge, but lost it at the gap. The fit was substantially improved by using a SP AG DOS with NPZS and then both the gap and the gap edge were fit well simultaneously.

The superconducting gap can be reduced by a number of factors, including for example, magnetic impurities, which can reduce the superconducting transition temperature as well as reduce the gap energy. There can be a concentration of impurities where the transition temperature is not zero but the gap is zero, a phenomenon known as gapless superconductivity. For a given magnetic field, aluminum becomes a gapless superconductor as shown in Fig. IV-16.

CHAPTER V

EXPERIMENTAL APPARATUS

A. VAPOR DEPOSITION SYSTEM

The vapor deposition system has two important parts: an ultra high vacuum (UHV) deposition chamber and a cryostat to do in-situ measurements of quenched films as shown in Fig. V-1. The UHV chamber has two 10KW Airco Temescal electron (e-) guns powered by a Sloan Pak 12 to evaporate two materials separately and simultaneously at different rates. To measure the evaporation rates, there are two electron impact emission spectroscopy instruments (EIES, see appendix E) arranged to independently measure the evaporation rates for each material. An Inficon Sentinel 200 Quartz Crystal Microbalance (QCM) measures the combined thickness of the two materials. The QCM is water cooled to maintain the operating temperature during e-gun operation.

The vacuum chamber was custom made made by Vacuum Generators now known as VG Scienta. The chamber uses an 18" diameter Edwards diffusion pump with a liquid nitrogen (LN_2) cooled trap (model # E09) filled with Santovac 5 oil. The whole system is made of stainless steel with glass viewports that allow visual observation of the deposition sources. All seals are made with copper gaskets with the exception of three Viton O rings, one sealing the top of the vacuum chamber, one on the gate valve

and one on the chamber isolation valve. Further details of the instrument are provided by Nicoli.[98]

B. CRYOSTAT

The cryostat has two main parts, the superconducting magnet and the sample space. In the sample space, the substrate is kept at low temperature. The cryostat (Fig. V-1) is separated from the UHV chamber by a gate valve. The rapid-quench condensation of co-evaporated material into thin films occurs in the deposition system. The in-situ measurement of resistance vs. temperature is done in the cryostat. The cryostat assembly consists of a liquid helium (LHe) magnet Dewar (Janis) which contains a superconducting magnet (American magnetic) capable of producing a homogeneous magnetic field up to 7 T. Inside the superconducting magnet lies an extendable LHe cryostat that holds a silicon substrate. On the inside and outside of the magnet dewar are two LN_2 reservoirs that are used to prevent radiation losses to the surroundings. The outer most jacket is pumped to 10^{-6} Torr to prevent any thermal loss due to convective heat flow.

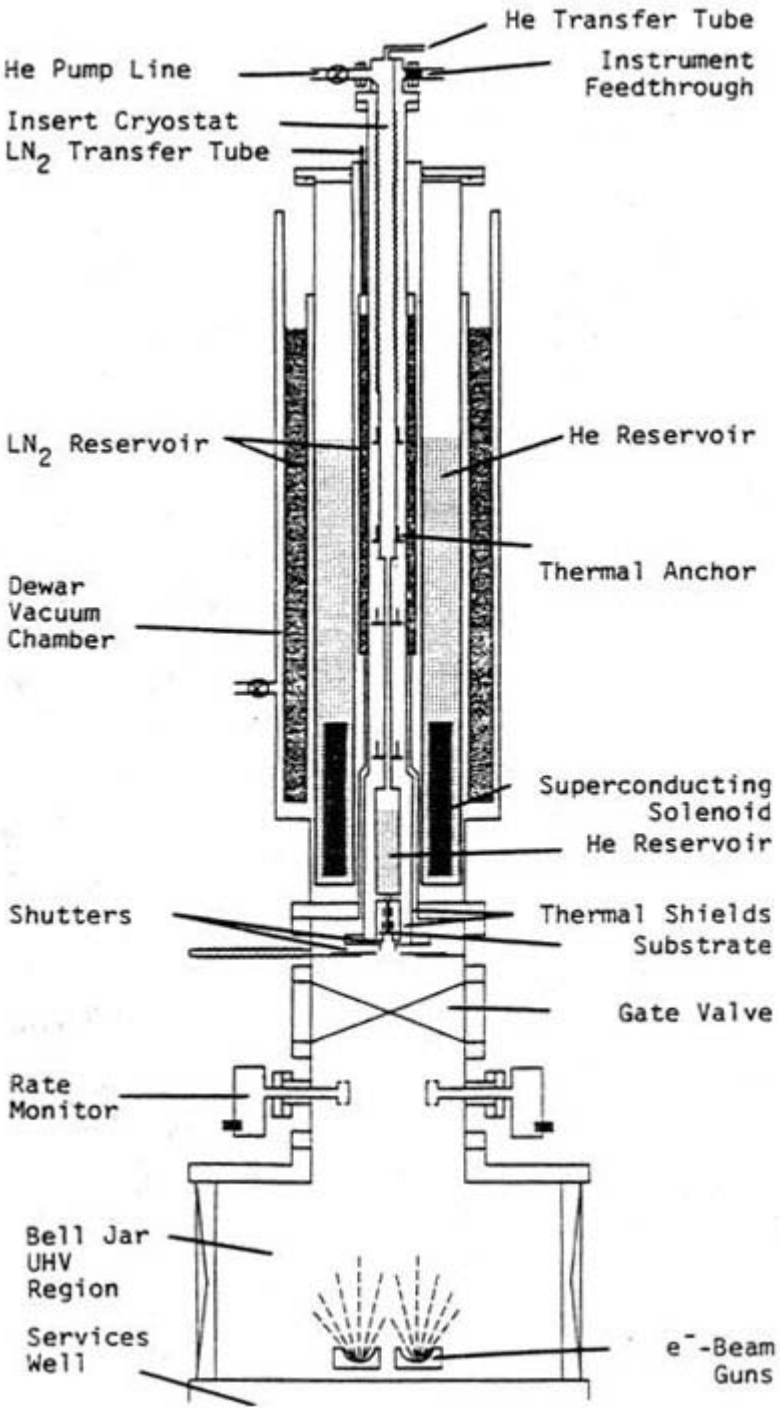

FIG. V-1. Cross-section of the UHV low-temperature evaporator (Adapted from Nikoli [98]).

C. ELECTRONICS

To measure the conductivity of co-evaporated thin films, two reversible constant current sources are used to supply current to both the sample and carbon glass thermometer. Separate Keithley 174 digital multi-meters are used to measure voltage across the sample and thermometer, and results are recorded using LABVIEW. Figure V-2 shows the circuit diagram to measure the resistance of the co-evaporated films. Figure V-3 shows the circuit diagram to measure the voltage across the carbon glass thermometer. The voltage across the thermometer is converted to degrees Kelvin using a program written in MATHEMATICA.

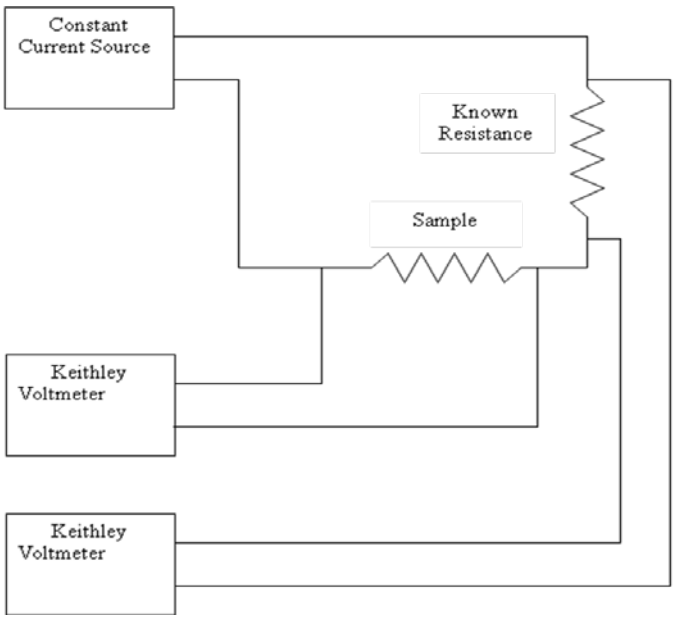

FIG. V-2. The circuit diagram to measure the current and the voltage across the co-evaporated film.

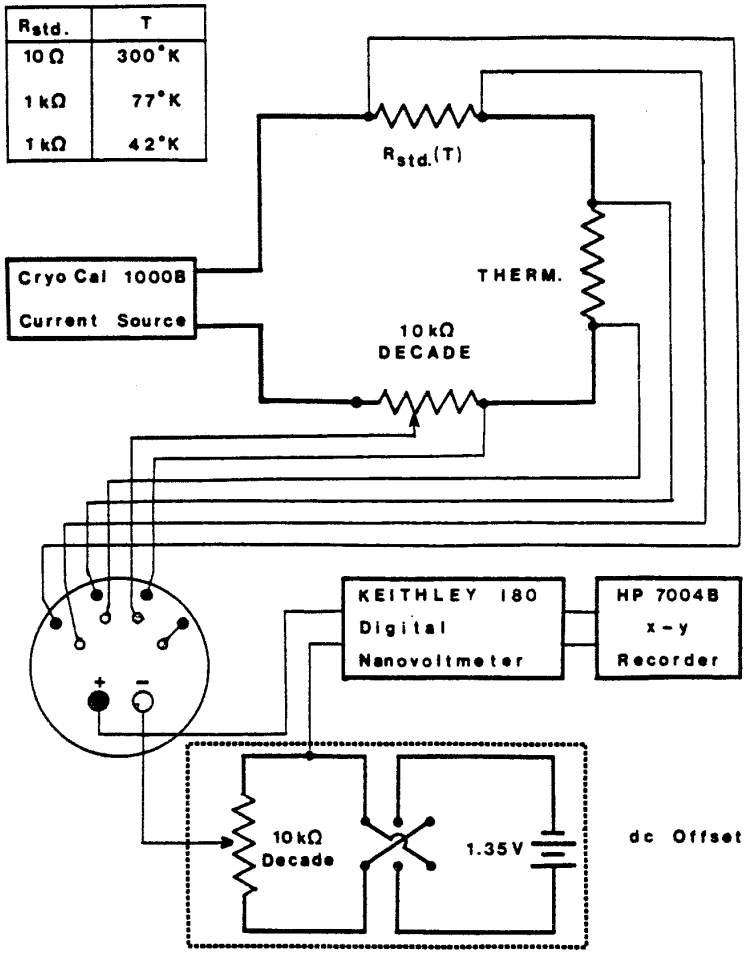

FIG. V-3. The circuit diagram to measure the voltage across the thermometer resistor.

D. SUBSTRATE PREPARATION

A 1.5 cm square substrate is cut from a factory supplied Si/SiO_2 wafer. The square is then cleaned using acetone and iso-propanol and dried using nitrogen (N_2) gas. The silicon oxide (SiO_2) layer is removed using a buffer HF solution. The substrate is kept in the buffer solution for a minute as the SiO_2 layer is very thin on factory supplied wafers.

The silicon sample is then mounted with the desired mask on a sample holder and placed inside a thermal evaporation chamber. After the chamber pressure has been pumped to $\sim 6\times10^{-6}$ Torr, silver is evaporated at a rate of ~4 Å per second and a silver film of ~500 Å gets deposited on the substrate. The silver pattern is used as contact pads for the transport measurement. FigureV-4. shows the schematic procedure to prepare a required pattern for four point transport measurements.

After the process outlined in Fig. V-4 is completed, the substrate is inserted in a UHV low-temperature evaporator for the co-deposition of Gd and Si.

a) Si/SiO_2 wafer cut in a 1.5cm square shape.

b) Buffer HF solution used to remove SiO_2 layer from the top.

c) Silver contacts made using thermal evaporator.

d) Thin film of Gd_xSi_{1-x} evaporated using e-beam in UHV system on cold substrate.

FIG. V-4. Schematic diagram to show the procedure for sample preparation.

E. BAKE AND COOL PROCESS

After a typical substrate is prepared by the process mentioned above, the inner cryostat is removed from the top of the whole cryostat and mounted on a homemade wooden frame. Two copper clamps are then attached to avoid flexible movement of the extendable bellows. The inner cryostat is then turned upside down to allow access to the bottom of the sample space. A silicon substrate with silver contacts is then mounted in the sample space. All wire contacts are checked before the inner cryostat is returned to the Dewar with magnet. The inner cryostat is sealed to the outer cryostat with a 3 and 3/8" oxygen-free high-conductivity (OFHC) copper gasket. The connections are checked again before the whole cryostat is placed on the UHV vacuum chamber with the help of an electrically operated pulley. The whole cryostat is sealed to the UHV chamber with a 10" OFHC copper gasket.

The outer jacket and the cryostat are connected to two independent diffusion pumps. During the preparation process three diffusion pumps are connected to the system. The outer jacket and cryostat are pumped overnight through nitrogen traps. Once the outer jacket is pumped to a pressure of $\sim 5\times10^{-5}$ Torr and the cryostat is pumped to $\sim 2\times10^{-6}$ Torr, the valves to the traps are closed. The gate valve is then opened to the UHV diffusion pump and the system is baked after a base pressure of 10^{-8} Torr has been achieved. The baking process continues for 20 hrs at 110°C and then for 16 hrs at 120°C. The uniformity of the temperature distribution, which defines the effectiveness of the baking process, is more important than the magnitude of the temperature. During the

baking process, the Dewar with magnet is filled with LN_2 to avoid any damage from overheating.

Just after the bake, the LN_2 trap is filled with cooled N_2 gas and then finally with LN_2 to stop any backflow of contamination. After a couple of hours, the outer jacket, magnet space and inner jacket are filled with LN_2 for thermal insulation. Once the sample space reaches ~77 K temperature, LHe is transferred to the helium reservoir above the sample space.

F. CO-EVAPORATION OF SILICON AND GADOLINIUM

Before the sample can be lowered and exposed to the e-guns for evaporation, the EIES and the QCM are calibrated by the method discussed in Chapter VI. For each evaporation step, the sample is lowered 5" from the center of the magnet and exposed to the e-guns. The shutter is opened for approximately 20 sec for each evaporation step. The sample is then pulled up to the center of the magnet. If the magnet is not used, the sample is pulled only halfway, until both the N_2 and He thermal shutters are closed as shown in Fig. V-5. During the process of evaporation, the sample space temperature can rise to as high as 30^{o}K. Even if the evaporation shutter is not open but the thermal shutter is open, the sample space will be heated.

A desired rate is set and then the sample space is moved down. During the descent of the sample, the desired evaporation rate tends to drift. It is not clear whether fixing an evaporation rate before bringing the sample down or bringing down the sample

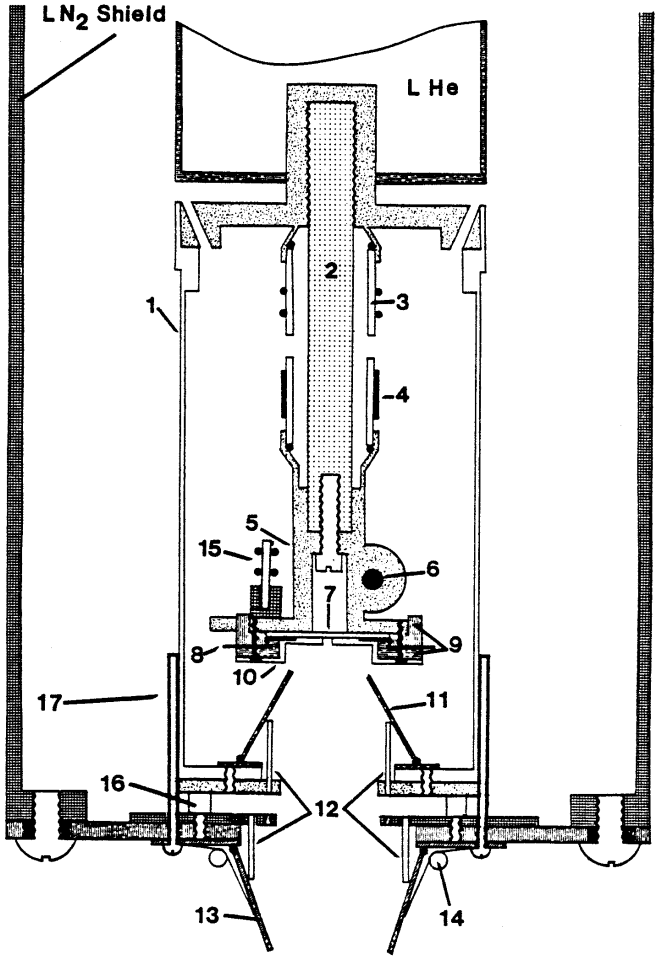

1. L He Radiation shield	10. Mask
2. Thermal transfer rod	11. LHe Radiation shield shutters
3. Sapphire heat sink (1/2" dia)	12. Shutter push pins
4. RuO2 Substrate heater	13. LN2 radiation shield shutters
5. Substrate holder	14. Tungsten spring
6. Carbon glass thermometer	15. Square sapphire heat sinks
7. Silicon substrate	16. Teflon thermal insulator
8. Platinum foil leads	17. Shutter plate guideposts
9. Teflon substrate clamps	

FIG. V-5. A cross section of the sample space with different shutters.

and then aiming for a desired evaporation rate is better. In both cases the sample space is exposed to the e-gun radiations for a long time.

Figure V-5 shows different components in and around the sample space. The whole sample space is lowered till both the LHe and LN_2 shutters are opened. For each evaporation process, the sample is lowered, and once the evaporation is done, it is pulled back until both shutters are closed. The size of the Helium reservoir requires refilling liquid helium in the reservoir after every evaporation process. In a few of the evaporation steps, the liquid helium in the reservoir boiled off before a desired co-evaporation rate could be achieved. The disproportionate boiling off of LHe leads to irregularities in the temperature coverage for the sample measurements. The range over which sample data can be collected depends on the amount of LHe left after the evaporation. Each evaporation is started with a full He reservoir (assumed, since the reservoir has no Helium level detector).

During co-evaporation, two numbers were observed to fix the value of x (fraction of gadolinium in Gd_xSi_{1-x}). One combined evaporation rate is given by a QCM and a second gadolinium evaporation rate is given by the EIES. The EIES rate is interpreted instantaneously and subtracted from the evaporation rate of the QCM to estimate the evaporation rate of Si. Every process aims for a pre-calculated evaporation ratio. To start the evaporation, the QCM and the EIES are reset at the same time to record the total thickness at the same instant that the evaporation shutter is opened. To reduce the error of approximately a second during the reset time of each instrument, opening the shutter for more than 20 sec reduces the error to less than 5%. Better control on the evaporation

rate and the total time are possible within a minimum thickness of 4 nm at x=14%. Chapter VI discusses the calibration problems in more detail.

CHAPTER VI

CALIBRATION AND MEASUREMENT

In the process of co-evaporation, the final thickness and respective thicknesses of the two materials are requisite to estimate the atomic ratio. Thickness measurements can easily be done with two different electron impact emission spectroscopes (EIES see appendix E) for each respective material and a quartz crystal microbalance (QCM) for the total thickness. Appendix E shows the working of the EIES.[99]

This chapter explains the different calibration steps taken to extract the thickness. Measuring the individual thickness of each material is crucial as the ratio of each material during co-evaporation depends on its individual thickness. EIES cannot be used for the thickness measurement for silicon as silicon has a very poor optical signal. One QCM is used for total thickness and one EIES is used for the thickness of gadolinium only.

Calibrating and measuring the whole thickness requires five steps as given below:

A. Calibrate QCM

B. Calibrate EIES with respect to QCM

C. Calibrate silicon thickness to gadolinium thickness using QCM.

D. Conduct co-evaporation process

E. Extract individual thickness after completion of co-evaporation

F. Measure finite conductivity

A. CALIBRATE QCM

The substrate and the QCM are at different distances from the evaporating source, which leads to a difference in the thickness measured at the QCM and the actual thickness at the substrate as shown in Fig. VI-1. The QCM is calibrated by repeated evaporation of pure gadolinium and pure silicon to a known thickness and then compared to the actual thickness measured using atomic force microscopy (AFM).

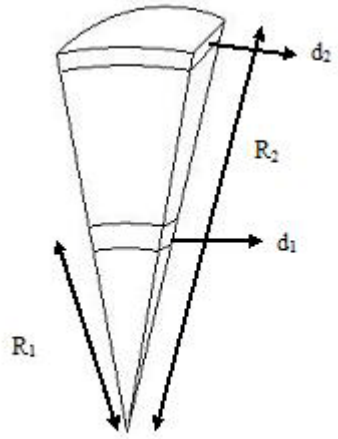

Fig. VI-1. Different thickness at different distance from the evaporating source

The calibration includes the geometric effects, or tooling factor, of the QCM. The volume of the evaporated material at the top and midpoint of the evaporation path is the same for a given solid angle and for a given time. Approximating each volume to be a cuboid, the volume at different distances from the source will be equal:

$$4\pi R_1^2 d_1 = 4\pi R_2^2 d_2 \qquad \text{(VI-1)}$$

Eq. VI-1 gives the relation of the thickness recorded at the QCM to the actual thickness evaporated. In the data, the actual thickness is reported for each sample.

The value of $\frac{d_2}{d_1}$ is observed as 0.3 from the AFM scan as shown in Fig. VI-2. The thickness ratio approximately matches the geometric ratio of $\frac{R_1}{R_2}$. In the evaporation system, R_1 is approximately 50 cm and R_2 is approximately 90 cm.

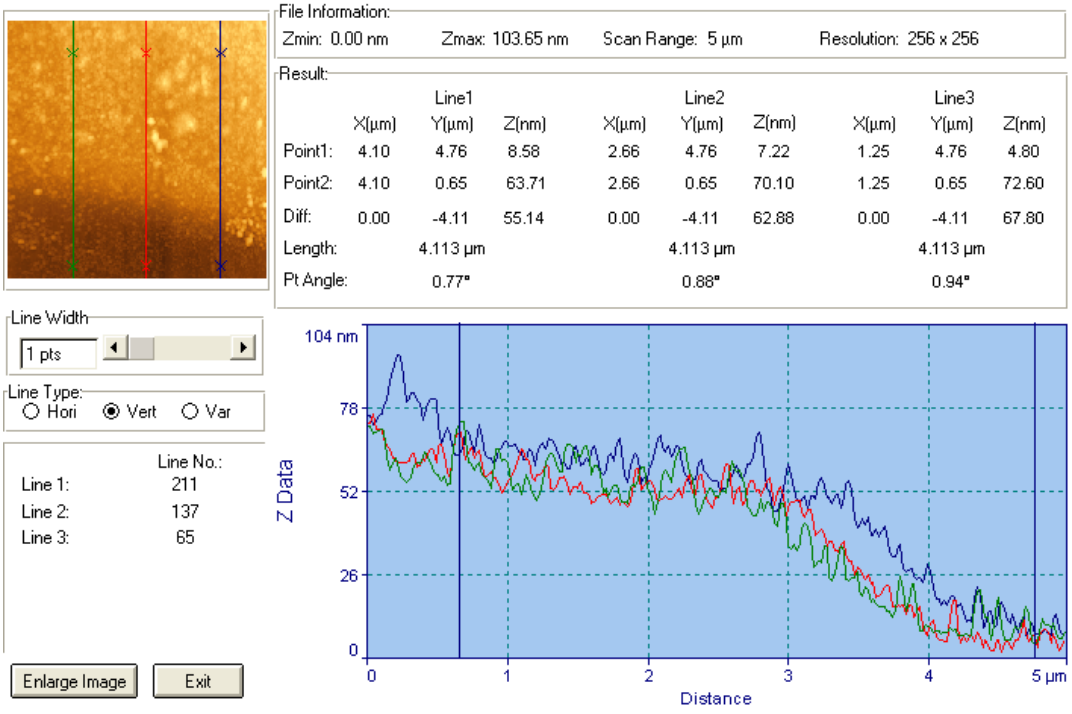

FIG. VI-2. Atomic force microscopy image and data for gadolinium film (d_1 = 200 nm).

B. CALIBRATE EIES WITH RESPECT TO QCM

First, the EIES sensor is left on for 30 min to make sure the electronics are stable and have a constant filament current. The desired frequency is set on the EIES for gadolinium, and gadolinium is evaporated. Both QCM and EIES values are recorded manually. EIES thickness is plotted against different QCM thicknesses in Fig. VI-3. The graph is fit to a straight line and the slope is used in steps C and D. After the calibration process, the EIES reading can be used to estimate the thickness of gadolinium given by QCM. Appendix E explains EIES in more detail.

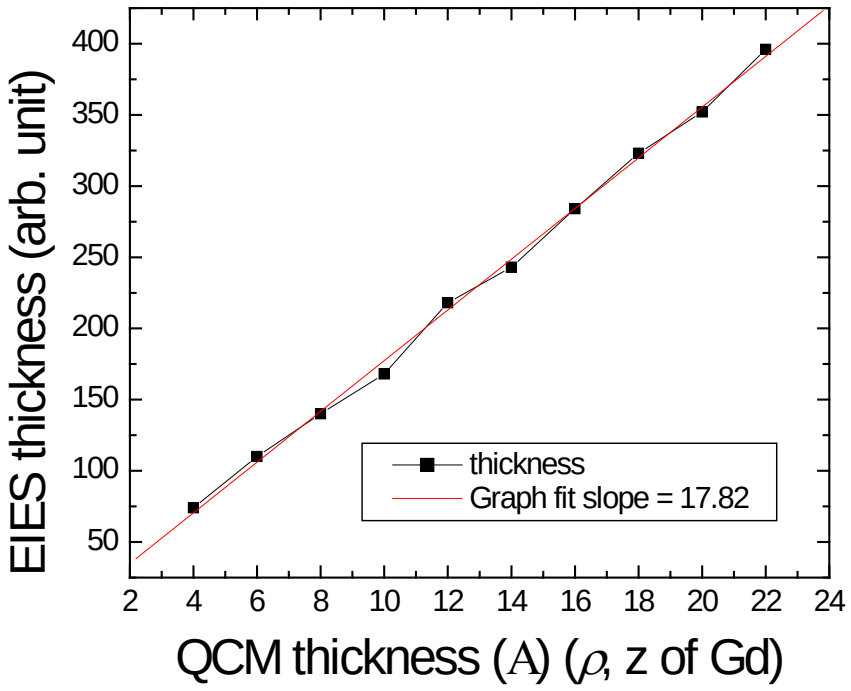

FIG. VI-3. EIES thickness plotted against QCM thickness of gadolinium.

C. CALIBRATE SILICON THICKNESS TO GADOLINIUM THICKNESS USING QCM

The QCM uses AT-cut α-quartz crystals so shear vibrations can be measured. The crystal wafer is prepared by cutting the quartz at approximately 35.17° from its Z-axis. A typical crystal plate is a cylindrical disk with a diameter of 1 cm and a thickness of about 0.1 mm to 0.7 mm for resonant operation in the 2 to15 MHz frequency range.

The film thickness is related to the change in resonant frequency of the quartz crystal. The relation is given by Eq. VI-2:

$$t = \frac{N_q \rho_q}{\pi \rho_m f_c z} \tan^{-1}\left\{ z \tan\left[\frac{\pi (f_q - f_c)}{f_q} \right] \right\} \qquad \text{(VI-2)}$$

where

t = thickness of film deposited

N_q= frequency constant for AT-cut quartz crystal ~ 1.668×10^{13} Hz/Å

ρ_q= density of quartz 2.648 gm/cm^3

ρ_m= density of film material in gm/cm^3

F_c= frequency of loaded crystal (after deposition) in Hz

F_q= frequency of unloaded crystal (prior to deposition) in Hz

z= z factor of film material = $\left(\frac{\rho_q \mu_q}{\rho_m \mu_m}\right)^{\frac{1}{2}}$

μ_q= shear modulus of quartz ~ 2.947×10^{11} gm/(cm s^2)

μ_m= shear modulus of the material deposited

The QCM instrument requires the density (ρ) and the z-ratio of a given material to estimate the evaporation rate and thickness. In the QCM calibration of silicon, the z-ratio and the density of gadolinium are used while silicon is evaporated. Once the silicon is evaporated, the z-ratio and the density were changed from gadolinium values to silicon values on the QCM and the thickness is recorded. The ratio of the QCM value with gadolinium settings to the QCM value with silicon settings is a constant for any given thickness. Figure VI-4 relates the QCM thicknesses for silicon, with the use of silicon density and z-ratio, vs. silicon, with the use of gadolinium density and z-ratio. The value of the slope from the above calibration will be used to determine the individual thicknesses and percentage of gadolinium co-evaporated with silicon.

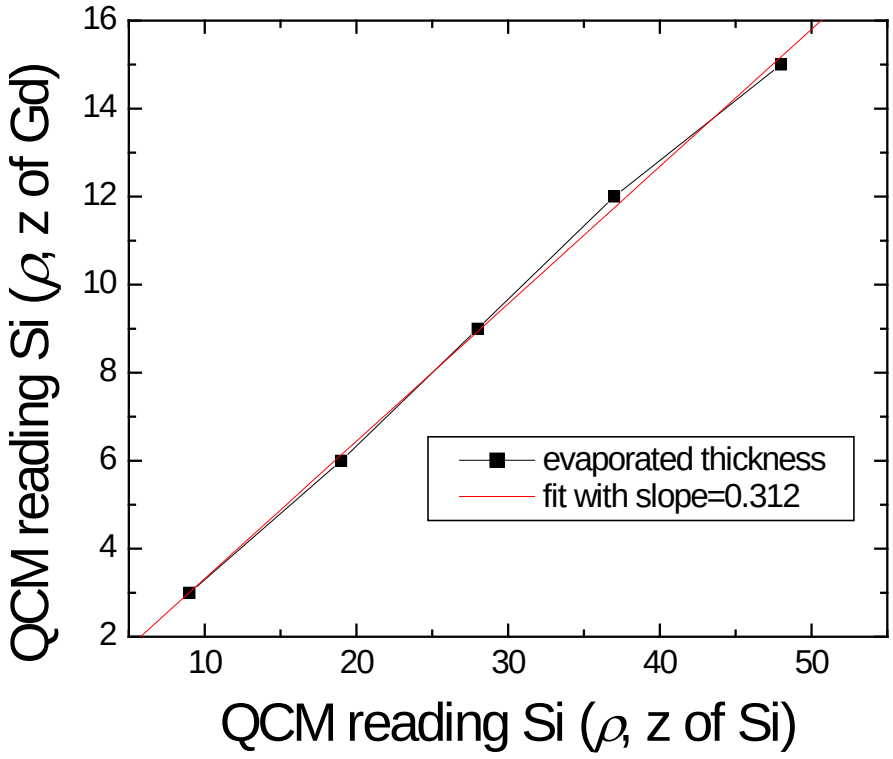

FIG. VI-4. Quartz crystal microbalance thickness measurement for silicon with use of silicon density and z-ratio and gadolinium density and z-ratio.

D. CONDUCT CO-EVAPORATION PROCESS

During co-evaporation of gadolinium and silicon, EIES is used to observe the desired evaporation rate of gadolinium, and QCM is used to observe the total thickness of gadolinium and silicon. The only way to get information about the rate at which silicon is evaporated is to subtract the calibrated evaporated rate of EIES (as done in

Step B) from the QCM evaporation rate. The relative evaporation rate is very crucial for the whole experiment as even a small change in the evaporation rate will lead to an significant change in the ratio of gadolinium and silicon. Silicon is a poor conductor of electrons when bombarded by an e-gun, so it is better to set the evaporation rate for silicon first and then adjust the evaporation rate of gadolinium. The gadolinium evaporation rate is easier to set than the silicon evaporation rate once it has been turned off and on again.

E. EXTRACT INDIVIDUAL THICKNESSES AFTER THE COMPLETION OF EVAPORATION

Once the process of evaporation is completed, two measurements are recorded: the total thickness of co-evaporation using QCM and the total thickness of gadolinium evaporated using EIES. First, the EIES value is changed to the QCM equivalent thickness using the calibration method described in Step B. The gadolinium QCM thickness is then subtracted from the total QCM value. The remaining QCM value left is the thickness of silicon in terms of gadolinium z-ratio and density. The remainder is changed to the thickness of the silicon with z-ratio and density of silicon as described in Step C.

Let us assume that the QCM gives a thickness t_q and EIES gives a thickness t_e in Angstrom at the end of the evaporation. Let the slope of the fit be m in the calibration of EIES and the slope for the different z-ratio is n.

The step-wise calculation to find the value of *x* and total thickness evaporated, where *x* is the fraction of gadolinium atoms in Gd_xSi_{1-x}, follows.

1. The equivalent thickness of EIES in QCM is $t_1 = t_e \times m$.
2. The net Si thickness evaporated with z ratio set to gadolinium is $t_q - (t_e \times m)$.
3. The net Si thickness evaporated with z ratio set to silicon is $t_2 = (t_q - (t_e \times m)) \times n$.

We assumed that a co-evaporated film is equivalent to two films with respective thickness of gadolinium and silicon as shown in Fig. VI-5.

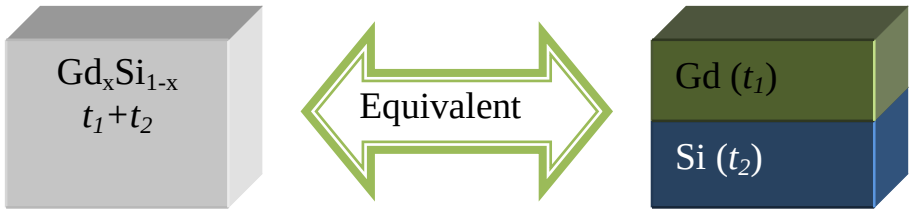

FIG. VI-5. Equivalence of two different thin films in thickness.

Both films have the same cross-sectional area but different thicknesses. The volumes of the films are V_1 and V_2 respectively for gadolinium and silicon. The density and atomic weight of gadolinium are d_1 and w_1 and of silicon are d_2 and w_2. The percentage of gadolinium atoms in total number of gadolinium and silicon atoms is defined as *x*.

4. *x* is calculated from Eq. VI-3,

$$x = \frac{d_1 \times \frac{V_1}{w_1}}{d_1 \times \frac{V_1}{w_1} + d_2 \times \frac{V_2}{w_2}} \quad , \qquad \text{(VI-3)}$$

we define

$$\frac{d_1 \times \frac{V_1}{w_1}}{d_2 \times \frac{V_2}{w_2}} = k \frac{t_1}{t_2} \quad , \qquad \text{(VI-4)}$$

where k is defined as

$$k = \frac{\frac{d_1}{w_1}}{\frac{d_2}{w_2}} \quad , \qquad \text{(VI-5)}$$

and is constant for two materials. Therefore, x is defined as

$$x = \frac{k \frac{t_1}{t_2}}{k \frac{t_1}{t_2} + 1} \quad , \qquad \text{(VI-6)}$$

This process can be used to find the total thickness as t_1+t_2 and the fraction of Gd in Gd_xSi_{1-x} as x.

F. MEASURE FINITE CONDUCTIVITY

First, we carried out co-evaporation until a conductive film was formed, confirming the continuity of the film by measuring the voltage across the film. Extreme precautions are taken to make sure that the film does not get destroyed during measurement. Once a finite conductivity is measured by a four point DC method (Fig. V-2), the sample is moved up to the center of the cryostat and the resistance is measured against temperature. Safety measures are observed as the heater is used with a constant current source to slowly increase the temperature to the desired value. Since a phase lag occurs between the application of the current and an increase in temperature, the temperature must stabilize before the sample voltage and carbon glass thermometer voltage are recorded using LABVIEW. A similar process is carried out during the cool down. The manual adjustment leads to steps in the data acquisition.

CHAPTER VII

EXPERIMENTAL RESULTS AND ANALYSIS

This chapter discusses the experimental results obtained and uncontrolled parameters involved during the experiment. Films with nominal values of x (fraction of gadolinium in Gd_xSi_{1-x}) and thicknesses were also analyzed to understand the transport properties near the metal-insulator transition (MIT). For some time,[3] the sign of the derivative of conductivity with respect to temperature, evaluated at low temperature, was considered a main indicator to determine whether the material is an insulator or a metal. Materials with $\frac{\partial \sigma}{\partial T} \leq 0$ were considered metals, while those with $\frac{\partial \sigma}{\partial T} > 0$ were considered insulators. Including quantum corrections to the conductivity showed that the conductivity derivative may be positive, $\frac{\partial \sigma}{\partial T} > 0$, for metals as well.[99] Thus, the sign of the derivative, $\frac{\partial \sigma}{\partial T}$, cannot be considered a reliable criterion to differentiate metals from insulators.[44] If conductivity of a material is extrapolated to T=0 and has some finite conductivity then it is considered as a metal. All films prepared in this work are metals by this criterion, except one.

We prepared the Gd_xSi_{1-x} thin films by the method described in the previous chapter, and took transport measurements for different thicknesses and for different values of percentage of gadolinium(x). The resistances and the conductivities of the thin films were then measured at different temperatures as shown in Figs. VII-1 and VII-2

respectively. The colors red, blue and green represents the samples evaporated in the same experimental run. Each run has either three or four successive film depositions. A careful look at the graph reveals two parameters competing against each other, *x* and thickness, to determine whether one film will be more conductive than another film. As expected, the conductivity increases as both the percentage (*x*) and thickness increase.

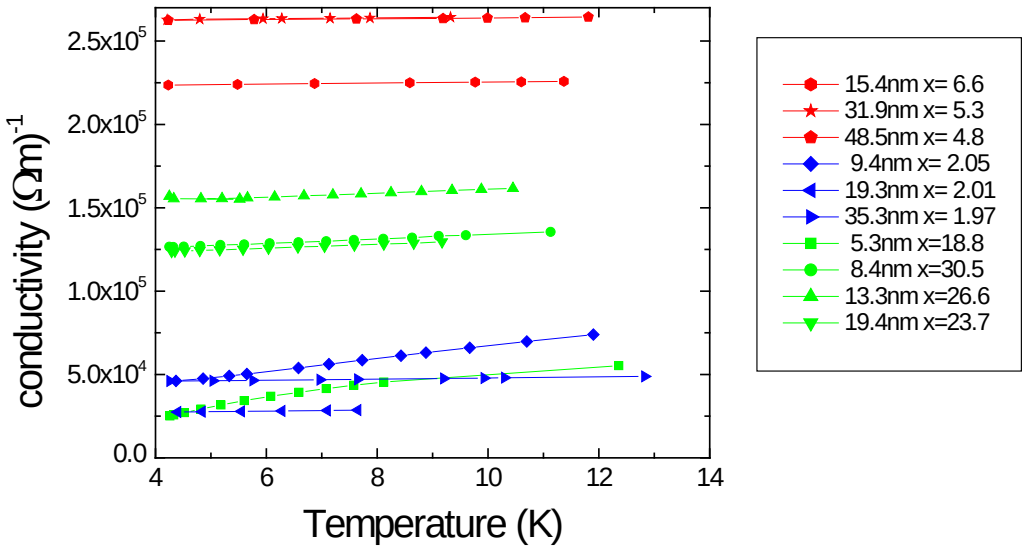

FIG. VII-1. DC conductivity vs. temperature for thin films with different thicknesses and x values.

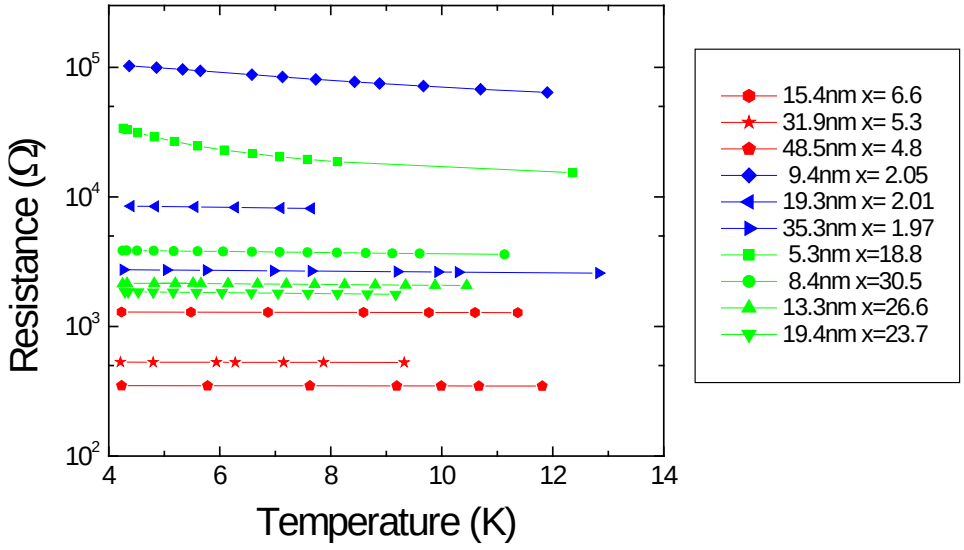

FIG. VII-2. Resistance vs. temperature for thin films with different thicknesses and x values.

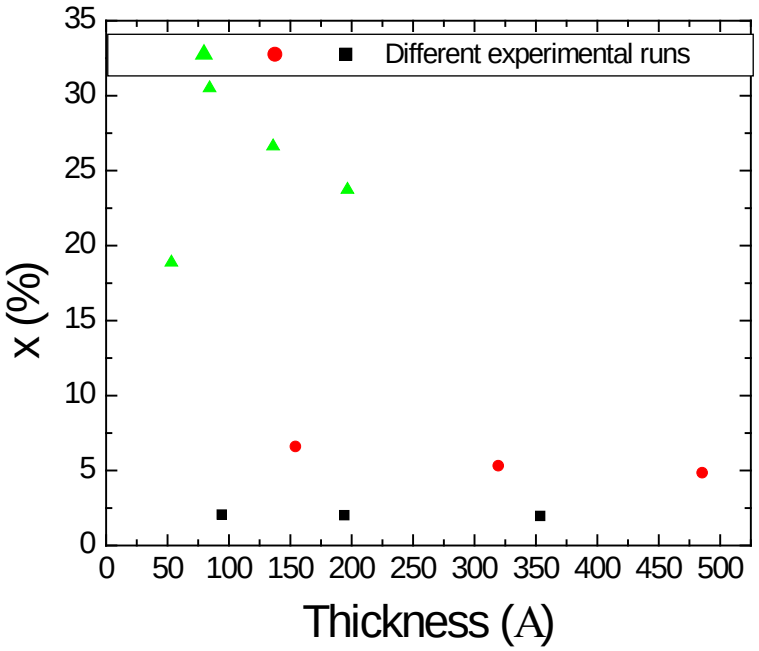

FIG. VII-3. Percentage of x vs. thickness achieved for different thin films.

In each experiment, a film was measured, then an additional film segment was added on top with the aim of having the same x (Fig. VII-3). However, every evaporated film segment had a different x. The set of computational graphs (Figs. VII-4 to VII-7) shows the fluctuation in the evaporation of pure silicon, which further led to a fluctuation in x.

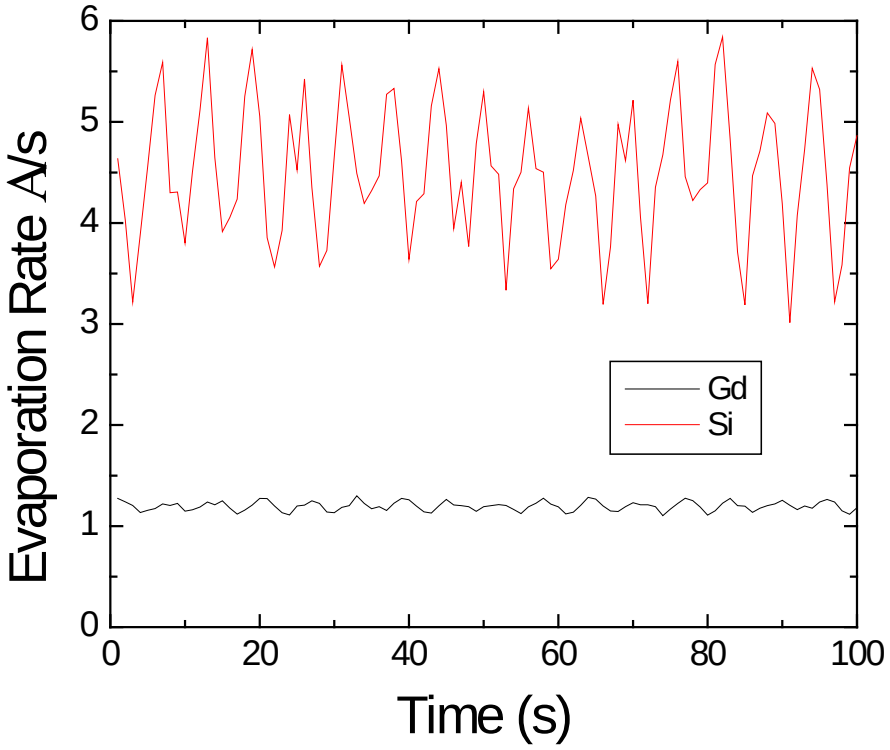

FIG. VII-4. Computer generated evaporation rate fluctuation of silicon and gadolinium.

Fig. VII-4 shows the fluctuation in the evaporation rates of pure silicon and gadolinium generated by adding random numbers to a desired rate. The magnitudes of the random numbers were set by the observed fluctuation during the evaporation process. As Fig. VII-4 shows, the evaporation of gadolinium is stable and has a negligible fluctuation (0.1 Å) within the instrument minimum range, while during the evaporation of silicon, the evaporation rate changed up to 30% within seconds. There was also an overall drift in the rate which was observed over a long time, which although included in the graph is not very prominent. Figure VII-4 shows the actual rate required

to achieve a desired x=14% as discussed Chapter VI. Silicon has to be evaporated at a rate approximately four times larger than gadolinium.

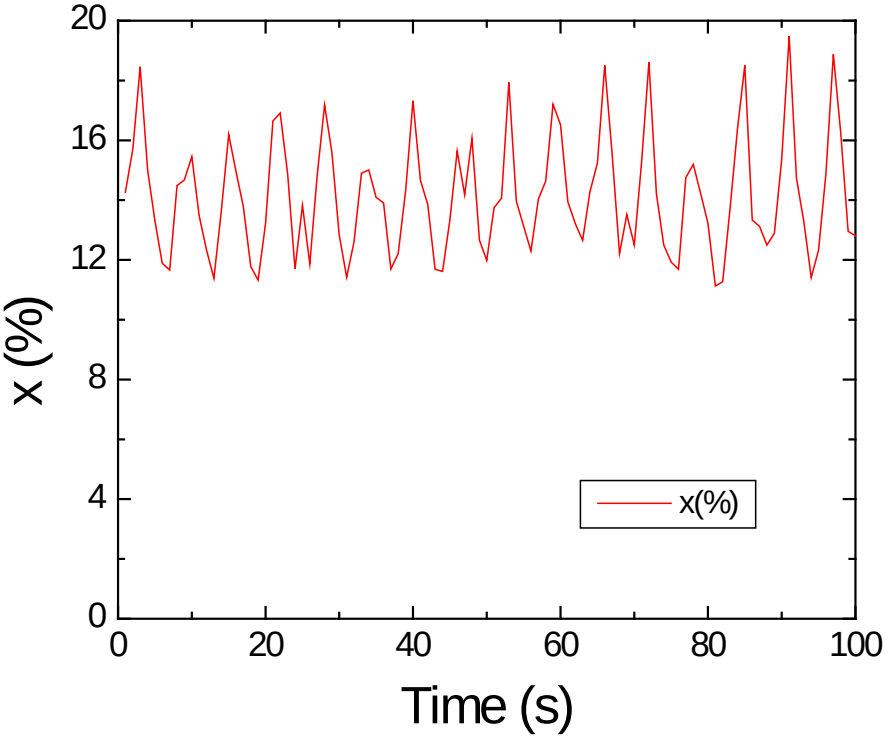

FIG. VII-5. Simulated instantaneous percentage of *x* during the evaporation.

Fig. VII-5 shows the instantaneous value of x calculated from the values shown in Fig. VII-4. The fluctuation in the rate of evaporation of silicon led to a fluctuation in the values of x. The fluctuation also led to irregularity in the thickness of the co-evaporated film as shown in Fig. VII-6.

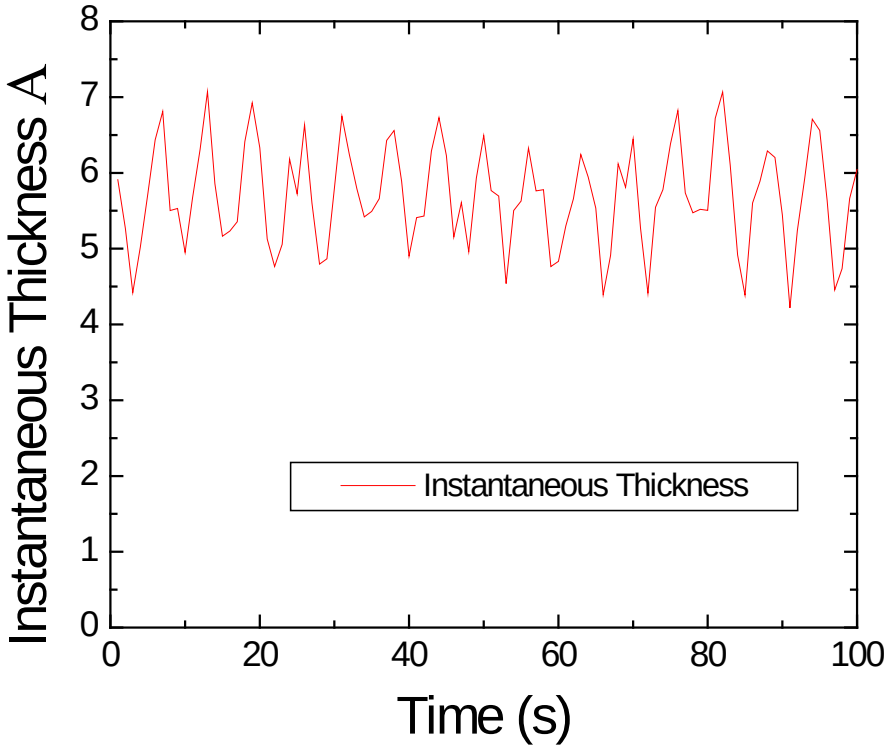

FIG. VII-6. Simulated instantaneous thickness during evaporation.

Keeping the rate of evaporation of pure silicon stable during co-evaporation is difficult. During the process, the evaporation rates were chosen in a way to achieve x=14%, defined as the desired value of x, whereas after the evaporation, a given x value

was computed from the measured values of the QCM and EIES, defined as the achieved value of x. Figure VII-7 shows the desired and achieved values of x for different experimental runs. In Fig.VII-7, the x-axis denotes the thickness of the film segment added to a previously made film or thickness of a new film (note that it is not the cumulative thickness of the film).

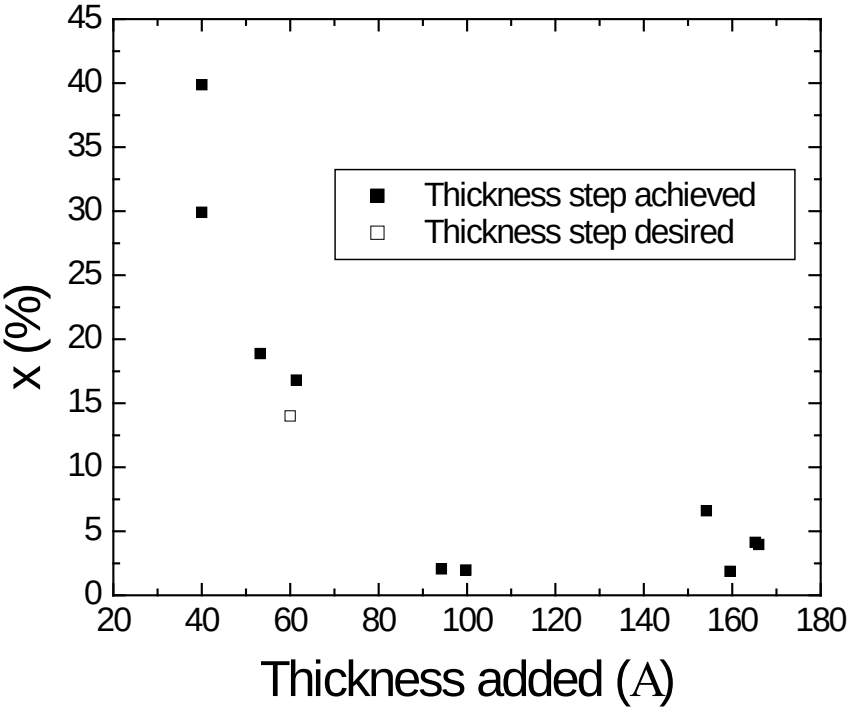

FIG. VII-7 Achieved and desired values of x in percentage vs. the increment in the thickness.

The x value will always deviate from the desired value of x because of the fluctuation of evaporation of pure silicon. To cross check the value of x, we performed

wavelength dispersion spectroscopy (WDS) on the thin films. Compositional analyses were carried out on a four spectrometer Camera SX50 electron microprobes at an accelerating voltage of 15 KV and beam current of 100 nA. All quantitative work employed wavelength-dispersive spectrometers. The analyses were carried out after daily standardization using well-characterized compounds or pure elements; standard checks were run on known samples to verify standardizations.

The X-ray maps were obtained at 15 kV and 100 nA beam current as shown in Fig. VII-8 and Fig. VII-9. The beam was scanned in a 512 × 512-point grid, with a grid width of 185 μm and a total time of 200 or 300 seconds. Two images were acquired: silicon (X-ray counts) and gadolinium (X-ray counts). The brightness is proportional to the number of back-scattered electrons (BSE) from X-rays measured at each pixel (normalized).

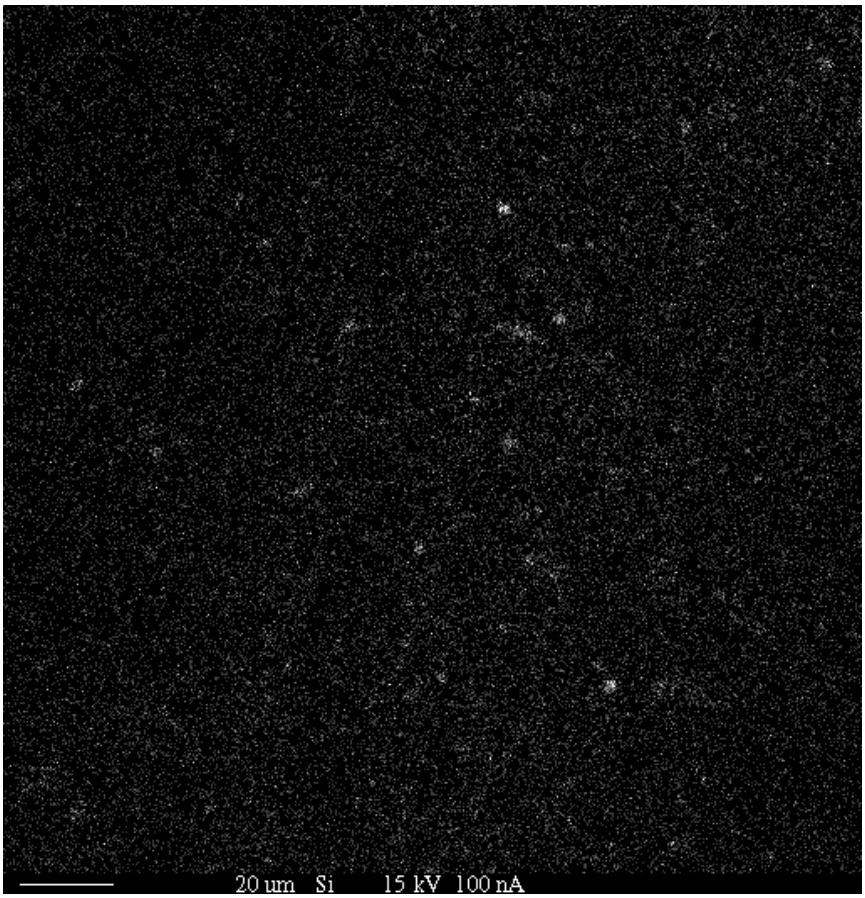

FIG. VII-8. X-ray map at 15 kV and 100 nA beam current for silicon.

Typical accuracy for major elements (> 10 wt %) is about =+/- 1 to 2% of the amount present; the uncertainty would increase as the concentration is decreased, with the uncertainty reaching 100% at the lower limit of detection. The lower limit of detection for most elements is typically 0.05 to 0.10 wt %.

Figure VII-8 shows clusters of white spots which are not uniformly distributed, whereas in Fig. VII-9 white spots are uniformly distributed over the scanned area. This may be due to the difference in the evaporation of gadolinium and silicon. Gadolinium is

conductive and evaporates atomically, on the contrary, silicon is insulating and do not evaporate atomically but sputters in small clusters of molecules. The sputtering of silicon may be responsible for the fluctuation in the evaporation rate.

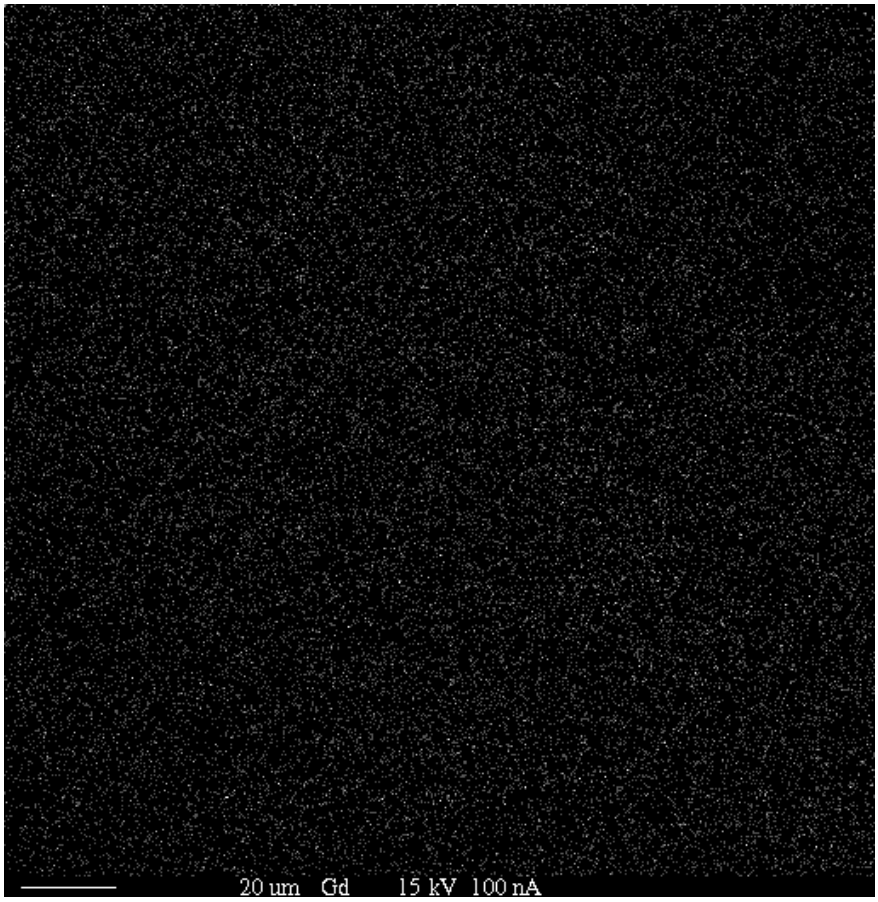

FIG. VII-9. X-ray map at 15kV and 100nA beam current for gadolinium.

Thin film analyses were processed using the program GMRFILM by Waldo on the WDS data. No significant difference appeared between the WDS x value and the value from the GMRFILM program.

Figure VII-10 shows the error in the value of x obtained from QCM and EIES with respect to the value obtained by WDS, and Fig. VII-11 shows the error in the values of x with respect to the estimated value of x using QCM and EIES. Figure VII-11 shows that the lower the concentration of gadolinium, the higher the error in the value of x. The error in concentration could lead to error in the thickness of gadolinium evaporated during a co-evaporation step. The thickness of gadolinium evaporated, as reported by EIES, was compared with the thickness calculated from the x value given by WDS, as shown in Fig. VII-12. In the WDS thickness calculation it was assumed that there was no error due to z- ratio of QCM or equivalent film thickness. The thickness of co-evaporated films was also measured using atomic force microscopy (AFM), which does not match with the calculated values from the QCM and EIES. AFM thicknesses are greater than the estimated value given by QCM and the EIES method. The error in the thickness may be the reason why thin films of $x<14\%$ have higher conductivity than those with $x>14\%$. The resistance of a given film is reproducible, but reproducing a film with the same thickness and same x is very difficult.

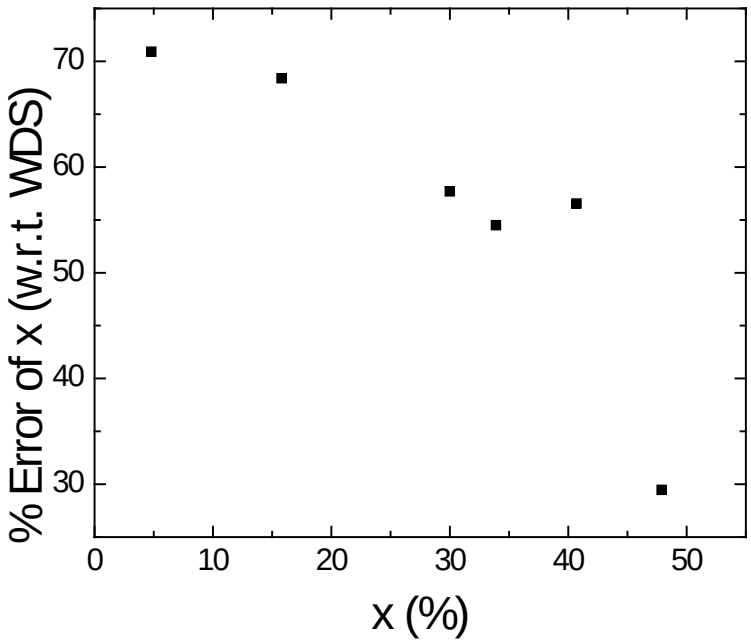

FIG. VII-10. Percentage error in x with respect to WDS.

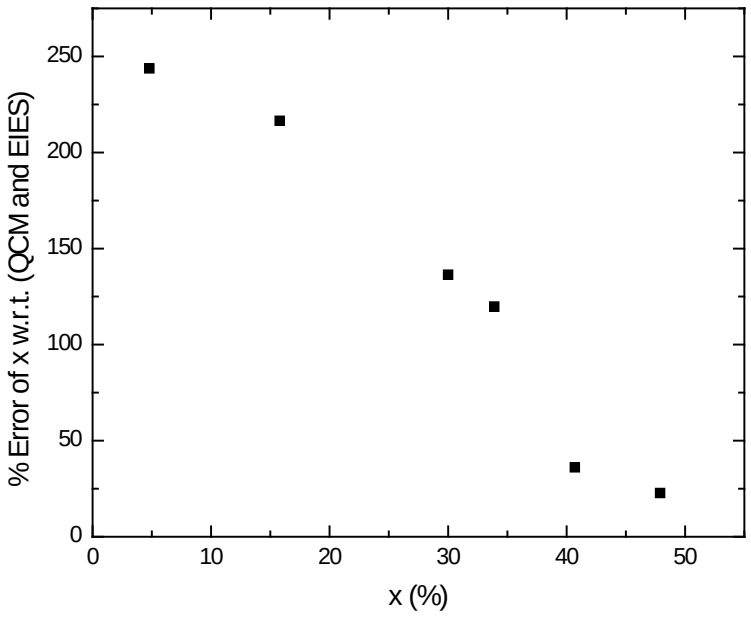

FIG. VII-11. Percentage error in x with respect to QCM and EIES.

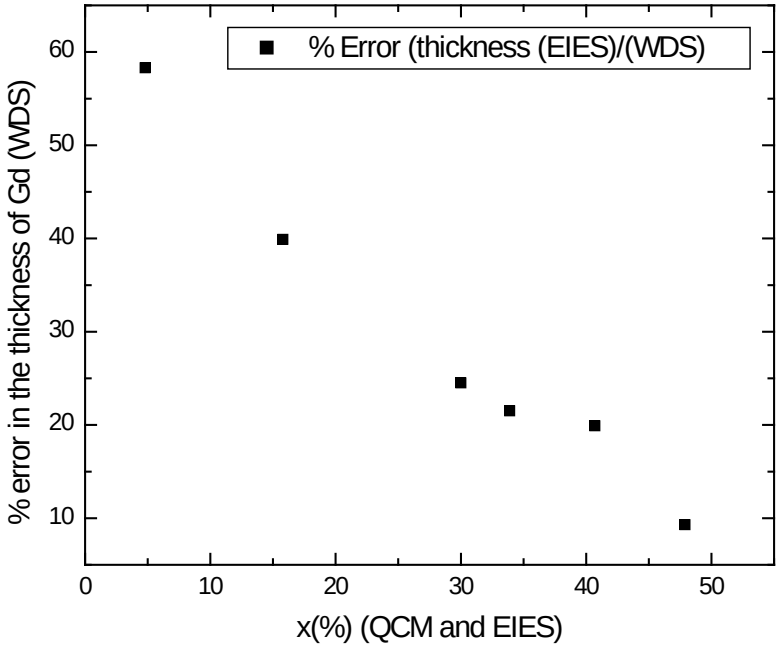

FIG. VII-12. Percentage error in thickness of gadolinium evaporated vs. percentage of x obtained using QCM and EIES.

To understand the conductivity of the thin co-evaporated films, the experimental data were fitted with two different formalisms as shown in Fig. VII-13 and Fig. VII-14. On the insulating side of the transition, conductivity is due to the nearest- neighbor hopping process; on the metallic side of the transition, the conductivity includes the electron-electron scattering process. The theory is dealt with in more detail in Ref. 43. Both conductivity relations are given below.

$$\ln(\sigma_{hopp}) \propto 1/T \qquad \text{(VII-1)}$$

$$\sigma_{cond} \propto T^{1/2} \qquad \text{(VII-2)}$$

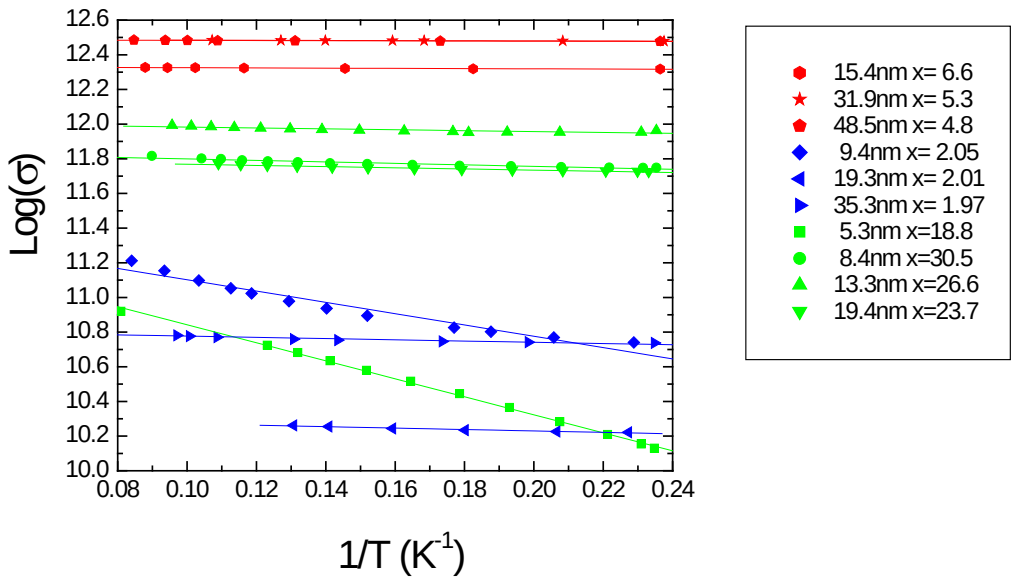

FIG. VII-13. Log(σ) vs. inverse temperature for samples with different thicknesses and x values.

The experimental value of the thicknesses and x are listed in Table VII-1 for the different samples. The thickness of the first film evaporated in each experimental run was smaller than the last one. The range of thicknesses was reduced in successive experiments to produce thinner films, as can be seen in Table VII-1.

All experimental data were fitted with the expressions given in Eq. (VII-1) and Eq. (VII-2). The values of the correlation coefficient (R) from both fits are plotted against the number of samples as shown in Fig. VII-15. The correlation coefficient indicates how well the line approximates the data. If $|R| = 1$, the line is a perfect fit to the data; if $|R| = 0$, the line does not fit the data at all. In general, the closer $|R|$ is to 1, the better the fit.

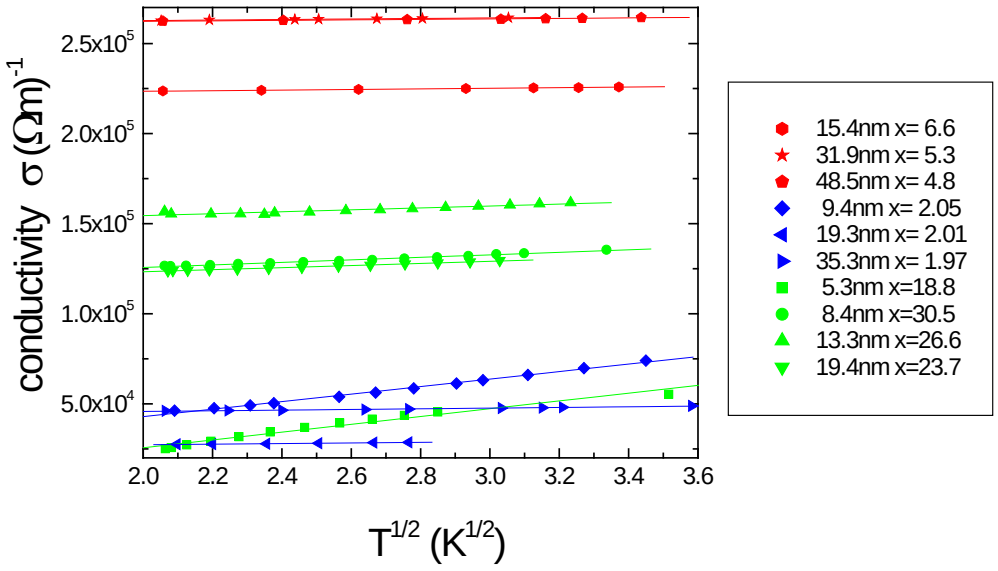

FIG. VII-14. Conductivity vs. $T^{1/2}$ for samples with different thicknesses and x values.

TABLE VII-1. Thicknesses in Å and x in percentage for different samples.

Sample #	x (%)	Thickness (Å)
1	6.6	154.2
2	5.3	319.4
3	4.8	485.4
4	2.05	94.2
5	2.01	193.0
6	1.97	353.5
7	18.8	53.2
8	30.5	84.3
9	26.6	133.0
10	23.7	194.5

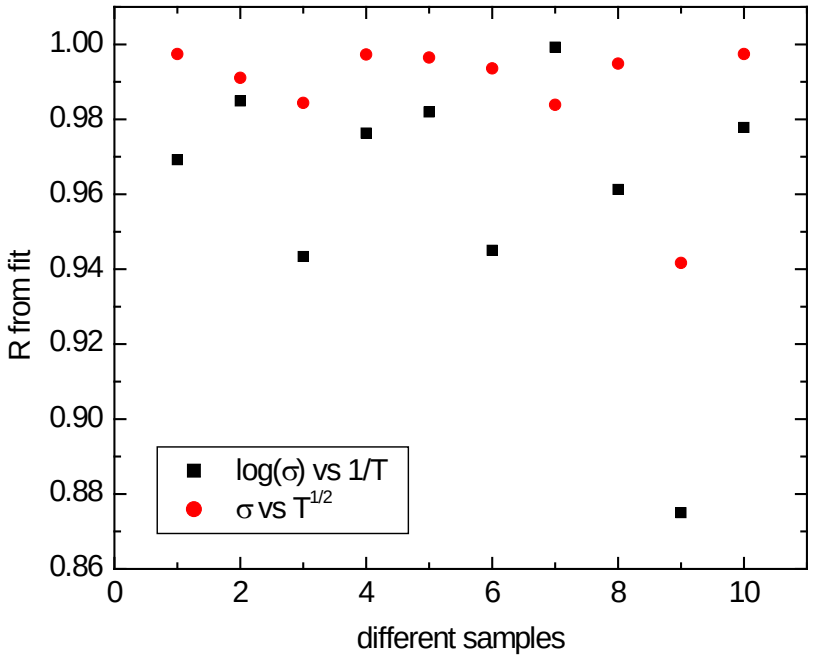

FIG. VII-15. Correlation coefficient R from the fits for [Log (σ) vs. 1/T] and [σ vs. $T^{1/2}$] vs. sample number.

Fig. VII-15 shows that only Sample #7 has a better fit for [Log (σ) vs. 1/T] than (σ vs. $T^{1/2}$). All the samples were metals except Sample #7, which was an insulator.

CHAPTER VIII

SUMMARY AND CONCLUSIONS

Theoretical and experimental study in the field of highly correlated electronic systems has increased in the last decade. This work evaluated spin polarization and the effect of an external magnetic field on a superconductor. Thin films of the magnetically doped semiconductor (GdSi) were made to further investigate the metal-insulator transition (MIT).

The spin polarization was extracted from the density of states measurement of $Al/Al_2O_3/Gd_xSi_{1-x}$ at x=14% near the MIT. To obtain the spin polarization from the density of states, we derived an analytical solution of the AG theory. The analytical method is an improvement to the numerical method commonly used to calculate complex densities of states. The spin polarization extracted using AG DOS is greater than the spin polarization previously extracted from the BCS DOS. In the presence of AG DOS, the system goes from a superconductor with a gap to a gapless superconductor in an external magnetic field.

An attempt was made to probe the MIT in 2-D by making thin films of Gd_xSi_{1-x}. The thin film work explored the transport properties of thin Gd_xSi_{1-x} near the MIT. While the initial aim was to fix x and allow the thickness to vary, the subsequent attempts revealed that both x and the thickness changed from one film to another. Numerous attempts to prepare two samples with the same x but different thicknesses or with the

same thickness but different x values met with failure. Thus, in the experimental part, the co-evaporation of thin films had two possible sources of error. One was the fluctuation in the evaporation rate of pure silicon and the other was the calibration of EIES for gadolinium. Figure VII-8 suggests that silicon was not evaporated but sputtered, as seen from the brighter spots in the X-ray scan. Silicon sputtering may have interfered with the EIES signal and hence reduced the emission intensity of gadolinium vapor. The error in the EIES is related to the amount of silicon evaporated since the z-ratio of the QCM is assumed to be correct. The large amount of silicon suggests an error in the estimated gadolinium thickness determined by the EIES.

The interference of the silicon evaporation described above is similar to the emissions from common residual gases that may interfere with the vapor flux, and can cause an erroneous flux measurement. The interference is most pronounced when measuring low flux density in the presence of gases, such as in a reactive deposition processes. The EIES problem can be solved by using two QCMs, each measuring the thickness and evaporation rate of an individual material, but fluctuations in x will remain as in silicon fluctuates. It has become increasingly evident that the accuracy of the gadolinium rate of the co-evaporation plays a significant role in controlling the x in Gd_xSi_{1-x}. A new arrangement is required to better monitor the evaporation rates during co-evaporation.

Experimental data suggests that the films produced are metallic as the conductivity is nonzero at zero temperature. The co-evaporation involves multiple calibration processes that complicated the experiment. The stability of the rate at which

silicon can be evaporated also played an important role in the control of x in the co-evaporation process. A POCO graphite crucible was used to get a smoother evaporation, but the silicon wet the crucible and made it usable only for a couple of evaporations before it shattered. Film Thickness as measured by AFM was larger than that measured by QCM measurements, which suggests a possible error in the assumptions of the z-ratio for the QCM measurement. The QCM thickness error is also related to x, which makes the error difficult to remove; hence, the QCM error should be further investigated if this project is continued.

There is a possibility that the large fluctuation in the evaporation rate of silicon can be removed by making an alloy with tantalum. It is not clear whether including tantalum as an impurity will affect the physical properties of the Gd_xSi_{1-x} alloy. At present, attempts have been made to observe a MIT in 2-D caused by impurities. Gd_xSi_{1-x} could be used to study the phenomenon. A 2-D MIT is still open for further investigation.

REFERENCES

[1] V. L. Ginzburg, Phys.-Uspekhi, **42**, 353 (1999); Phys.-Uspekhi, **45**, 205 (2002).

[2] A. L. Pergament, G.B. Stefanovich, and A. A. Velichko, in *Condensed Matter At The Leading Edge*, edited by M. P. Das (Nova Science, New York 2006), Chap1.

[3] N. F. Mott, *Metal-Insulator Transitions* (Taylor and Francis ltd, London 1974).

[4] M. Imada, A. Fujimori, and Y. Tokura, Rev. Mod. Phys. **70**, 1039 (1998).

[5] P. P. Edwards, T. V. Ramakrishnan, and C. N. Rao, J. Phys. Chem. **99**, 5228 (1995).

[6] D. Belitz and T. R. Kirkpatrick, Rev. Modern Phys. **66**, 261 (1994).

[7] C. N. R. Rao and B. Raveau, *Transition Metal Oxides: Structure, Properties and Synthesis of Ceramic Oxides* (Wiley- VCH, New York 1998).

[8] P. A. Cox, *Transition Metal Oxides. An Introduction to Their Electronic Structure and Properties* (Clarendon Press, Oxford 1992).

[9] C. N. R. Rao, Annu. Rev. Phys. Chem. **40**, 291(1989).

[10] J. M. D. Coey, M. Viret, and S. von Molnar, Advances in Physcis, **48**, 167 (1999).

[11] A.-M. Haghiri-Gosnet, and J.-P. Renard, J. Phys. D: Appl. Phys. **36**, R127 (2003).

[12] C. D. Esposti-Boschi and L. Ferrari, Phil. Mag. *B*, **80**, 1693 (2000).

[13] A. G. Zabrodsky and K.N. Zinov'eva, Zh. Exper. Teor. Fiz. (JETP) **86**, 727 (1984).

[14] S. Bogdanovich, M. P. Sarachik, and R. N. Bhatt, Phys. Rev. B **60**, 2292 (1999).

[15] A. El Kaauoachi, A. Nafidi, Ah. Nafidi, and G. Biskuspski, Semicond. Sci. Technol. **18**, 69 (2003).

[16] K. H. Kim, J. P. Wand, W.C. Joiner, and Y.H. Kim, J. Phys.: Condens. Matter **10**, 2963 (1998).

[17] G. Biskupski, A. El Kaaouachi, and A. Briggs, J. Phys.: Condens. Matter **3**, 8417 (1991).

[18] I. Shlimak, M. Kaveh, R. Ussyshkin, V. Ginodman, L. Resnick, and V. F. Gantmakher, J. Phys.: Condens. Matter **9**, 9873 (1997).

[19] N. A. Poklonski and A. I. Syaglo, Phys. Solid State **40**, 132 (1998); N. A. Poklonskii, S. A. Vyrko, and A. G. Zabrodskii, Phys. Solid State **46**, 1101 (2004).

[20] S. Abboudy, Physica B **212**, 175 (1995).

[21] E. A. Davis and W.D. Compton, Phys. Rev. **140**, A2183 (1965).

[22] A. Fujimori and Y. Tokura, *Spectroscopy of Mott Insulators and correlated metals* (Springer, Tokyo 1995).

[23] W. L. MacMillan and J. Mochel, Phys. Rev. Lett. **46** (8), 556 (1981).

[24] G. Hertel, D. J. Bishop, E. G. Spencer, J. M. Rowell, and R. C. Dynes, Phys. Rev. Lett. **50**, 743 (1983).

[25] F. Hellman, W. geerts, and B. Donehew, Phys. Rev. B **67**, 12406 (2003).

[26] P. Xiong, B. L. Zink, S. I. Applebaum, F. Hellman, and R. C. Dynes, Phys. Rev. B **59**, R3929 (1999).

[27] L. Bokacheva, W. Teizer, F. Hellman, and R. C. Dynes, Phys. Rev. B. **69**, 235111 (2004).

[28] W. Teizer, F Hellman, and R. C. Dynes, in *Proceedings of the 25th International Conference on the Physics of Semiconductors, 2000,* Edited by N. Miura and T. Ando (Springer, Osaka 2000).

[29] F. Hellman, D. R. Queen, R. M. Potok, and B. L. Zink, Phys. Rev. Lett. **84**, 5411 (2000).

[30] B. L. Zink, E. Janod, K. Allen, and F. Hellman, Phys. Rev. Lett. **83**, 2266 (1999).

[31] W. Teizer, F. Hellman, and R. C. Dynes , Physica E **18**, 266 (2003).

[32] W. Teizer, F. Hellman, and R. C. Dynes, Phys. Rev. B **67**, 121102(R) (2003).

[33] D. N. Basov, A. M. Bratkovsky, P. F. Henning, B. Zink, F. Hellman, Y. J. Wang, C. C. Homes and M. Strongin, Europhys. Lett. **57**, 240 (2002).

[34] W. Teizer et al., Int. J. Mod. Phys. *B* **17**, 3723 (2003).

[35] M. A. Paalanen, T. F. Rosenbaum, G. A. Thomas, and R. N. Bhatt, *Phys. Rev. Lett*. **48**, 1284 (1982); S. Waffenschmidt, C. Pfleiderer, and H. v. Lohneysend, *ibid*. **83**, 3005 (1999).

[36] I. Terry, T. Penny, S. von Molnar, J. M. Rigotty, and P. Becla, Solid State Commun. **84**, 235 (1992); C. Leighton, I. Terry, and P. Becla, Europhys. Lett. **42**, 67 (1998); *Phys. Rev. B* **58**, 9773 (1998).

[37] S. von Molnar and S. Methfessel, J. Appl. Phys. **38**, 959 (1967); S. von Molar, A. Briggs, J. Flouquet, and G. Remenyi, Phys. Rev. Lett. **51**, 706 (1983); S. Washburn, R. A. Webb, S von Molnar, F. Holtzberg, J. Flouquet, and G. Remenyi, Phys. Rev. *B* **30**, 6224 (1984); J. Jaroszynski and T. Dietl, Physica B **177**, 469 (1992).

[38] R. P. Galazka, in *Proceedings of the 14th International Conference on Physics of Semiconductors, Edinburgh, 1978,* edited by B. H. L. Wilson (IOP Conf. Ser. 43, IOP, London 1978).

[39] J.A. Gaj, in *Proceedings of the 15th International Conference on Physics of Semiconductors, Kyoto, 1980*; J. Phys. Soc. Jpn. Suppl. A, 747, **49** (1980).

[40] T. Dietl, in *Proceedings of the 5th International Conference on Application of High Magnetic Fields in Semiconductor Physics and Magnetic Materials, Hakone, 1980,* Edited by S. Chikazumi and N. Miura (Springer, New York, 1981).

[41] J. K. Furdyna, J. Appl. Phys. **53**, 7637 (1982).

[42] D. Weller, Phys. Rev. Lett. **63**, 155 (1985).

[43] C. Ran, and C. Jin, J. Appl. Phys. **54**, 3667 (1988).

[44] P. A. Lee and T. V. Ramakrishnan, Rev. Mod. Phys., **57**, 287 (1985).

[45] http://ssg.als.lbl.gov/ssgdirectory/arenholz/alsum06/helgren.pdf

[46] J. Bardeen, L. N. Cooper, andJ. R. Schrieffer, Phys. Rev. **108**, 1175 (1957).

[47] A. A. Abrikosov and L. P. Gorkov, Zh. Eksperim. I Teor. Fiz. **39**, 1781 (1960).

[48] P. Majumdar and S. Kumar, Phys. Rev. Lett. **90**, 237202 (2003).

[49] E. Abrahams, P. W. Anderson, D. C. Licciardello, and T. V. Ramakrishnan, Phys. Rev. lett. **42**, 673 (1979)

[50] S. V. Kravchenko, G. V. Kravchenko, J. E. Furneaux, V. M. Pudalov, and M. D'lorio, Phys. Rev. B **50**, 8039 (1994).

[51] E. Punnose and A. M. Finkel'stein, Science **310**, 289 (2005).

[52] P. A. Cox, *Transition Metal Oxides. An Introduction to Their Electronic Structure and Properties* (Clarendon press, Oxford, 1992).

[53] K. Yosida, Phys. Rev. **110**, 769 (1958).

[54] B. S. Chandrasekhar, Appl. Phys. Lett. **1**, 7 (1962).

[55] A. M. Clogston, Phys. Rev. Lett. **9**, 266 (1962).

[56] P. Flude, Solid State Commun. **5**, 181 (1967).

[57] N. N. Bogoliubov, V. V. Tolmachev, D. V. Shrikov, Fortschr. Physik **6,** 605 (1958).

[58] J. G. Valatin, Nuovo Cimento **7**, 405 (1958).

[59] A. A. Abrikosov, L. P. Gor'kov, I. E. Dzyaloshinki, *Methods of Quantum Field Theory in Statistical Physics* (Prentice-Hall, inc., Englewood Cliffs, New Jersey, 1963), chap. 7.

[60] F. Reif, Phys. Rev. **106**, 208 (1957).

[61] G. M. Androes and W. D. Knight, Phys. Rev. **121**, 779 (1961).

[62] R. J. Noer and W. D. Knight, Rev. Mod. Phys. **36**, 177 (1964).

[63] A. M. Clogston, A. C. Gossard, V. Jaccarino, and Y. Yafet, Phys. Rev. Lett. **9**, 262 (1962).

[64] R. H. Hammond and G. M. Kelly, Rev. Mod. Phys. **36**, 185 (1964).

[65] R. A. Ferrell, Phys. Rev. Lett. **3**, 269 (1959).

[66] P. W. Anderson, Phys. Rev. Lett. **3**, 325 (1959).

[67] A. A. Abrikosov and L. P. Gorkov, Zh. Eksp. Teor. Fiz. **42**, 1088 (1962) [Sov. Phys. – JETP **15**, 752 (1962)].

[68] A. A. Abrikosov and L. P. Gor'kov, Zh. Eksp. Teor. Fiz. **39**, 1781 (1960); **39**, 866 (1961). [Soviet Phys.—JETP **12**, 1243 (1961)].

[69] C. Caroli, P. G. De Gennes, J. Matricon, J. Phys. Radium **23**, 707 (1962).

[70] P. G. De Gennes and G. Sarma, J. Appl. Phys. **34**, 1380 (1963).

[71] L. P. Gorkov and A. I. Rusinov, J. Exptl. Theoret. Phys. U.S.S.R. **46** (1964) 1363.

[72] E.W. Hudson, S. H. Pan, A. K. Gupta, K.-W. Ng, J. C. Davis, Science **285**, 88 (1999).

[73] G. Tkachov and K. Richter, Phys. Rev. B **75,** 134517 (2007).

[74] D. Parker and P. Thalmeier Phys. Rev. B **75,** 184502 (2007).

[75] R. V. A. Srivastava and W. Teizer. Solid State Comm. **145**, 512 (2008).

[76] A. Baratoff, Ph.D. dissertation, Cornell University, 1964, Pg. 77.

[77] W. Teizer, F. Hellman, and R. C. Dynes, Phys. Rev. B **67**, 121102 (2003).

[78]M. Tinkham, *Introduction to Superconductivity* (Robert E. Krieger Publishing Company, Malabar, Florida, 1975), Ch. 2-8.

[79]L. Solymar, *Superconductive Tunnelling and Applications* (Wiley-Interscience Div, New York 1972).

[80] I. Giaever and K. Mergerle, Phys. Rev. **122**, 1101 (1961).

[81] P. M. Tedrow and R. Meservey, Phy. Rev. B. **7**, 318 (1973)

[82] L. N. Cooper, Phys. Rev. **104**, 1189 (1956).

[83] R. C. Dynes, V. Narayanamurti, and J. P. Garno, Phys. Rev. Lett. **41**, 1509 (1978).

[84] J. H. Park, E. Vescovom, H. J. Kim, C. Kwon, R. Rameshm and T. Venkatesan, Phy. Rev. Lett. **81**, 1953 (1998).

[85] R. J. Soulen, Jr., J. M. Byers, M. S. Osofsky, B. Nadgorny, T. Ambrose, S. F. Cheng, P. R. Broussard, C. T. Tanaka, J. Nowak, J. S. Moodera, A. Barry and J. M. D. Coey, Science **282**, 85 (1998).

[86] C. T. Tanaka, J. Nowak and J. S. Moodera, J. Appl. Phys. **86**, 6239 (1999).

[87] I. Giaever, Phys. Rev. Lett. **5**, 464 (1960).

[88] I. Gaiever, H. R. Hart, Jr., and K. Megerle. Phys. Rev. **126**, 941 (1962).

[89] J. Klein and A. Leger, Phys. Lett. A **28** (2), 134 (1968).

[90] R. Meservey and P. M. Tedrow, Phys. Rep. **238**, 173 (1994).

[91] K Maki and T Tsuneto, Progr. Theoret. Phys. **31**, 945 (1964).

[92] K. Maki, Prog. Theor. Phys. **32**, 29 (1964).

[93] K. Maki, Progr. Theoret. Phys. (Kyoto) **31**, 731 (1964).

[94] K. Maki and P. Fulde, Phys. Rev. **140**, A1586 (1965).

[95] R. V. A. Srivastava, W. Teizer, F. Hellman, and R. C. Dynes., Physica B cond. Matt. **403**, 1321 (2008).

[96] E. Dagotto, T. Hotta, and A. Moreo, Phys. Rep. **344**, 1 (2001); T. Becker, C. Streng, Y. Luo, V. Moshnyaga, B. Damaschke, N. Shannon and K. Samwer, Phys. Rev. Lett. **89**, 237203 (2002).

[97] S. Wagner, M. Lakner, H. v. Lohneysen, Phys. Rev. B **55**, 4219 (1997); T. G. Castner, Phys. Rev. B **68**, 115201 (2003).

[98] V. M.Nicoli, M.S. thesis, Texas A&M University, College Station, TX, 1984.

[99] V. F. Gantmakher, *Electrons and Disorder in Solids*, International series of monographs on Physics 130 (Clarendon press, Oxford, London 2005).

APPENDIX A

ANALYTICAL EXPRESSION

Due to space constraints, the long form of the analytical solution is not included in the dissertation. Figure A-1 shows the same expression but written with a different style to show the simplicity of the complex expression. Figure A-2 shows the AG density of states output of the expression in Fig. A-1 in MATHEMATICA. The program to plot the AG DOS is added as a supplement to this dissertation.

$$A = \text{Function}[\{\xi, \alpha\}, 2 - 2\alpha^2 + \xi^2];$$

$$B = \text{Function}[\{\xi, \alpha\}, \left(-1 + \alpha^2 + \xi^2\right)^2];$$

$$CC = \text{Function}[\{\xi, \alpha\}, -1 + \alpha^6 + 3\xi^2 - 3\xi^4 + \xi^6 + 3\alpha^4\left(-1 + \xi^2\right) + 3\alpha^2\left(1 + 16\xi^2 + \xi^4\right)];$$

$$DD = \text{Function}[\{\xi, \alpha\}, 6\sqrt{3}\sqrt{\alpha^2\xi^2\left(\alpha^6 + 3\alpha^4\left(-1 + \xi^2\right) + \left(-1 + \xi^2\right)^3 + 3\alpha^2\left(1 + 7\xi^2 + \xi^4\right)\right)}];$$

$$EE = \text{Function}[\{\xi, \alpha\}, (CC[\xi, \alpha] + DD[\xi, \alpha])^{\frac{1}{3}}];$$

$$u = \text{Function}[\{\xi, \alpha\}, \frac{1}{6}\left(3\xi + \sqrt{3}\sqrt{\left(A[\xi, \alpha] + \frac{B[\xi, \alpha]}{EE[\xi, \alpha]} + EE[\xi, \alpha]\right)} - \sqrt{3}\sqrt{\left(2A[\xi, \alpha] - \frac{B[\xi, \alpha]}{EE[\xi, \alpha]} - EE[\xi, \alpha] - \frac{6\sqrt{3}\left(1 + \alpha^2\right)\xi}{\sqrt{\left(A[\xi, \alpha] + \frac{B[\xi, \alpha]}{EE[\xi, \alpha]} + EE[\xi, \alpha]\right)}}\right)}\right)];$$

$$v = \text{Function}[\{\xi, \alpha\}, \text{Re}[u[\xi, \alpha] / (u[\xi, \alpha] * u[\xi, \alpha] - 1)^{1/2}]]$$

$$\text{Plot}[\{v[\text{Re}[\xi], 1.755], v[\text{Re}[\xi], 1.350], v[\text{Re}[\xi], 1.000], v[\text{Re}[\xi], 0.786], v[\text{Re}[\xi], 0.505], v[\text{Re}[\xi], 0.362], v[\text{Re}[\xi], 0.250], v[\text{Re}[\xi], 0.171], v[\text{Re}[\xi], 0.100]\}, \{\xi, 0, 3\}]$$

FIG. A-1. Analytical expression (from MATHEMATICA).

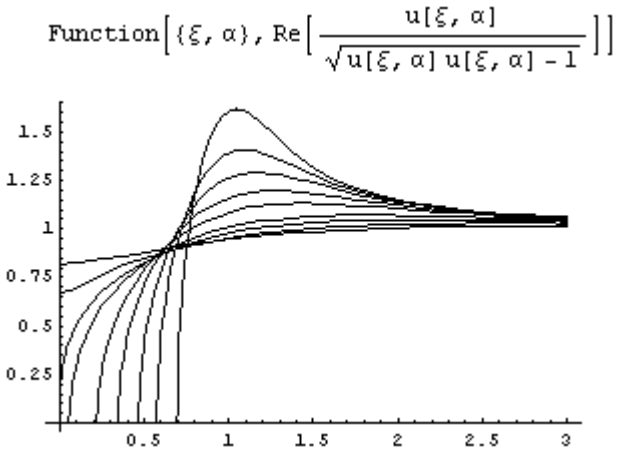

FIG. A-2. AG density of states for different values of α (from MATHEMATICA).

APPENDIX B

INTEGRATION RANGE

The BCS density of state is given by the following equation.

$$\frac{N_s(E)}{N(0)} = \frac{d\xi}{dE} = \begin{cases} \mathrm{Re}\left(\dfrac{(E)}{(E^2 - \Delta^2)^{1/2}} \right) & (E > \Delta) \\ 0 & (E < \Delta) \end{cases} \qquad \text{(B-1)}$$

where Δ is the gap parameter, and 2Δ is the energy gap. Figure B-1 shows the BCS DOS.

Figure B-1 shows the BCS density of states. As we include the temperature effects with a Fermi distribution, Fig. B-1 changes to Fig. B-2 for a temperature T=25 mK. The values of the iteration step increment are taken in such a way that the values of the integrated function do not change to the 10^{th} decimal place.

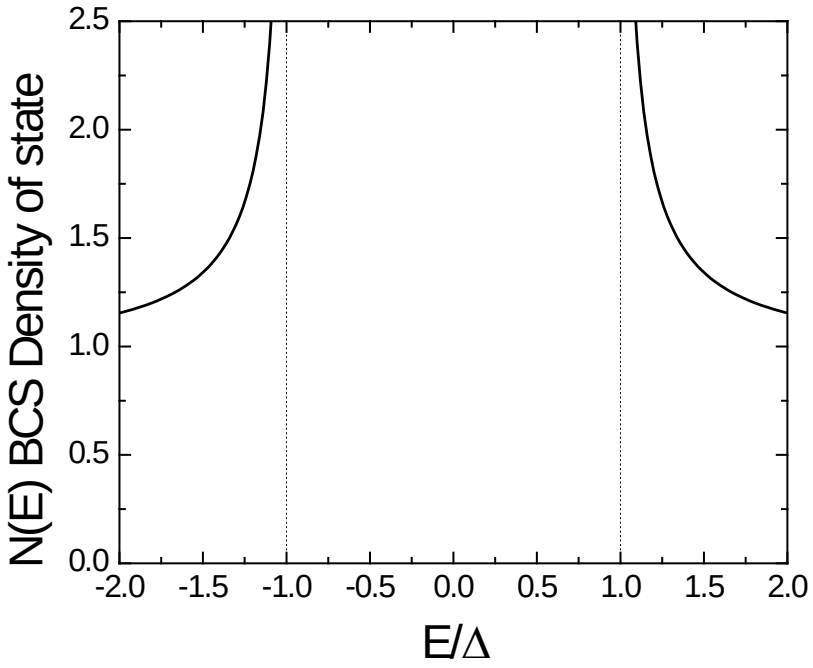

FIG. B-1. BCS density of state versus normalized energy.

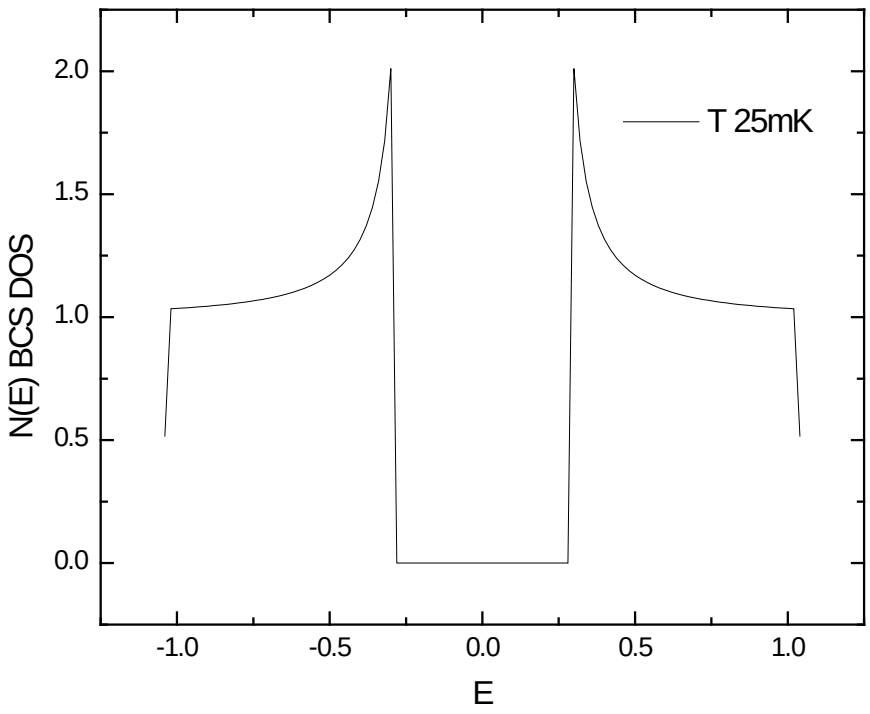

FIG. B-2. BCS DOS at temperature T = 25 mK.

Even a small change in temperature can affect the BCS DOS. We observe a sudden fall in the density of states at the graph boundary, an artifact of the integration being carried out only upto the boundary. For the rest of the graphs, we will show data only where the integration is carried out to sufficiently high |E| to avoid the artifact.

The calculation shows that at finite temperature the singularity in the DOS at the gap edge is reduced to finite values and a density of states appears in the gap.

APPENDIX C

FLOWCHART

Figure C-1 compares two different flow charts. The left one is the flow chart used before the analytical solution of the AG theory was discovered. In the left flowchart, for every iteration step the computer has to find a numerical value of the AG density of states for a given set of parameters. The process consumes a lot of computation time if the number of iteration steps is large. The flowchart on the right side of Fig. C-1 does not have that problem, as the program does not compute the solution at every iteration step. The arrow specifies the change in the step from the older numerical approach to the newer and better method.

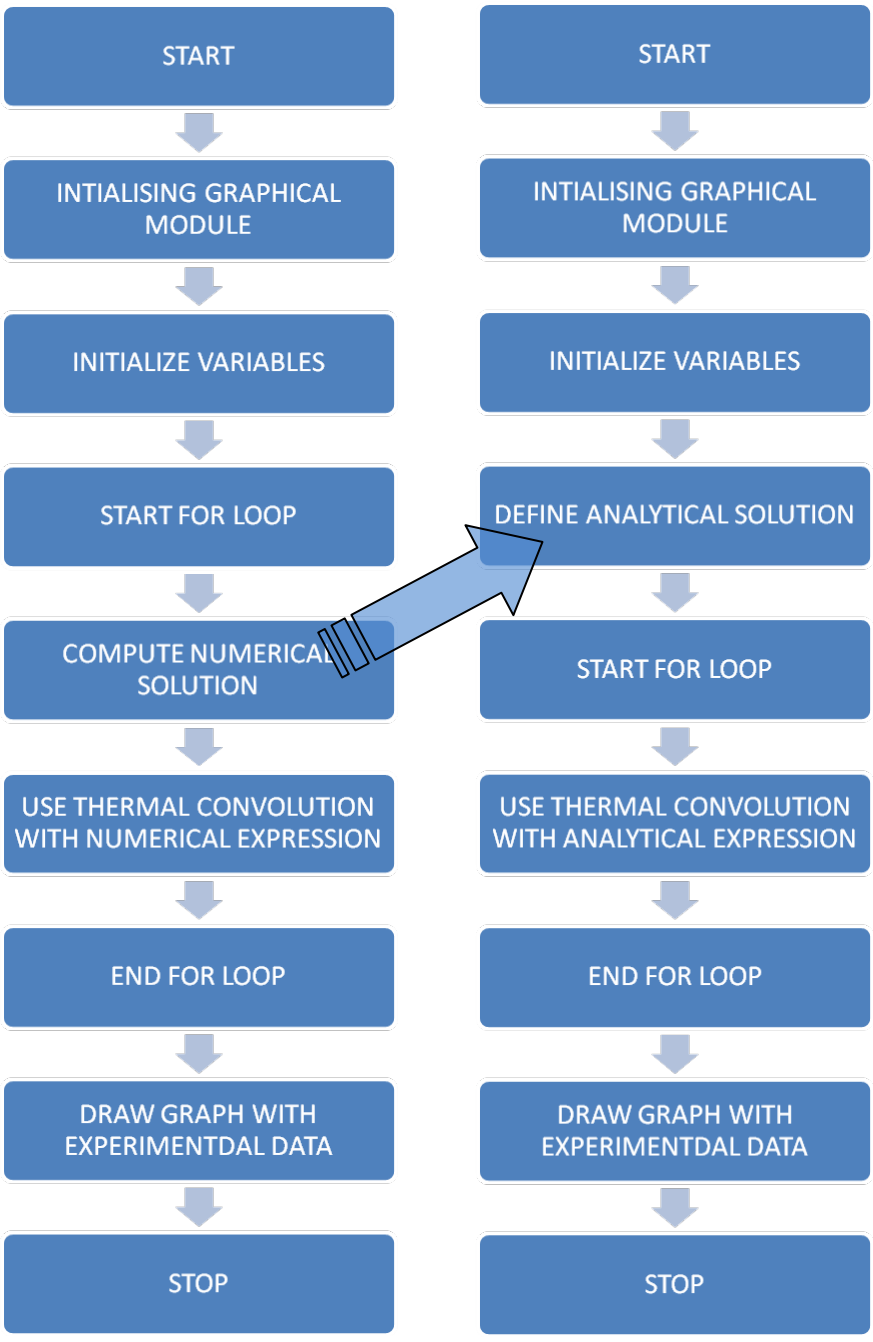

FIG. C-1. Flowcharts for two different methods, the right with analytical solution and the left without it.

APPENDIX D

ERROR ANALYSIS

Once we were able to plot different graphs using the analytical solution, we also did error analysis. We tried different error methods to find the best fit as mentioned below.

1. Least squares difference in x axis
2. Least squares difference in y axis
3. Combination of both 1 and 2

In Method 1 we take the theoretical data at a given x and experimental data at the same x, take the difference, square it, and then sum it over all values of x. With the help of this method, we were able to move the theoretical fit close to the gap where the data is dense and does not give a convergence to find a local minimum.

In Method 2 we were not able to implement this method as there were two to four values of x for a given y which leads to an undefined relation to compute, the same is the case for method 3.

We also wrote a program to find best fit or global minima using error in a D-4 space, and then followed the path with least error value as shown in the Fig. D-1. In each step the path is decided by the error as defined in Method 1. This method does not give the best visual fit as the densities of data points, which influence the error, are different at different crucial area of the graph. Figure D-2 shows the areas that were under scrutiny during visual fit. We decided the best fit by making a matrix of possible best fit graphs

and picking it visually. Reduction in calculation time using the analytical solution enabled error analysis.

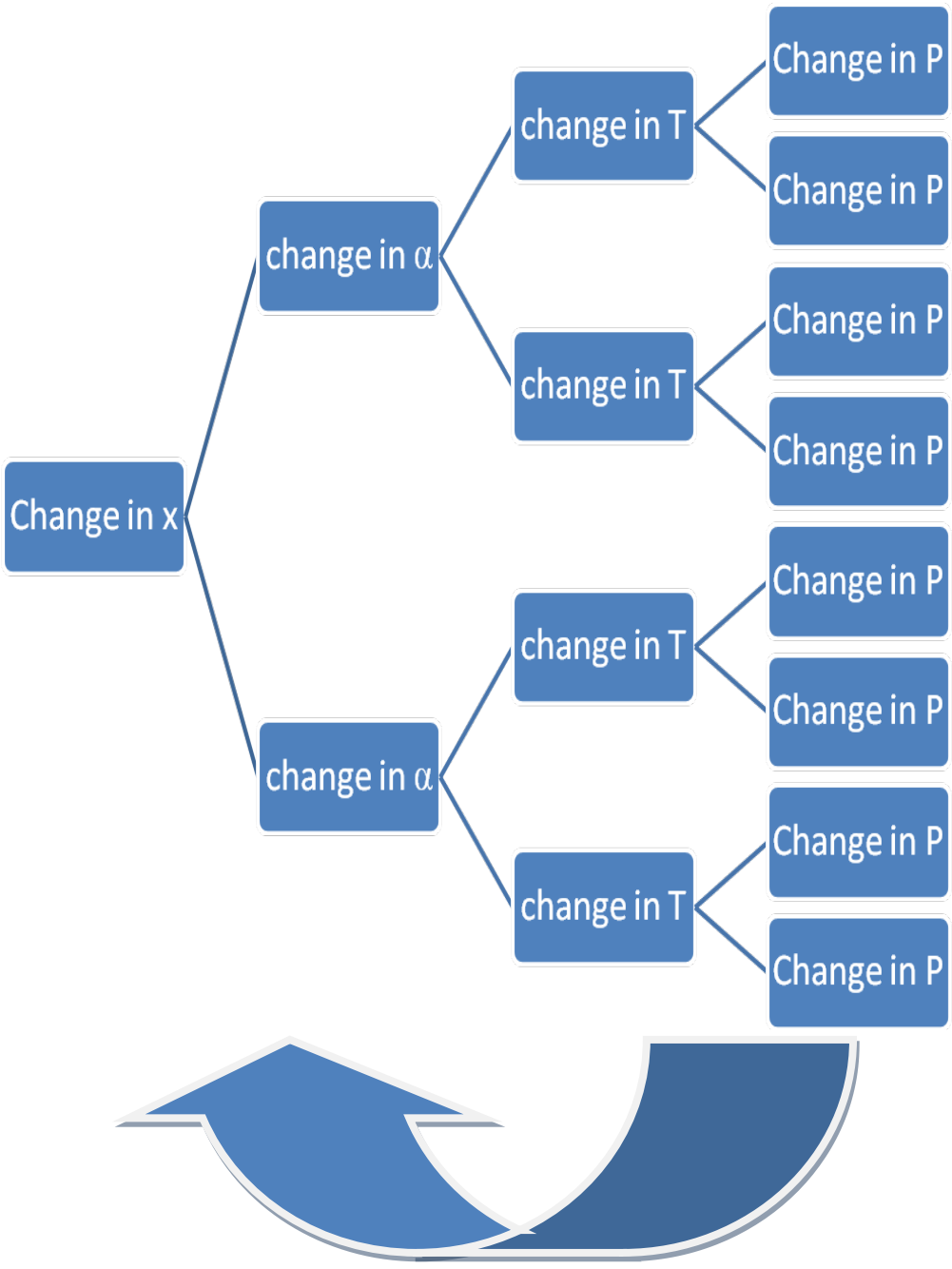

FIG. D-1. Flowchart to find a best fit with error analysis.

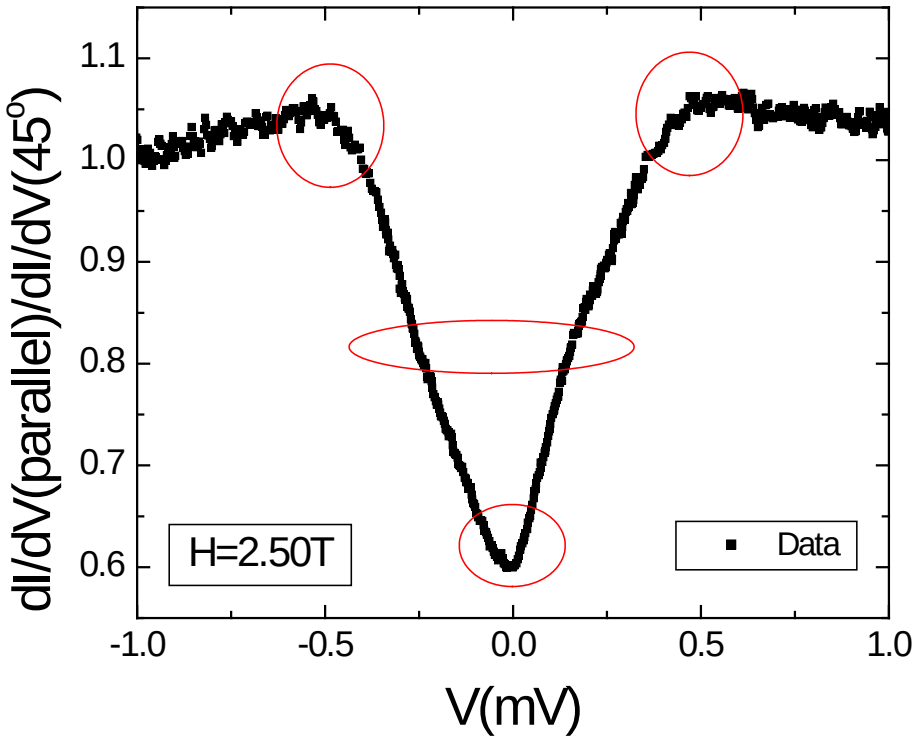

FIG. D-2. Normalized conductance data vs. applied voltage. Ovals shows areas under inspection.

Error calculation was not able to give a better fit, as we changed parameters to reduce error. In this process it increases the error locally at the some areas, as shown in Fig. D-2, but reduces the error at other part of the graph. This fails to fit crucial points and still has a small error. The error method was not further used to find the best fit.

APPENDIX E

ELECTRON IMPACT EMISSION SPECTROSCOPY

This appendix explains the electron impact emission spectroscopy (EIES). For co-evaporating, EIES has an advantage over a standard quartz-crystal microbalance. In EIES, the evaporated flux is allowed to enter the sensor just above the specific source as shown in Fig. E-1, and does not allow flux to enter from another source in the multi evaporated system.

A known cross-sectional area of vapor is bombarded with electrons with known cross-sectional area, which is formed by an emitter assembly at a potential of -175 V with respect to rest of the assembly. This results in the fraction of vapors getting excited, and ends up emitting a specific spectrum for a given material. The total emission current is controlled at 6mA and is chopped at 320 Hz by the regulating anode current. In this manner, interference of the signal with induced and thermal emfs may be subtracted and thus reduce the background noise. An optical channel collects the photon emission and passes it though a vacuum-sealed optical window to a photo-detection system located outside the UHV region. This detection unit contains a grating that allows a specific frequency to be detected. At a specific electron excited energy, emission intensity of the characteristic lines from any material is proportional to the number density of that constituent in the vapor flux. The optical output signal is linearly proportional to the deposition rate.

The relationship of the emission to rate is given below.

For any material mass deposition rate per unit area, D is given by Eq. E-1.

$$D = m\, v\, N \tag{E-1}$$

where m is mass and v is the average velocity of the evaporated particles, and N is the number density near the substrate.

The relationship between the optical intensity, I, and the mass deposition rate can be approximated by Eq. E-2.

$$I = \frac{gD}{T^{1/2}} \tag{E-2}$$

where T is the temperature and g is the gauge constant which depends on the material, electron energy and the sensitivity of the photo detector. Hence, intensity is linearly proportional if g and T are constant.

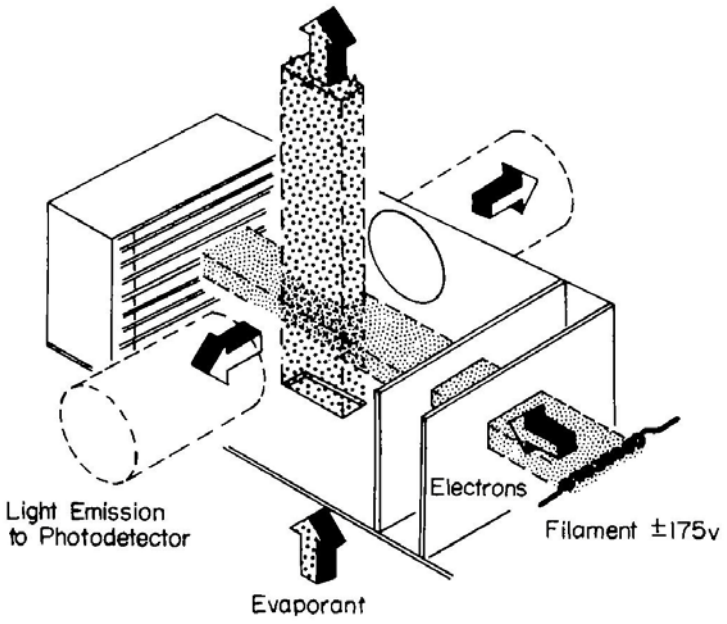

FIG. E-1. Basic features of the EIES sensor.

VITA

Raj Vibhuti Anand Srivastava was born in Lucknow, India. He is the son of Mrs. Pushpa Lata Srivastava and Mr. Triloki Nath Srivastava.

He entered Indian Institute of Technology, Kharagpur, in September 1997 and majored in physics. Upon completion of his Bachelor of Science degree in May 2000, he began his Master of Science program under the direction of Dr. Anushree Roy at Indian Institute of Technology, Kharagpur. He received the Master of Science in physics, with emphasis on the Piezo-electric property of fresh chicken bones, in May 2002.

He joined Texas A&M University in August 2002 and conducted research under the direction of Dr. Winfried Teizer. He received the Master of Science in physics, with emphasis of making thin films of $Mn_{12}FAc$ using pulsed laser depositions, in May 2005 and received his Ph.D. degree in physics in May 2009 from Texas A&M University. His email address is rajvibhuti@yahoo.com.

c/o Dr. Winfried Teizer

Department of Physics

Texas A&M University

College Station, TX 77843-4242